



HAL
open science

Growth and optical characterization of Sb-based materials on InP for optical telecommunication

Yu Zhao

► **To cite this version:**

Yu Zhao. Growth and optical characterization of Sb-based materials on InP for optical telecommunication. Optics / Photonic. INSA de Rennes, 2014. English. NNT : 2014ISAR0002 . tel-01083881

HAL Id: tel-01083881

<https://theses.hal.science/tel-01083881v1>

Submitted on 18 Nov 2014

HAL is a multi-disciplinary open access archive for the deposit and dissemination of scientific research documents, whether they are published or not. The documents may come from teaching and research institutions in France or abroad, or from public or private research centers.

L'archive ouverte pluridisciplinaire **HAL**, est destinée au dépôt et à la diffusion de documents scientifiques de niveau recherche, publiés ou non, émanant des établissements d'enseignement et de recherche français ou étrangers, des laboratoires publics ou privés.



THESE INSA Rennes
sous le sceau de l'Université européenne de Bretagne
pour obtenir le titre de

DOCTEUR DE L'INSA DE RENNES
Spécialité : Physique-Optoélectronique

présentée par
Yu ZHAO

ECOLE DOCTORALE : SDLM
LABORATOIRE : FOTON-OHM

Growth and optical characterization of Sb-based materials on InP for optical telecommunication

Thèse soutenue le 11.02.2014
devant le jury composé de :

Éric Tournié

Professeur - Université de Montpellier 2 / rapporteur / président du jury

Régis André

Directeur de recherche - Institut Néel Grenoble / rapporteur

François Julien

Directeur de recherche - IEF Orsay / examinateur

Paul Koenraad

Professor - Technische Universiteit Eindhoven / examinateur

Anne Ponchet

Directeur de recherche - CEMES Toulouse / examinateur

Hervé Folliot

Professeur - INSA de Rennes / Co-encadrant de thèse

Mathieu Perrin

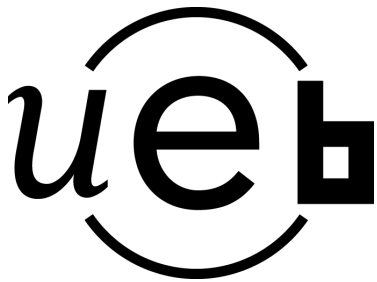
Maître de conférences - INSA de Rennes / Co-encadrant de thèse

Nicolas Bertru

Professeur - INSA de Rennes / Directeur de thèse

Growth and optical characterization of Sb-based materials on InP for optical telecommunication

Yu Zhao



Remerciement

Les études présentées dans cette thèse ont été réalisées pendant une durée de trois ans dans le laboratoire FOTON-OHM à Rennes.

Je tiens dans un premier temps à remercier Nicolas Bertru, Hervé Folliot et Mathieu Perrin, pour avoir m'avoit confié ce travail de recherches et m'avoit encadré quotidiennement. Leurs grandes expériences dans l'épitaxie et dans les caractérisations optiques m'ont toujours éclairé. Mes remerciements vont aussi à Antoine Létoublon, pour ses expertises de diffraction de rayon X.

Durant ces trois années, j'ai pu vivre dans un milieu particulièrement agréable et ces travaux n'auraient pas pu aboutir sans l'aide de l'ensemble des membres de l'équipe : Tony Rohel pour la croissance SSMBE et Marianne Prévôt pour la première version de banc d'absorption ...

Cette thèse ne serait pas complète sans des nombreuses collaborations à l'extérieur du laboratoire. Je tiens mes remerciements particulièrement à Anne Ponchet et Julien Nicolaï pour les analyses TEM et pour m'avoit accueilli dans leur laboratoire. J'adresse un grand remerciement aussi à Professeur Paul Koenraad et Samuel Mauger de Technische Universiteit Eindhoven pour leurs excellentes analyses X-STM. Nous remercions aussi François Julien pour nous avoir permis à réaliser les premiers mesures d'absorption inter-sous-bandes dans son laboratoire. Je voudrais également exprimer toute ma reconnaissance à M. Régis Andrés et M. Éric Tournié, qui m'ont fait honneur d'avoit rapporté cette thèse et d'avoit participé au jury de soutenance.

Ces remerciements ne seraient pas complets sans une pensée pour les « jeunes » du laboratoire et des amis que j'ai eu le plaisir de côtoyer durant ces quelques années à Rennes.

Mes dernières pensées iront vers mes parents, qui m'auront permis de poursuivre mes études jusqu'à aujourd'hui.

Contents

Introduction	1
1 Epitaxial Growth of Antimonides on InP Substrate	7
1.1 MBE system	8
1.2 Epitaxial growth of lattice-matched alloys on InP substrate	9
1.3 Deposition of lattice-mismatched materials on InP substrate	11
2 The Growth of $\text{Ga}_{0.47}\text{In}_{0.53}\text{As}/\text{AlAs}_{0.56}\text{Sb}_{0.44}$ Quantum Wells for Inter-subband Applications	17
2.1 Inter-subband transition and devices	18
2.2 Inter-band properties of GaInAs/AlAsSb multiple quantum wells	22
2.3 Inter-subband properties of GaInAs/AlAsSb multiple quantum wells	26
2.4 The effects of surface terminations	35
2.5 The impact of digital alloy growth	43
3 Sb-mediated Growth of InAs/AlAs_{0.56}Sb_{0.44} Strained Quantum Wells for Inter-subband Applications	53
3.1 Properties of InAs/AlAsSb strained quantum well	54
3.2 Sb-mediated Growth of InAs on InP substrate	55
3.3 Sb-mediated growth of pseudomorphic InAs/AlAsSb single quantum well	58
3.4 Strain compensation in InAs/AlAsSb multiple quantum wells	64
3.5 Polarization-dependent absorption in InAs/AlAs _{0.56} Sb _{0.44} multiple quantum wells	68
4 Sb-mediated Growth of InAs/GaAs_{0.51}Sb_{0.49} Heterostructures on InP Substrate	75
4.1 InAs quantum dots on grown on (001) and (113)B substrates	76
4.2 InAs/GaAs _{0.51} Sb _{0.49} quantum wells on InP (001) substrate	79
4.3 Surface-orientation dependent surfactant effect of Sb	91
5 Incorporation of Sb in Strained InAs(Sb) Heterostructures	97
5.1 Thermodynamics of Sb-incorporation in strained InAs	98

5.2 Sb-incorporation in InAs/Al _{0.48} In _{0.52} As quantum wells	101
Conclusion	107
Résumé	109
Appendices	119
A.1 Inter-subband absorption workbench	119
A.2 Thermodynamic calculations on the composition of InAs _{1-x} Sb _x	120
A.3 Surfactant effect on the surface of Ga _{0.47} In _{0.53} As	125
A.4 Routine experimental methods	127

Introduction

Silica optical fiber networks are nowadays deployed all over the world and they connect the continents by transmitting infrared light signals in 1.55 μm band. InP-based lasers and photo-detectors are deployed to generate and to pick up light-signal transmitted in long-haul telecommunication networks. The telecommunication infrastructure has never stopped evolving, to meet the ever-increasing demand of Internet traffic. Many InP-based devices are being researched on to enable even faster modulation, denser multiplexing and more sophisticated modulation scheme. For example, InP-based light source like InAs/InP quantum-dash lasers is able to generate clock signal at a repetition rate over 300 GHz [1]. On the electronic side, InP-based GaInAs transistor can operate at frequencies as high as 710 GHz [2] and it can be easily integrated with current InP-based technologies.

Paradoxically, advanced signal processing in optical networks relies on electronics. Various conversions between light and electronic signals are performed during the journey of each bit of information and the limit of electronics will one day be a bottleneck to achieving faster data exchange. At the same time, scaling up such electronics-based infrastructure will lead to elevated energy cost [3].

To overcome such limits, full-optical signal processing has been proposed to bypass the electronics. The modulation of light signal boils down to rapid change of optical functions of the transmitting medium. Inter-subband transition in a quantum-well structure is one of the physical processes that enable fast attenuation and refractive index change. It enables fast switching from ON-state to OFF-state in a fraction of one pico-second [4, 5], which corresponds to a modulation rate even higher than 1 THz. Besides the fastness, its high non-linear properties [6] also mark potential uses in efficient modulation schemes like high-order phase-keying. Many quantum-well structures that allow inter-subband transition at 1.55 μm have been studied for potential use in full-optical signal processing, ranging from GaN/AlGaIn [7], ZnSe/CdSe [8], to GaInAs/-AlAsSb [5] quantum wells which is fully compatible with InP substrate.

Many of the aforementioned structures are developed using epitaxy technologies like molecular beam epitaxy (MBE). For it can achieve sharp interface and thickness precision down to one atomic layer, this thin film growth technology is able to realize many nanostructures as-designed. Also, its various adjustable growth parameters are indis-

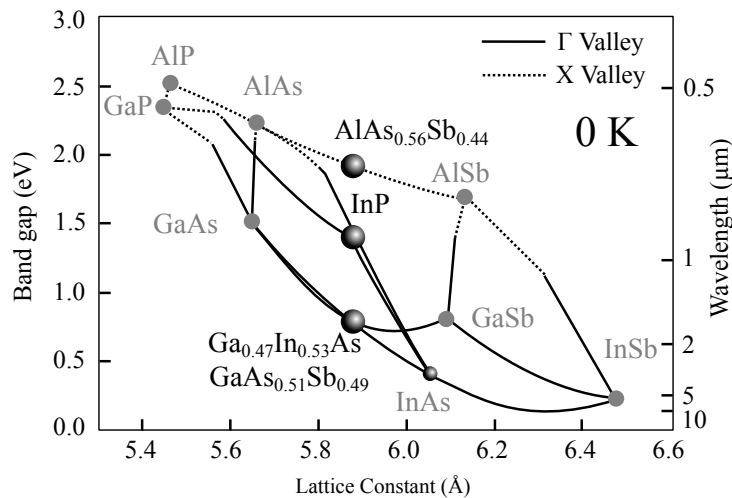


Figure 1: Band-gaps and lattice constants of common III-V compound semiconductor compounds and their alloys (0 K). Direct band-gap alloys are interpolated by solid curves while indirect ones are dot or dashed lines. Reproduced according to [9].

pensable for structure optimization. Furthermore, various analyzing facilities integrated in MBE growth chamber enable *in situ* observation of epitaxial growth mechanism. MBE is hence the choice for the research of less adopted materials like antimonide alloys.

Figure 1 illustrates band gap and lattice parameters of commonly used III-V semiconductors. Antimonide compounds like GaSb and InSb have smaller band gaps than most common III-V semiconductors, and they are found in lower part of figure 1. They are found very useful in mid-infrared light generation and detection. However, it is difficult to integrate these compounds in InP-based devices for their large lattice constants. Fortunately, by alloying antimonides with arsenic compounds, they can form ternary alloys like $\text{AlAs}_{0.56}\text{Sb}_{0.44}$ and $\text{GaAs}_{0.51}\text{Sb}_{0.49}$ that are lattice-matched to InP substrate. The incorporation of Sb in these alloys leads to smaller band-gap as compared to their arsenic components. At the same time, they introduce new band line-up with materials that is commonly used on InP substrate like GaInAs. Together, they offer new possibilities in InP-based applications.

Figure 2 shows several semiconductor alloys that are lattice-matched to InP substrate. GaInAs/GaAsSb quantum wells possess a type-II line-up with an effective gap as small as 0.3 eV. This makes it suitable for infrared generation and detection in 3-5 μm band. On the other side of the spectrum, (Ga)InAs/AlAsSb quantum wells has a conduction band offset as large as 1.6 eV [9]. Such deep electron confinement potential profile allows inter-subband transition in mid-infrared and even near-infrared range. For one thing, it allows quantum cascade laser operating at 3 μm . For another, it enables inter-subband absorption near 1.55 μm (0.8 eV) that find its uses in full-optical signal processing. Realizing inter-subband transition at 3 μm with these material is a major

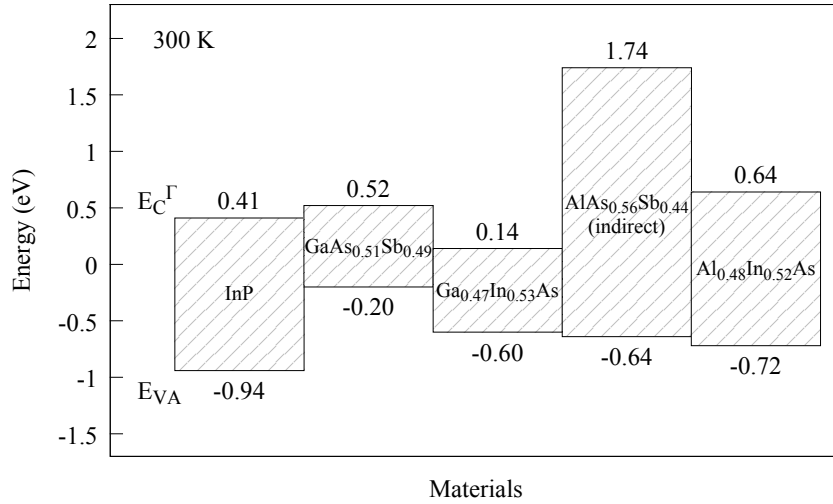


Figure 2: Band line up of several ternary alloys that are lattice matched to InP. Data are taken from [9].

topic studied in this thesis.

Beside antimonide alloys, elemental Sb has also found important uses in the epitaxial growth of lattice-mismatched materials. Usually, by depositing an epitaxial materials that have much larger lattice constants than that of substrate, the deposit would organize into quantum dots structures (three-dimensional nanometric islands). The use of Sb in such growth can significantly increase the quality of the epitaxial thin film; and yet Sb atoms incorporate little and mostly stay on the growth surface [10]. It was demonstrated that the use of Sb can effectively delay the formation of quantum dots or the generation of dislocations [11, 12]. This aspect of Sb is known as surfactant effect for it being a *surface active agent*. Under other circumstances, the use of Sb has also demonstrated enhancement to the properties of quantum-dot structures, including increased island density, more uniform size distribution, as well as several other benefits [13–15]. Although these Sb-related phenomena have important technological uses in device elaboration, their mechanisms are often disputed.

The use of antimonides and surfactant effect of Sb being the clue of this thesis, it is developed as follows:

- Chapter 1 will provide more details on MBE growth, especially the growth of antimonide alloys on InP substrate. Following that, different epitaxial growth modes of lattice-mismatched materials are introduced.
- Chapter 2 begins by attempting to tune inter-subband absorption wavelength of Ga_{0.47}In_{0.53}As/AlAs_{0.56}Sb_{0.44} quantum well structures to 1.55 μm , which is however not achieved. A series of growth optimization and microscopic study were conducted, and these results indicate that multiple imperfections within such struc-

tures, such as the unintended incorporation of Sb into GaInAs layer, could be responsible.

- Chapter 3 advances the findings of chapter 2 and tries to shorten inter-subband transition wavelength, by replacing lattice matched $\text{Ga}_{0.47}\text{In}_{0.53}\text{As}/\text{AlAs}_{0.56}\text{Sb}_{0.44}$ with strained $\text{InAs}/\text{AlAs}_{0.56}\text{Sb}_{0.44}$. At a first time, the surfactant effect of Sb has well exercised its power and ensures good quality of single quantum well. Following that, stacking of these quantum wells were obtained by means of “strain compensation”. At the end of this chapter, preliminary investigation into inter-subband transition in strained $\text{InAs}/\text{AlAs}_{0.56}\text{Sb}_{0.44}$ quantum wells will be presented.
- Chapter 4 explores the influence of Sb on the InAs deposition on different substrate orientations, in order to better understand the surfactant effect of Sb. Completely different growth behaviors were observed for InAs deposition on (001) and (113)B surfaces of $\text{GaAs}_{0.51}\text{Sb}_{0.49}$. The spectacular differences are interpreted by surface orientation dependent surfactant effect of Sb.
- Chapter 5 closes this thesis with preliminary investigations on the incorporation of Sb in highly-strained InAs layer on InP substrate. The use of Sb during the deposition of InAs(Sb) introduces two competing effects: it helps maintain layer-by-layer growth by covering the surface; at the same time, it favors the formation of relaxed island for it contributes more strain energy by incorporating into InAs. The practice of such growth could serve as a test of the effectiveness of Sb surfactant effect, and at the same time it can give some reflections on the magnitude of competing energetic terms.

References

- [1] K. Merghem et al., “Pulse generation at 346 GHz using a passively mode locked quantum-dash-based laser at 1.55 μm ”, *Applied Physics Letters* **94**, 021107 (2009).
- [2] W. Hafez et al., “12.5 nm base pseudomorphic heterojunction bipolar transistors achieving $f_T=710$ GHz and $f_{\text{max}}=340$ GHz”, *Applied Physics Letters* **87**, 252109 (2005).
- [3] O. Wada, “Recent progress in semiconductor-based photonic signal-processing devices”, *IEEE Journal of Selected Topics in Quantum Electronics* **17**, 309–319 (2011).
- [4] J. Hamazaki et al., “Ultrafast intersubband relaxation and nonlinear susceptibility at 1.55 μm in GaN/AlN multiple-quantum wells”, *Applied Physics Letters* **84**, 1102 (2004).
- [5] T. Akiyama et al., “1.55 μm picosecond all-optical switching by using intersubband absorption in InGaAs-AlAs-AlAsSb coupled quantum wells”, *IEEE Photonics Technology Letters* **14**, 495–497 (2002).
- [6] S.-i. Gozu et al., “Cross phase modulation efficiency enhancement in $\text{In}_{0.8}\text{Ga}_{0.2}\text{As} / \text{Al}_{0.5}\text{Ga}_{0.5}\text{As} / \text{AlAs}_{0.56}\text{Sb}_{0.44}$ coupled double quantum wells by tailoring interband transition wavelength”, *Applied Physics Express* **2**, 042201 (2009).
- [7] M. Tchernycheva et al., “Systematic experimental and theoretical investigation of intersubband absorption in GaN/AlN quantum wells”, *Physical Review B* **73**, 125347 (2006).

- [8] R. Akimoto et al., “Ultrafast intersubband optical switching in II-VI-based quantum well for optical fiber communications”, *physica status solidi (b)* **243**, 805–812 (2006).
- [9] I. Vurgaftman et al., “Band parameters for III–V compound semiconductors and their alloys”, *Journal of Applied Physics* **89**, 5815 (2001).
- [10] T. F. Kuech, “Surfactants in semiconductor epitaxy”, in *AIP conference proceedings*, Vol. 916 (2007), p. 288.
- [11] J. C. Harmand et al., “GaInAs/GaAs quantum-well growth assisted by sb surfactant: toward 1.3 μm emission”, *Applied Physics Letters* **84**, 3981–3983 (2004).
- [12] C. Gatel et al., “Analysis by high-resolution electron microscopy of elastic strain in thick InAs layers embedded in Ga_{0.47}In_{0.53}As buffers on InP(0 0 1) substrate”, *Acta Materialia* **58**, 3238–3246 (2010).
- [13] N. Kakuda et al., “Sb-mediated growth of high-density InAs quantum dots and GaAsSb embedding growth by MBE”, *Applied Surface Science* **254**, 8050–8053 (2008).
- [14] A. Gocalinska et al., “Suppression of threading defects formation during sb-assisted metamorphic buffer growth in InAs/InGaAs/InP structure”, *Applied Physics Letters* **100**, 152112 (2012).
- [15] W. LU, “Elaboration par épitaxie par jets moléculaires et caractérisation de nanostructures à base d’antimoine sur substrats InP”, PhD thesis (Institut National des Sciences Appliquées de Rennes, Rennes, France, 2010), 214 pp.

Chapter 1

Epitaxial Growth of Antimonides on InP Substrate

This chapter is dedicated to introducing all the epitaxially grown materials studied in this thesis. At a first time, the solid source molecular beam epitaxy (MBE) system along with its major growth parameters are shortly covered in section 1.1. Following that, section 1.2 explains how lattice-matched materials like $\text{Ga}_{0.47}\text{In}_{0.53}\text{As}$ and $\text{AlAs}_{0.56}\text{Sb}_{0.44}$ are elaborated on InP substrate, and the choice of their growth conditions. These ternary alloys are essential to inter-subband applications studied in chapter 2 and 3. The final section 1.3 walks through different manner in which the deposition of lattice-mismatched material like InAs could would behave on InP substrate. According to deliberately manipulated growth conditions, different degrees of strain relaxation could result in either fully-strained two-dimensional InAs layer or three-dimensional InAs quantum dots, which are essential to the subjects studied in subsequent chapters 3-5.

1.1 MBE system

All the samples studied in this thesis were prepared using a Riber 21T compact solid-source MBE system. Figure 1.1 illustrates its growth chamber, an ultra-high vacuum (UHV) enclosing where the epitaxial growth takes place. In essential, it consists of a set of evaporation cell sending molecular beams to a heated substrate. Therefore, they define the most important growth parameters of MBE growth: substrate temperature and flux intensities (pressures) of molecular beams.

Substrate for crystal growth is mounted onto molybdenum holders, which is heated from its back side during the growth. The heater reading number is measured by thermo-sensor, which is calibrated by well-known temperatures, like surface reconstruction transition temperature and melting points. The substrate temperature is stabilized by partial-integral-differential controllers to ensure fluctuation smaller than $0.1\text{ }^{\circ}\text{C}$. The eventual run-to-run temperature difference is estimated to be less than $5\text{ }^{\circ}\text{C}$.

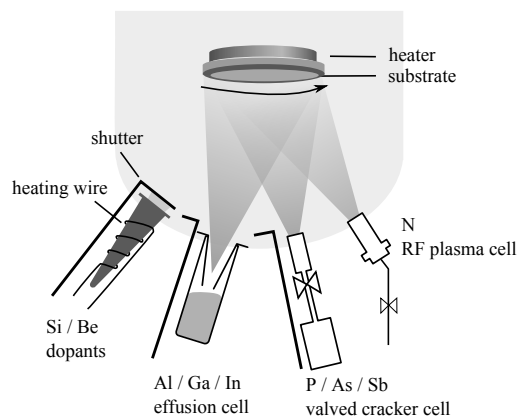


Figure 1.1: An illustrative representation of MBE growth chamber (Riber 21T)

The molecular beam fluxes are produced by different type of source cells. Group-III elements like Al, Ga, In as well as doping atoms like Si and Be are evaporated using Knudsen-type effusion cells. In these type of cell, molecular beams are produced by heating substances contained in ceramic crucibles. A mechanic shutter plates is installed in front of each cell to enable on-off flux modulation. Since flux intensities of these elements are solely determined by the cell temperature, they cannot be changed rapidly. In order to realize rapid change of a given elemental flux within one growth-run, redundant cells should be equipped. Group-V elements like P, As, Sb are produced by more sophisticated valved-cracker cell. In these cells, the micrometric valves enable rapid flux variation. Also, pure solid are not only evaporated but also pyrolyzed at a high-temperature cracking stage, turning Sb_4 into Sb_2 for example. The use of bi-atomic molecules like Sb_2 can significantly modifies the incorporation behavior of Sb, and this will be further addressed in chapter 5.

The output of each source cell is measured by a retractable flux gauge positioned in front of the substrate. The gauge readings are recorded in beam equivalent pressure ; they are actively monitored before each growth-run and consistent output of each cell is crucial for reproducible results. In the literatures beam equivalent pressures are commonly given to describe growth conditions, but in practice growth parameters like growth-rate are equally important. This will be explained shortly.

1.2 Epitaxial growth of lattice-matched alloys on InP substrate

Figure 1.2 offers a microscopic view of substrate surface under MBE growth. At a first time, the incoming molecules or atoms get adsorbed on the surface and then get involved in a series of surface processes like massive migration across all kinds of features on the growth surface (surface diffusion). Eventually, the ad-atoms could settle down and join the lattice, or possibly gain enough energy and leave the growth system (desorption). Many of these processes can be kinetically controlled, which makes MBE growth dependent of substrate temperature and other specific growth parameters in a complex manner.

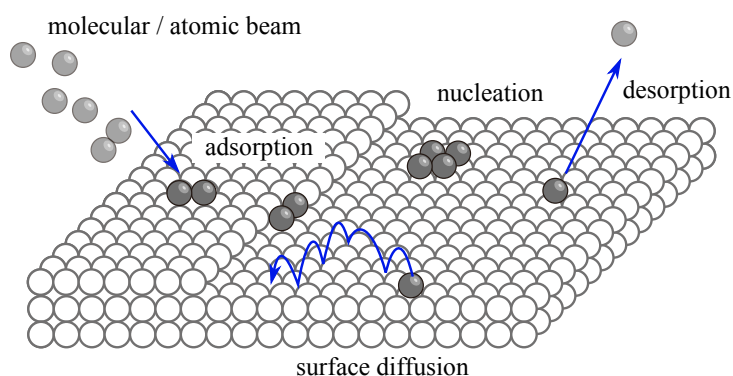


Figure 1.2: MBE growth surface

During the growth of binary compound like GaAs, over-saturated level of group-V element (As) is usually supplied, that is, under a V/III beam equivalent pressure ratio greater than 1. Under such circumstances, the desorption of group-III element (Ga) is negligible and they have unity sticking coefficient. On the other side, the desorption of group-V atoms (As) is significant and it has complex dependence on growth parameters. In practice, *growth rate* is used to describe the incorporating rate of group-III element. It is determined by thickness of materials grown in given time and it is usually expressed in mono-layer per second (ML/s). Experimentally, the growth rate is measured with the help of strained super-lattice composed of repeated InP/AlInP pairs of thick InP and very thin AlInP layers for example. The thickness of GaAs layers can be approximated

by the thickness of one super-lattice period, which is in turn measured by ω - 2θ scans in X-ray diffraction.

The growth of ternary alloys like $\text{Ga}_{0.47}\text{In}_{0.53}\text{As}$ and $\text{Al}_{0.48}\text{In}_{0.52}\text{As}$ is simply done by co-deposition of their constituent binary alloys GaAs, AlAs and InAs. For alloys like GaInAs, which contains two types of cations (group-III elements) and one anion, its composition can be well estimated by the growth rates of cations since cation desorption is usually negligible. For example, the growth $\text{Ga}_{0.47}\text{In}_{0.53}\text{As}$ is achieved by simultaneous deposition of Ga and In, at growth rates of 0.11 ML/s and 0.12 ML/s respectively.

For the growth ternary alloys like $\text{AlAs}_{0.56}\text{Sb}_{0.44}$ or $\text{GaAs}_{0.51}\text{Sb}_{0.49}$, which contain different anions (group-V elements), the achievement of lattice-matching condition is more challenging. Due to the desorption of anions, the alloy composition is influenced by the substrate temperature and even the growth rate of cation (group-III element) [1, 2]. Nevertheless, the desorption of anion can be reduced by sending equal amount of anion and cation to growth surface. In practice, this corresponds to a low V/III beam equivalent pressure ratio, and the desired AlAsSb composition can be found by varying the growth rate of Al while keeping group-V flux at constant level. The composition of such alloys is routinely checked, and the misfit of $\text{AlAs}_{0.56}\text{Sb}_{0.44}$ and $\text{GaAs}_{0.51}\text{Sb}_{0.49}$ grown on InP substrate are kept lower than 0.1% (AlAsSb 0.07%, GaAsSb 0.05%).

Unlike $\text{Ga}_{0.47}\text{In}_{0.53}\text{As}$, a classical material for InP substrate, much less information is available about the growth of $\text{AlAs}_{0.56}\text{Sb}_{0.44}$ lattice-matched to InP substrate [1–7] or about its optical properties [8–10]. Quaternary AlGaAsSb has been employed used in integrated Bragg mirror for its low refractive index [2, 11], while GaInAs/AlAsSb are used in quantum cascade lasers [12–14] and inter-subband transition optical switch for its high conduction band offset. Among these applications, a wide range of growth temperatures have been reported from 540 °C [3] to as low as 400 °C [7], although miscibility gap is predicted in a wide range of composition [15]. Actually, clusters of AlAs were observed [5] in AlAsSb alloy grown under low growth rate and low temperature, and these defects can be eliminated by raising growth temperature to above 500 °C. Such elevated temperature poses yet another problem for the growth of $\text{Ga}_{0.47}\text{In}_{0.53}\text{As}$: desorption of indium becomes significant at such elevated temperature. As the first step towards InP-based inter-subband transition application, (Ga)InAs/AlAs_{0.56}Sb_{0.44} structures presented in this thesis were all prepared at 450 °C, which is adapted to the elaboration of other InP-based structures. We leave temperature optimization for future studies.

Another issue concerning the growth of AlAsSb is the segregating nature of antimony. Compared to arsenic, antimony has lower binding energy with cations. The first layers of AlAsSb could be As-rich due to the segregation of Sb. In addition, Sb also has much lower saturating pressure which allows it cumulates on growth surface rather than evaporates into gas phase. This portion of segregated Sb could be incorporated into

subsequent layers and smear the interface between antimonide and antimony-free layers. Special surface termination method can be employed to counteract the segregation of Sb. For example, long-time growth interruption under As_2 -flux can purge accumulated surface Sb [16].

The aforementioned growth conditions described how alloys like $\text{Ga}_{0.47}\text{In}_{0.53}\text{As}$, $\text{AlAs}_{0.56}\text{Sb}_{0.44}$, $\text{Al}_{0.48}\text{In}_{0.52}\text{As}$ and $\text{GaAs}_{0.51}\text{Sb}_{0.49}$ can be grown individually; however, they cannot be grown within the same growth-run, since no set of constant flux can accommodate the growth of these four alloys. This is currently solved by using redundant gallium and indium source-cells.

1.3 Deposition of lattice-mismatched materials on InP substrate

Growth modes of heteroepitaxy

The epitaxial growth of heterostructure may proceed under three distinct growth modes: the Frank van der Merwe mode for two-dimensional layer-by-layer growth, the Stranski-Krastanow mode for layer-plus-island growth, and Volmer-Webber mode for three-dimensional direct island formation; they are illustrated in figure 1.3. The growth mode of a given material system is largely determined by strain energy stocked in the epitaxial thin film ($\epsilon_{\text{strain}}^{2\text{D}}$), the surface energies ($\gamma_2, \gamma_3, \gamma_4$) and interface energy at the substrate-epitaxial thin film interface (γ_1).

For the growth of aforementioned lattice-matched materials like $\text{Ga}_{0.47}\text{In}_{0.53}\text{As}$, its growth mode is solely determined by the interface and surfaces energies. Layer-by-layer growth mode usually occurs if the surface and interface energies introduced by epitaxial layer is lower than the surface energy of matrix ($\gamma_2 + \gamma_1 < \gamma_3$ in figure 1.3). The epitaxial layer is considered to be *wetting* the matrix. Otherwise, the epitaxial growth will proceed under Volmer-Webber growth mode and non-wetting islands are formed.

The growth of lattice-mismatched material is more complicated for it involves strain energy and subsequently strain relaxation. The epitaxial layer may either maintain full coherence with the substrate, form three-dimensional islands that enable partial strain relaxation, or release strain energy by generating defects.

In case of high lattice-mismatch, the strain energy is so dominant that no other energy term can compete with it ($E_{\text{strain}}^{2\text{D}} \gg E_{\text{strain}}^{3\text{D}}$). The epitaxial grown material could directly organize into islands under Volmer-Webber mode.

When the lattice mismatch is intermediate, the system can go under Stranski-Krastanow growth mode : the epitaxial growth maintains two-dimensional wetting-layer until a critical thickness is reached. The system then switches to three-dimensional mode, forming islands upon the wetting layer. The *critical thickness for two-dimensional-to-three-dimensional transition* depends on material system and growth conditions. For

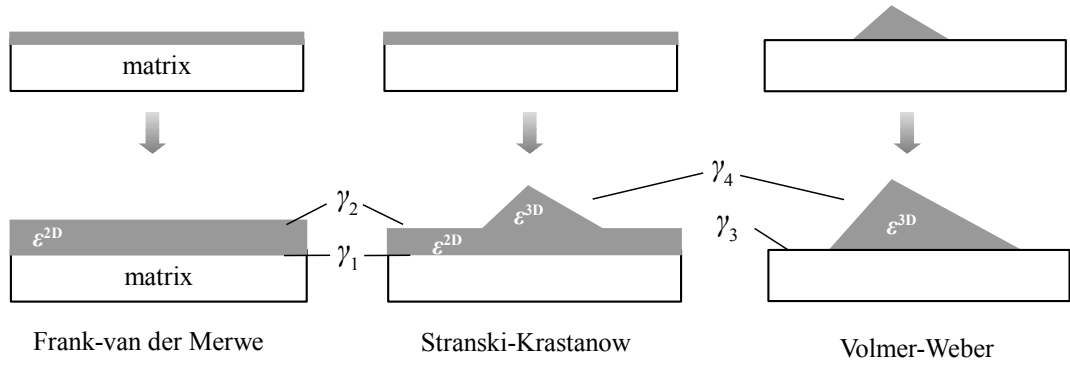


Figure 1.3: Three growth modes of heteroepitaxy : Frank-van der Merwe, Volmer-Webber, and Stranski-Krastanow.

example, a critical thickness of 1.5–1.8 mono-layer (ML) is determined for InAs deposition on GaAs under a wide range of growth conditions, and a wetting layer of similar thickness can still be observed by *ex situ* observations like cross-sectional scanning tunneling microscope [17]. Stranski-Krastanow growth mode is crucial to self-assembled InAs quantum dots, for they can produce coherently strain islands that powers devices like quantum-dot lasers.

Strain relaxation

Coherently strained layer or coherent islands can exist during the initial stage of deposition; however, their growth cannot proceed without limit. The lattice strain will cumulate until a critical thickness, beyond which strain energy would be released via elastic relaxation by generating undulation, or via plastic relaxation by generating dislocations and other defects. These different ways of strain relaxation are illustrated in figure 1.4. Neither of these relaxation is desired, since they degrade electronic properties and device performance.

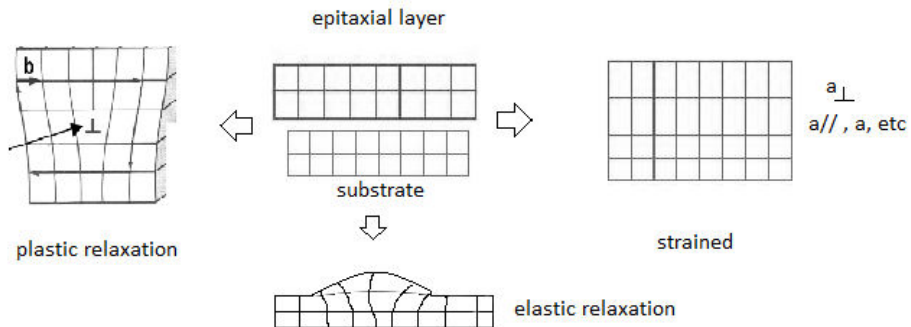


Figure 1.4: Coherent epitaxial layer, elastic relaxation and plastic relaxation

The degree of relaxation of a epitaxial thin film can be determined by measuring

its lattice constants. As is demonstrated in figure 1.4, fully coherent epitaxial layer is subject to elastically tetraorthogonal deformation. Its in-plane lattice constant a_{\parallel} is deformed to match that of substrate a_{sub} , while its vertical lattice constant a_{\perp} can be estimated by :

$$a_{\perp} = a_0 - \frac{2\nu}{1-\nu}(a_{\text{sub}} - a_0) \quad (1.1)$$

in which a_0 is relaxed lattice constant of epitaxial material, and ν represents its Poisson's ratio. The vertical lattice constant a_{\perp} can be easily determined by X-ray diffraction measurements, and deviation from the value predicted in equation (1.1) signifies strain relaxation.

The *critical thickness for plastic relaxation* h_c can be estimated by calculations prior to actual growth. Matthews and Blakeslee [18] proposed a criterion for plastic relaxation based on the movement of dislocations, which can often give an idea about the limit of pseudomorphic growth regime [19] ¹:

$$h_c = \frac{|\mathbf{b}|}{2 \cdot 4 \cdot \pi f} \frac{1 - \nu \cos^2 \theta}{(1 + \nu) \cos \lambda} \ln \left(\frac{h_c}{|\mathbf{b}|} + 1 \right) \quad (1.2)$$

a_{\parallel} is the lattice constant of substrate, $f = (a_{\text{sub}} - a_0)/a_0$ is the misfit between epitaxial material and substrate, and ν is the Poisson's ratio of epitaxial layers. If we choose the most prevalent 60° dislocation in zinc-blende structure, its Burgers vector $|\mathbf{b}| = a_{[101]}/2 = \sqrt{2}a_0/2$, and direction cosines $\cos \theta = \cos \lambda = 1/2$. Poisson ratio ν is taken as $1/3$, a good approximation for many compound semiconductor materials. Compared to the original expression of Matthews-Blakeslee, the first factor of equation (1.2) has an extra denominator 4. It counts for the fact that epitaxial thin film is constraint only from one side [19]. Equation (1.2) is solved over a wide range of misfit and corresponding solutions are shown in figure 1.5.

The lattice constant of InAs is 3.2% larger than that of InP, and its critical thickness for plastic relaxation is only about 1.7 nm (~ 3 ML) by the criterion of Matthews-Blakeslee. Due to its band-gap as low as 0.4 eV, strained InAs quantum wells on InP substrate can potentially extend the working wavelength of InP-based device to mid-infrared range. In reality, InAs deposition on InP goes under Stransky-Krastanov growth mode upon 1–2 ML (0.3–0.6 nm) deposition, which limits its emission wavelength below 2 μm .

Surfactant effect and Sb

The growth mode of InAs can be significantly modified by the deliberate introduction of surfactant atoms like Sb. The use of Sb is known to help maintain two-dimensional growth mode of lattice-mismatched epitaxial layers [20, 21]. By applying Sb flux during

¹This critical thickness for *plastic relaxation* is different from critical thickness for *growth-mode transition*.

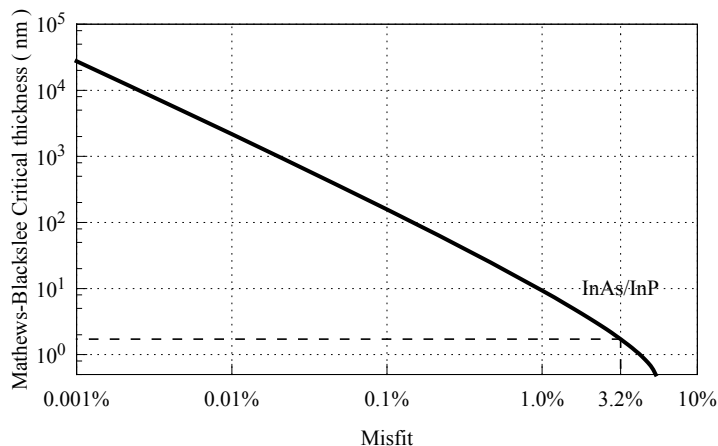


Figure 1.5: Critical thickness for plastic relaxation obtained by Matthews-Blackslee formula 1.2

their deposition, thick and yet defect free InAs layer of high quality was obtained on InP substrate, and yet the incorporation level of Sb was negligible [21]. The use of surfactant was taken as surface energy modifications, which increase energy barrier for strain relaxation [22]. The use of surfactant was also considered to shift the balance between competition between elastic and plastic relaxation [22] and subsequently critical thickness for dislocation generation as well as critical thickness for elastic relaxation [20]. We attempt to achieve 1.55 μm inter-subband transition within strained InAs/AlAs_{0.56}Sb_{0.44} quantum wells. The limit of such Sb-assisted growth as well as its relaxation behavior is studied in chapter 3.

The effect of surfactant is also taken as modification of surface diffusivity of Indium ad-atom, and a surfactant atoms can enhance or reduced diffusion length of cation ad-atom [23]. In these scenario, the surfactant effect of Sb is attributed to its complete surface coverage: arriving ad-atoms are instantly swapped with sub-surface Sb atoms and by consequence their surface mobility is significantly reduced. [20, 24]. Such kinetic diffusion blocking has also been employed to explain high density and uniform quantum dot that were obtained under the influence Sb [25].

It has been demonstrated that the use of surfactant can modify the equilibrium shape of strained Ge/Si deposition, and degree of energy modification is considered facet orientation dependent [26]. In chapter 4, the effect of Sb on the deposition of strained InAs is again examined on both (001) and (113)B surfaces of GaAs_{0.51}Sb_{0.49}. As a matter of fact, very different behaviors were obtained. These results will be presented in detail in chapter 4, which allow more insight into the mechanism of surfactant effect than pure.

References

- [1] S. Németh et al., “Compositional dependence of $\text{AlAs}_y\text{Sb}_{1-y}$ ternaries on the ratio of Sb/As fluxes and on the substrate temperature”, *Journal of Applied Physics* **77**, 3552–3553 (1995).
- [2] J. Harmand et al., “Molecular beam epitaxy of AlGaAsSb system for 1.55 μm bragg mirrors”, *Journal of Crystal Growth* **175–176, Part 1**, 372–376 (1997).
- [3] E. Hall et al., “Improved composition control of digitally grown AlAsSb lattice-matched to InP”, *Journal of Crystal Growth* **203**, 447–449 (1999).
- [4] R. Kaspi and G. P. Donati, “Digital alloy growth in mixed As/Sb heterostructures”, *Journal of Crystal Growth* **251**, 515–520 (2003).
- [5] G. Boishin et al., “AlAs-in-AlSb digital alloy superlattice morphology versus growth temperature”, *Journal of Crystal Growth* **286**, 32–36 (2006).
- [6] W. LU, “Elaboration par épitaxie par jets moléculaires et caractérisation de nanostructures à base d’antimoine sur substrats InP”, PhD thesis (Institut National des Sciences Appliquées de Rennes, Rennes, France, 2010), 214 pp.
- [7] Y. Fedoryshyn, “Modeling, growth and characterization of InGaAs/AlAsSb quantum well structures for all-optical switching based on intersubband transitions”, PhD thesis (Swiss Federal Institute of Technology Zurich, Zürich, 2012).
- [8] T. Mozume et al., “Indices of refraction of AlGaAsSb by an optical waveguide technique”, *Journal of Applied Physics* **102**, pages (2007).
- [9] T. Mozume et al., “Optical functions of AlAsSb characterized by spectroscopic ellipsometry”, *physica status solidi (a)* **205**, 872–875 (2008).
- [10] J. Y. Kim et al., “Optical properties of $\text{AlAs}_x\text{Sb}_{1-x}$ alloys determined by in situ ellipsometry”, *Applied Physics Letters* **103**, pages (2013).
- [11] O. Ostinelli, “Long wavelength VCSELs with MOVPE grown AlGaAsSb/InP bragg reflectors”, Doctor of Natural Sciences (Swiss Federal Institute of Technology Zurich, Zurich, 2006), 127 pp.
- [12] J. P. Commin et al., “High peak power 3.3 and 3.5 μm InGaAs/AlAs(Sb) quantum cascade lasers operating up to 400 K”, *Applied Physics Letters* **97**, pages (2010).
- [13] C. Deutsch et al., “InGaAs/GaAsSb/InP terahertz quantum cascade lasers”, *Journal of Infrared, Millimeter, and Terahertz Waves* **34**, 374–385 (2013).
- [14] C. Manz et al., “High-quality GaInAs/AlAsSb quantum cascade lasers grown by molecular beam epitaxy in continuous growth mode”, *Journal of Crystal Growth* **280**, 75–80 (2005).
- [15] J. Pessetto and G. Stringfellow, “ $\text{Al}_x\text{Ga}_{1-x}\text{As}_y\text{Sb}_{1-y}$ phase diagram”, *Journal of Crystal Growth* **62**, 1–6 (1983).
- [16] R. Kaspi and K. R. Evans, “Sb-surface segregation and the control of compositional abruptness at the GaAsSb/GaAs interface”, *Journal of Crystal Growth* **175–176, Part 2**, 838–843 (1997).
- [17] Y. H. Wu et al., “Structural and optical properties of buried InAs/GaAs quantum dots on GaAsSb buffer layer”, *Journal of Physics D: Applied Physics* **42**, 185106 (2009).
- [18] J. Matthews and A. Blakeslee, “Defects in epitaxial multilayers: i. misfit dislocations”, *Journal of Crystal Growth* **27**, 118–125 (1974).
- [19] S. M. Hu, “Misfit dislocations and critical thickness of heteroepitaxy”, *Journal of Applied Physics* **69**, 7901–7903 (1991).
- [20] J. C. Harmand et al., “GaInAs/GaAs quantum-well growth assisted by sb surfactant: toward 1.3 μm emission”, *Applied Physics Letters* **84**, 3981–3983 (2004).
- [21] C. Gatel et al., “Analysis by high-resolution electron microscopy of elastic strain in thick InAs layers embedded in $\text{Ga}_{0.47}\text{In}_{0.53}\text{As}$ buffers on InP(0 0 1) substrate”, *Acta Materialia* **58**, 3238–3246 (2010).
- [22] J. Tersoff and F. K. LeGoues, “Competing relaxation mechanisms in strained layers”, *Physical Review Letters* **72**, 3570–3573 (1994).

1.3. Deposition of lattice-mismatched materials on InP substrate

- [23] J. Massies and N. Grandjean, “Surfactant effect on the surface diffusion length in epitaxial growth”, [Physical Review B](#) **48**, 8502–8505 (1993).
- [24] C. W. Snyder and B. G. Orr, “Comment on “Delayed relaxation by surfactant action in highly strained III-V semiconductor epitaxial layers””, [Physical Review Letters](#) **70**, 1030–1030 (1993).
- [25] N. Kakuda et al., “Sb-mediated growth of high-density InAs quantum dots and GaAsSb embedding growth by MBE”, [Applied Surface Science](#) **254**, 8050–8053 (2008).
- [26] D. J. Eaglesham et al., “Growth morphology and the equilibrium shape: the role of “surfactants” in Ge/Si island formation”, [Physical review letters](#) **70**, 966–969 (1993).

Chapter 2

The Growth of $\text{Ga}_{0.47}\text{In}_{0.53}\text{As}/\text{AlAs}_{0.56}\text{Sb}_{0.44}$ Quantum Wells for Inter-subband Applications

Inter-subband transition between two conduction-band subbands in a quantum well allows very flexible band-engineering due to its high dependence on structure parameters. It has brought about many device applications like long-wavelength photo-detector [1], mid-infrared quantum cascade laser [2] and near-infrared optical switch [3]. Section 2.1 begins this chapter with a physical description of inter-subband transitions and how it enables ultrafast light-signal modulation at 1.55 μm telecommunication band. Following that the state of art on GaInAs/AlAsSb optical switch will be shortly presented. Section 2.2 and 2.3 will present our first efforts in making such optical switch via a series of studies on the interband and inter-subband properties in $\text{Ga}_{0.47}\text{In}_{0.53}\text{As}/\text{AlAs}_{0.56}\text{Sb}_{0.44}$ quantum wells. Near infrared inter-subband absorption was eventually observed but the goal of 1.55 μm was left unfulfilled. Section 2.4 and 2.5 launch different optimizations together with microscopic observations of such quantum-well structures, in order to have a closer look at all kinds of imperfections that could have prevented us from obtaining 1.55 μm inter-subband absorption.

2.1 Inter-subband transition and devices

Physical descriptions of inter-subband transition

In a quantum well illustrated in figure 2.1, the energy separation between the ground state (E_1) and the first-excited state (E_2) is roughly approximated by:

$$E_2 - E_1 = \frac{3 \hbar^2}{2m^*} \left(\frac{\pi}{L} \right)^2 \quad (2.1)$$

In this estimation, the quantum well is considered as an infinite potential well, and L marks its extent (thickness). The conduction-band dispersion is assumed to be parabolic so that the effective mass of electron m^* is constant in the quantum well. Such estimation reveals that the inter-subband transition energy is highly dependent on L . For example, in a 10 nm-thick $\text{Ga}_{0.47}\text{In}_{0.53}\text{As}$ quantum well¹, inter-subband transition energy associated with first conduction-band subbands is about 260 meV, which corresponds to a wavelength of 4.8 μm in the mid-infrared band. Meanwhile, when L is reduced to 6 nm, its inter-subband transition energy becomes as high as 0.8 eV and its wavelength lies in 1.55 μm telecommunication band.

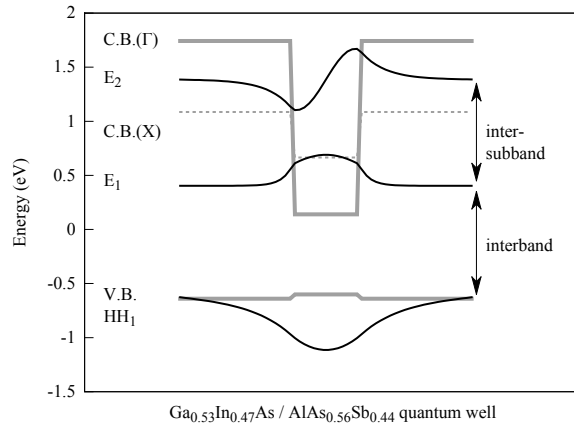


Figure 2.1: Conduction-band subbands in a single quantum well. The gray lines describe the band line-up of GaInAs/AlAsSb quantum well, while the black curves depict the wave-functions envelope superposed on their energy levels.

Like inter-band transitions, both photon emission and absorption can take place via inter-subband transition, leading to different applications like quantum cascade lasers [5] or quantum-well inter-subband photo-detector [1]. The absorption coefficient associated

¹Electron effective mass m_{Γ}^* is taken as $0.043 m_e$ [4].

with inter-subband transition from E_1 to E_2 can be estimated by [6, pp. 299–301]:

$$\alpha_{E_1-E_2}(\hbar\omega) \propto e_z^2 \langle \varphi_2 | z | \varphi_1 \rangle^2 (N_1 - N_2) \frac{\Gamma/2}{(E_2 - E_1 - \hbar\omega)^2 + (\Gamma/2)^2} \quad (2.2)$$

in which e_z is the electric field component of incident radiation projected in quantum confinement direction (z)². This term indicates that in a ridge wave-guide (figure 2.2a), inter-subband transition interacts with transverse-magnetic (TM) polarized light but not with transverse-electric (TE) polarized light. φ_1 (φ_2) is the envelope of electron wave-function corresponding to eigenstate E_1 (E_2), which carries information on spatial distribution of electron wave-function. The dipole matrix element $\langle \varphi_2 | z | \varphi_1 \rangle$ indicates that inter-subband transition is weak where two wave-functions hardly overlap or when they have the same parity. In practice, such selection rules could be relaxed by asymmetric potential profile which breaks its mirror symmetry, as well as strain which induces band mixing. N_1 (N_2) represents the electron population in the conduction-band ground state (first excited state). This term indicates that the conduction-band ground-state must be sufficiently populated for experimental observation of inter-subband absorption. The last term originates from energy conservation which requires the absorbed photon has the same energy as the separation between subbands $\hbar\omega = E_2 - E_1$. It adds phenomenological broadening characterized by Lorentzian with line width Γ . This suggests that an inter-subband absorption spectrum appears as individual absorption peak, rather than step-like absorption spectrum in the case of inter-band transition in a quantum well.

Inter-subband transition optical switch

The polarization-dependent nature of inter-subband absorption allows independent control of inter-band and inter-subband processes by using TE- and TM-polarized light. This is illustrated in figure 2.2b using a three-level quantum well, of which the conduction-band ground level is populated by high-level of doping. Without inter-subband excitation, TE-polarized probing photon that correspond to the effective-gap of quantum well can pass through the structure without large attenuation, because the final states of inter-band transition is already occupied by electrons coming from dopant atoms and thus absorption is prohibited. Under the presence of intense TM-polarized pumping, the conduction-band ground level (E_1) is bleached by inter-subband transition so that the previously prohibited inter-band transition is now allowed and this will eventually induce high attenuation to the TM-polarized probe-light. In essential, this simple scheme enables the modulation of light and it is employed in experimental study of inter-subband relaxation dynamics.

An alternative scheme, coupled-double-quantum-well has successfully demonstrated

² z is also the growth direction.

demultiplexing operation at a frequency of about 1 THz [7]. When two quantum wells are strongly coupled, each of the previously degenerated E_1 E_2 states would unfold into two states and thus the double quantum-wells becomes a four-level system. This is similar to what is illustrated in figure 2.2c. The signal light is adapted to the transition from E_2 to E_3 , while control-light is adapted to transition from E_1 to E_4 . Without inter-subband excitation, E_2 to E_3 transition is allowed so that the attenuation of probe-light is strong and the structure is in its “OFF” state. Under the excitation of strong control-light, the lower levels are bleached so that E_2 to E_3 transition is prohibited and the probe-light can pass through the structure without attenuation and the switch is in its “on” state. This scheme thus also allows the implementation of “ON/OFF” modulation. Additionally, inter-subband excitation can induce refractive-index change for TE polarized probe-light near inter-band energy, so that the structure also allows cross-phase modulation between pump and probe-light [8, 9].

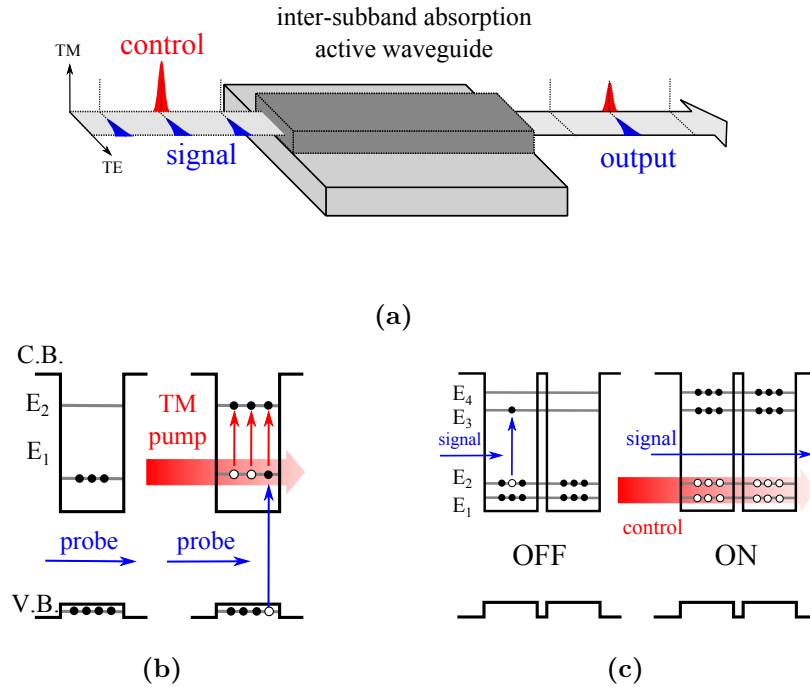


Figure 2.2: Inter-subband transition based light-signal modulation. (a) illustrates a ridge wave-guide typically used in inter-subband modulators. (b) presents optical modulation using three-level system in a single quantum well. (c) presents a four-level scheme using a coupled-double quantum well.

Eligible material systems

Usually, phonon-assisted inter-subband relaxation has characteristic time in the order of pico-second (10^{-12} s), which is well adapted for optical applications operating at terahertz (10^{12} Hz) repetition rate. To operate in the $1.55 \mu\text{m}$ optical telecommunication

band, the hosting structure should have sufficiently large confinement potential to host two conduction-band sub-bands separated by 0.8 eV (1.55 μm). Essentially, this requirement calls for large conduction-band offset. Three eligible material systems are currently being studied for applications based on inter-subband transition.

II-VI semiconductor CdS(/ZnSe)/BeTe quantum well has a conduction-band offset as large as 3.1 eV, and it has been researched in optical switching applications in 1.55 μm band. It allows a fast inter-subband relaxation with decay time lower than 600 fs, and it enables 10 dB light switching using excitation pulse of about 7 pJ/ μm^2 [10]. Although all the materials involved in this II-VI structure have similar lattice-constants, they have no common element. The interface treatment is rather complicated: different bonding schemes could result in lattice-mismatch up to 10%, which can significantly influence device performance [11–13]. At the same time, no perfect substrate is commercially available for these II-VI semiconductor structure and they are elaborated on GaAs substrate with a lattice-mismatch of about 0.3%.

Wurtzite III-V GaN/AlGaIn quantum well also offers a conduction band offset as large as 2 eV. It enables continuously adjustable inter-subband transition wavelength which covers both 1.3 μm and 1.55 μm telecommunication bands. Due to the strong coupling between electrons and longitudinal-optical-mode phonons, inter-subband relaxation time in this material can be as short as 100 fs. Usually, wurtzite GaN-based material are elaborated on sapphire or SiC substrates, which could raise concerns in the crystal quality of epitaxial thin-film. Also, the spontaneous polarization due to piezo-electric effect should be carefully handled, which breaks the mirror symmetry of a quantum well and subsequently the polarization selection rules of inter-subband absorption. [14, 15]

InP-based Ga_{0.47}In_{0.53}As/AlAs_{0.56}Sb_{0.44} quantum wells also have a conduction band offset as large as 1.6 eV [4], which makes it eligible for 1.55 μm inter-subband applications.

State of art of Ga_{0.47}In_{0.53}As/AlAs_{0.56}Sb_{0.44} quantum wells for optical switch

1.55 μm inter-subband absorption in Ga_{0.47}In_{0.53}As/AlAs_{0.56}Sb_{0.44} quantum wells was first reported by Mozume *et al.* [16] and this material system have shown inter-subband relaxation time as short as 0.8 ps [17] (1.3 ps by [18]). In this material system, the absorption coefficient of TM-polarized light was found to be highly nonlinear, which was attributed to both the nonlinearity of inter-subband absorption at intermediate input power and two-photon absorption at high excitation power regime [19]. Such nonlinearity makes them suitable for applications like noise filter or saturable absorber. At the same time, the inter-subband transition energy in this system was found to be very stable against temperature variation [20], which ensures stable performance under fluctuating working conditions.

The GaInAs/AlAs/AlAsSb coupled-double quantum well is a structure that is used

by many research groups to achieve 1.55 μm inter-subband transition; figure 2.9a (page 30) presents a structure similar to it. The interaction between two quantum wells pushes inter-subband transition to higher energies than in a single quantum well. The inter-subband relaxation time in such a structure was found to be even shorter than 0.7 ps [21]. It has even higher inter-subband absorption nonlinearity, of which saturates at pulse energy density as low as 10 fJ/ μm^2 [22]. ON/OFF modulation at 1 THz was achieved with a GaInAs/AlAsSb coupled-double quantum well waveguide [7], and it has demonstrated reliable room temperature demultiplexing operation [23]. Furthermore, this four-level system enable efficient (0.5 rad/pJ) cross-phase modulation between control and signal light [8, 9] .

In this chapter, we will layout the foundation for the research of inter-subband transition applications based on InP substrate. In section 2.2 and section 2.3, Ga_{0.47}In_{0.53}As/AlAs_{0.56}Sb_{0.44} quantum wells will be studied for its optical properties associated with inter-band and inter-subband transition.

2.2 Inter-band properties of Ga_{0.47}In_{0.53}As/AlAs_{0.56}Sb_{0.44} multiple quantum wells

Determination of optimal quantum well thickness

To determine the exact Ga_{0.47}In_{0.53}As/AlAs_{0.56}Sb_{0.44} structure that is required to reproduce inter-subband transition at 1.55 μm , transition energies in GaInAs/AlAsSb quantum wells were examined using empirical tight-binding calculations. In these calculations, the multiple quantum well structure is modeled by super-cells containing 34 ML of AlAs_{0.56}Sb_{0.44} and from 5 to 22 ML of Ga_{0.47}In_{0.53}As while the electron wave-function are expended using an extended *spds**-basis[24]. The calculations were performed by Soline Richard (FOTON).

The calculation results are reported in figure 2.3, in terms of inter-subband transition energies at different Ga_{0.47}In_{0.53}As layer thickness. These results indicate inter-subband transition energy as high as 0.9 eV (1.37 μm) can be achieved by a 5 ML (1.5 nm) thick GaInAs quantum well. To achieve inter-subband transition at 1.55 μm (0.8 eV), the Ga_{0.47}In_{0.53}As layer thickness has to be as small as 7 ML (2.1 nm). Such small thicknesses pose stringent requirement on the control of quantum well thickness and they demand high-quality interfaces between the material layers; 1 ML quantum well thickness derivation would lead to inter-subband energy shift of around 70 meV, which correspond to 150 nm wavelength-shift.

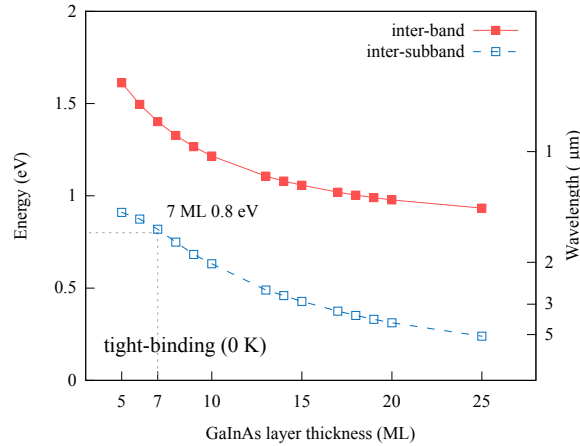


Figure 2.3: Tight-binding simulated inter-band and inter-subband transition energies in $\text{Ga}_{0.47}\text{In}_{0.53}\text{As} / \text{AlAs}_{0.56}\text{Sb}_{0.44}$ single quantum wells.

Inter-band properties

Three GaInAs/AlAsSb multiple quantum-well samples were prepared for the study of their inter-band properties. Their structure is illustrated in figure 2.4a: within each period of these samples, the AlAsSb barrier thickness is fixed to 10 nm, and the GaInAs layer thicknesses is chosen to be 7 ML (sample S1078), 14 ML (S1079) and 19 ML (S1080). Each sample was made to contain 10 periods of quantum wells and no intentional doping were applied to the quantum wells. These structures were grown on conductive InP (001) substrates using solid source MBE, under the conditions described in section 1.2 (page 9). To protect the Al-containing layers from oxidation in the air, each of these samples was finished by a 5 nm-thick $\text{GaAs}_{0.51}\text{Sb}_{0.49}$ layer.

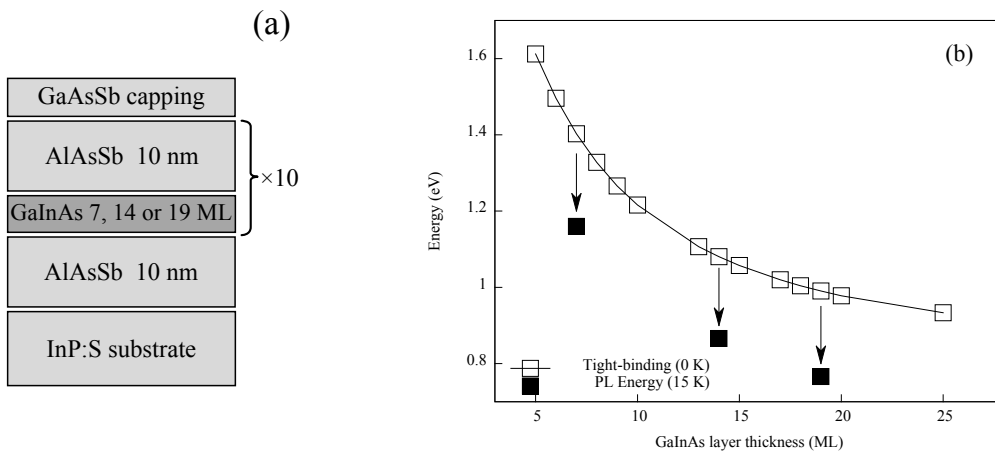


Figure 2.4: (a) Structures of samples S1078–S1080 (b) Calculated transition energies (0K) compared to PL energies recorded at 10 K. The excitation power density was 4 kW/cm^2 .

PL spectra of these samples were recorded under temperature ranging from 15 K

up to about 250 K. A 532-nm laser was used as excitation source and the maximum excitation power density was about 4 kW/cm^2 . Figure 2.4b presents a comparison of PL peak energies obtained at 15 K along with those tight-binding calculated inter-band transition energies. The PL energies follow the same trend as the calculations but they are systematically lower than calculated values by about 200 meV. Many factors could be responsible for such large difference, including the accuracy of calculations, the error in quantum well thickness and the unintentional incorporation of Sb in GaInAs layer.

Precision of quantum well thickness

In order to examine the possible deviation of quantum well thickness, the structural parameters of these quantum-well samples were checked by X-ray diffraction (XRD). $\omega-2\theta$ scans were performed to find out the periodic thickness of these quantum wells, namely the thickness of GaInAs layer plus that of AlAsSb layer. All the measured quantum-well periods are found to be smaller than their nominal values by about 4-5 ML. The ‘missing thicknesses’, that is, the difference between experimentally measured thickness and those intended, are plotted in figure 2.5 versus their nominal thickness. The ‘missing’ period thickness is actually linearly correlated to the nominal quantum-well thickness. This could be a result of rounding error in MBE growth rate calibration. Since the only varying parameter among all three samples is the GaInAs layer thickness, the slope formed by the three data points thus stands for the error in GaInAs growth rate, which is about 10%.

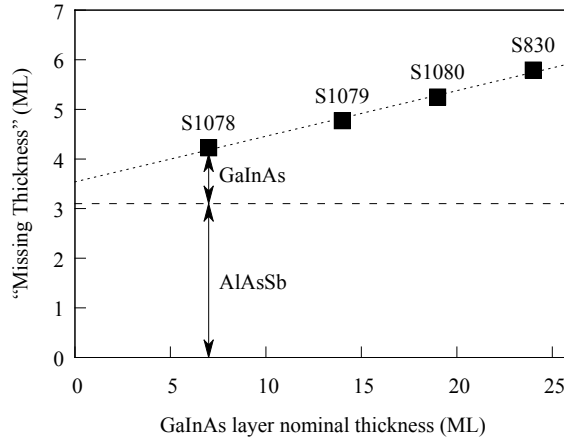


Figure 2.5: Missing thicknesses in GaInAs/AlAsSb quantum wells.

The error in growth rate calibration can be subtracted by extrapolating the ‘missing thickness’ to zero-GaInAs thickness and the intersection in figure 2.5 shows that there’s still 3.5 ML missing. To attribute the ‘missing thickness’ to the GaInAs and AlAsSb layers composing each quantum well period, we performed X-ray reflectivity on one of these samples. The result reveals that in each period of $\text{Ga}_{0.47}\text{In}_{0.53}\text{As}/\text{AlAs}_{0.56}\text{Sb}_{0.44}$

quantum well sample S1078, about 1.1 ML of thickness is missing from GaInAs layer, and 3.1 ML was missing within the AlAsSb layer. Therefore, out of the 3.5 ML missing, 3.1 ML is contributed by AlAsSb layer, leaving the segregation of indium to be the last possible source of 0.4 ML ‘missing thickness’.

The above structural analysis gives an estimation of the magnitude of indium segregation as well as a better growth rate calibration. But the detected thickness error is still too small to cause the observed 200 meV difference between experimental PL energies and calculated inter-band energies.

Unintentional incorporation of Sb

Sb is known to segregate during MBE growth and it can get unintentionally incorporated into layers that next to antimonide alloys. In fact, elemental Sb can stay on the growth front for a while even after its supply is interrupted [25]. To evaluate the Sb-incorporation level in GaInAs/AlAsSb quantum well, we have simulated inter-band transition energy in $\text{Ga}_{0.53}\text{In}_{0.47}\text{As}_{1-y}\text{Sb}_y$ / $\text{AlAs}_{0.56}\text{Sb}_{0.44}$ single quantum wells using $k \cdot p$ method. In figure 2.6, the calculated energies given in empty squares are compared with PL energies in filled squares. The PL energies seem to coincide with calculated energies for $y = 20\%$ and they seem to indicate the unintended Sb-incorporation level in GaInAs layer could be about 20%, which is unexpectedly high. Microscopic studies is required to confirm such high level of unintentional incorporation of Sb, and this issue will be addressed in later section 2.4 using cross-sectional scanning tunneling microscopy.

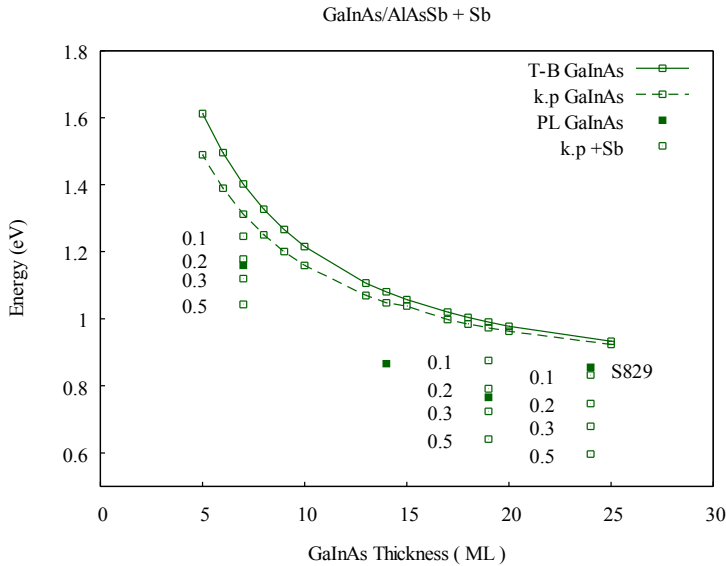


Figure 2.6: Calculated inter-band transition energy under different levels of Sb-incorporation in GaInAs(Sb) layer.

2.3 Inter-subband properties of Ga_{0.47}In_{0.53}As/AlAs_{0.56}Sb_{0.44} multiple quantum wells

Effect of doping

Beside good control of quantum well thickness, another important aspect of achieving strong inter-subband transition is to sufficiently populate conduction-band ground state. This is commonly accomplished by high level n -doping using Si. Sheet carrier densities higher than $1 \times 10^{12} \text{ cm}^{-2}$ is being used by many research groups [17, 19]. For a quantum well as thin as 2 nm, it requires a bulk doping level of about $1 \times 10^{19} \text{ cm}^{-3}$. We first performed calibration on n -doping in GaInAs with bulk GaInAs sample. With the maximum Si flux and modest GaInAs growth rate of 0.2 ML/s, a doping level of $5 \times 10^{18} \text{ cm}^{-3}$ can be achieved.

Being aware that high-level of Si doping could introduce addition disorder at the GaInAs/AlAsSb interface [26, 27], two GaInAs/AlAsSb multiple-quantum well samples S1309 and S1310 were prepared to evaluate the impact of doping in such structures. They were elaborated under the same conditions as previous GaInAs/AlAsSb structures and they have the same structures as previous samples except for that the thickness of GaInAs layer is fixed to 7 ML (2.1 nm) . The GaInAs layers in sample S1309 is doped with Si while sample S1310 is kept intact for comparison.

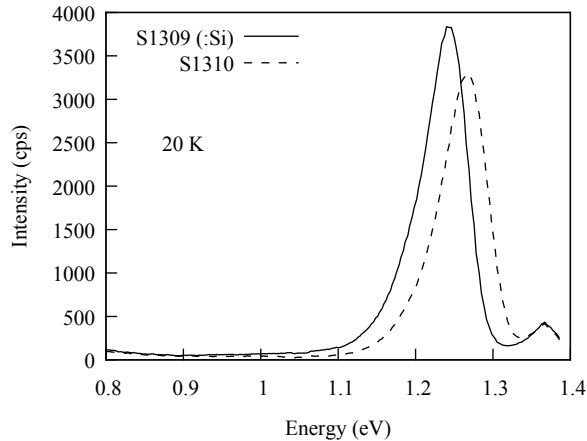


Figure 2.7: Low temperature PL spectra of sample S1309 and S1310. The incident laser power density was about 4 kW/cm^2 .

The two samples are characterized by PL from 20 K up to room temperature. Figure 2.7 displays low temperature PL spectra of these two samples obtained under 20 K, while other PL characteristics are summarized in table 2.1. Compared with the non-doped sample S1310, doping in sample S1309 has led to neither broadening nor additional peaks that were observed in reference [27]. On the contrary, the Si-doped sample has a very similar line width as the non-doped sample. And it even demonstrates higher

Table 2.1: PL characteristics of sample S1309 and S1310

Sample	Peak energy (eV)		Line width (meV)		E_A (meV)
	24 K	300K	24 K	300 K	
S1309	1.244	1.21	74	123	25.7
S1310	1.27	1.24	79	121	25.0

thermal activation energy E_A for non-radiative process. These PL results indicate no serious degradation was caused by doping.

Absorption measurement using a multi-pass waveguide

In order to observe the interaction between incident-light and inter-subband transitions, it is necessary to couple the incident-light into transverse-magnetic (TM) mode in the quantum wells. A ridge waveguide illustrated in figure 2.2a has 100% TM-mode coupling efficiency. Nevertheless, fabrication of such a structure requires knowledge in technological process of AlAsSb; without proper treatment, an AlAsSb-based ridge could oxide by its lateral facets [28] and breaks down in the atmosphere. Alternatively, the multiple reflection waveguide is a commonly adopted solution in optical studies, since it can be easily fabricated and yet it has TM-mode coupling efficiency as high as 71% [29]. Figure 2.8 shows a schematic representation of such a waveguide, which is obtained by shaping epitaxial samples into slabs with parallelogram cross-sections.

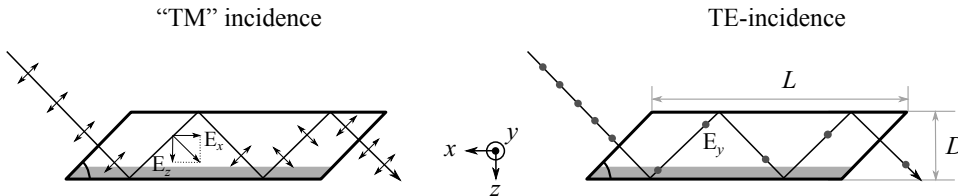


Figure 2.8: Geometry of a multi-pass waveguide. Double-headed arrows stand for p -polarized light whose electric-field vector lies in the paper, and dots represents s -polarized light whose electric-field is perpendicular to the paper.

Due to the strong refractive index contrast between the air and semiconductor materials, the internal surfaces of the waveguide are total-reflective for a large range of angles. Light entering from the facets of parallelogram slabs can propagate along a zigzag path inside the waveguide. For the parallelogram waveguide draw in 2.8, light travels a distance of $l = \sqrt{2}L$ in the guide and it passes through the epitaxial layers $2N$ times, where $N = \lfloor L/2D + 1/2 \rfloor$. The length of waveguide L has to be sufficiently long so that attenuation due to the absorption of epitaxial layer can be easily detected.

When s -polarized light enters such a sample, it transmits in “pure” TE-mode and its

electric field vector is parallel to the in-plane direction (y) with regard to the quantum wells. Its transmittance can be described as

$$T_{\text{TE}} = \exp[-(\alpha_{\text{E}_1\text{-HH}_1,y} + \alpha_{\text{E}_1\text{-LH}_1,y} + \alpha_{\text{others}}) \cdot l] \quad (2.3)$$

in which $\alpha_{\text{E}_1\text{-HH}_1}$ is absorption coefficient associated with heavy-hole to conduction-band transition. $\alpha_{\text{E}_1\text{-LH}_1,y}$ stands for absorption due to the interaction TE-polarized light and light-hole to conduction-band process.³ All other polarization-independent optical loss are included in α_{others} .

When p -polarized light passes through the wave-guide, it transmits in “TM”-mode — which is not exactly the same as the TM-mode in a ridge waveguide. The electric-field of propagating light is 45° away from both z and x directions so that it interacts with both inter-subband ($\text{E}_1\text{-E}_2$) process and inter-band processes ($\text{HH}_1\text{-E}_1$, $\text{LH}_1\text{-E}_1$) :

$$T_{\text{TM}} = \exp\left[-\left(\frac{\alpha_{\text{HH}_1\text{-E}_1,x} + \alpha_{\text{LH}_1\text{-E}_1,x} + \alpha_{\text{others}}}{2} + \frac{\alpha_{\text{LH}_1\text{-E}_1,z} + \alpha_{\text{E}_1\text{-E}_2} + \alpha_{\text{others}}}{2}\right) \cdot l\right] \quad (2.4)$$

Here, we acknowledge that $\text{HH}_1\text{-E}_1$ process only interacts with electric field vector parallel to in-plane directions (x and y), while $\text{LH}_1\text{-E}_1$ process interact with both in-plane electric field vector and out-of-planes ones, resulting in absorption coefficients $\alpha_{\text{LH}_1\text{-E}_1,x}$ and $\alpha_{\text{LH}_1\text{-E}_1,z}$, respectively⁴. Eventually, polarization dependent absorption can be extract by comparing TE and “TM” absorption spectra :

$$\ln \frac{T_{\text{TE}}(\lambda)}{T_{\text{TM}}(\lambda)} = [\alpha_{\text{inter-subband}}(\lambda) - \alpha_{\text{interband}}(\lambda)] \cdot \frac{l}{2} \quad (2.5)$$

where all contribution from inter-band process ($\text{HH}_1\text{-E}_1$, $\text{LH}_1\text{-E}_1$) are generalized in $\alpha_{\text{interband}}(\hbar\omega)$.

The above discussions even apply to situations where inter-band and inter-subband energies are not well separated, and subsequently their contributions to polarization dependent absorption cannot be easily isolated. However, in many cases, inter-subband and inter-band energies are well separated. In one hand, at the wavelength range where inter-subband absorption occurs, $\alpha_{\text{HH}_1\text{-E}_1}$ is supposed to be 0 so that in practice $\log_{10}(T_{\text{TE}}/T_{\text{TM}}) \propto \alpha_{\text{E}_1\text{-E}_2}$ is commonly used to present the inter-subband absorption, which appear as a peak centered at $\hbar\omega = E_2 - E_1$. On the other hand, at the wavelength range where inter-band absorption occurs, $\alpha_{\text{E}_1\text{-E}_2}$ is supposed to be 0, thus inter-band absorptions $\alpha_{\text{inter-band}}$ will appear in $\log_{10}(T_{\text{TE}}/T_{\text{TM}})$ plot as a valley. The above discussions only apply to perfect quantum wells. In reality, the polarization selection-rules may be relaxed due to asymmetric quantum well profile, strain and all kinds of inhom-

³Here we only try to deal with transitions related to E_1 or E_2 ; absorption related to higher subband or inter-valence-band absorption are not taken into account.

⁴The projections of $\text{LH}_1\text{-E}_1$ dipole moment along x (y) and z directions are different, so the values of $\alpha_{\text{LH}_1\text{-E}_1,x}$ and $\alpha_{\text{LH}_1\text{-E}_1,z}$ are also expected to be different.

geneity.

The absorption contributed by InP substrate is not yet taken into account in above discussion. InP has a direct band-gap of 1.34 eV at room temperature and it can interfere in the measurement of the absorption in two ways. For one thing, inter-subband transition may be submerged in free-carrier absorption background. This can be avoided by using semi-insulating substrate, which has very small free-carrier density. For another, the inter-band absorption of a GaInAs/AlAsSb quantum well may overlap with absorption originating from InP direct gap. As is indicated in figure 2.3, inter-band absorption energy of a 5 ML GaInAs/AlAsSb quantum well is already very close to the band-gap of InP. To better resolve the inter-band absorption spectra near band-gap of InP, we used a reference scheme to subtract the absorption contributed by the substrate. Each multi-pass waveguide is actually further divided into two equal parts by its width. One piece stays intact and it becomes a ‘test’ sample for absorption measurement. The other ‘reference’ sample goes through wet-etching process so that its epitaxial layers are removed. Eventually the part of absorption contributed by InP substrate can be removed by comparing the absorbance spectra of ‘test’ and ‘reference’ samples.

Reduction of barrier layer thickness

Another way to increase inter-subband absorbance is to integrate more quantum wells in the structure. Since all materials in $\text{Ga}_{0.47}\text{In}_{0.53}\text{As}/\text{AlAs}_{0.56}\text{Sb}_{0.44}$ quantum wells are lattice-matched to InP substrate, there’s no major difficulty in achieving arbitrary thick structure. But it would be beneficial to reduce the thickness of AlAsSb layer in order to reduce growth time of samples with high stacking-number.

Here we try to determine the minimum AlAsSb layer thickness that is required to sufficiently separate two GaInAs quantum wells. We examine two $\text{Ga}_{0.47}\text{In}_{0.53}\text{As}$ quantum wells separated by a variable central barrier using $k \cdot p$ calculations. Figure 2.9a shows the band schema of such a structure, and the energy split between the first two eigenstates $E_2 - E_1$ was used as an indication of the strength of the coupling between the two quantum wells. Figure 2.9b displays the energy split as a function of central barrier thickness. E_1 and E_2 are mostly degenerated until the barrier thickness is reduced to about 5 nm. Thus 6 nm thick AlAsSb layers is considered sufficient and this value is used in future GaInAs/AlAsSb samples prepared for inter-subband absorption studies.

Near-infrared Absorption of $\text{Ga}_{0.47}\text{In}_{0.53}\text{As}/\text{AlAs}_{0.56}\text{Sb}_{0.44}$

Samples preparation

Three $\text{Ga}_{0.47}\text{In}_{0.53}\text{As}/\text{AlAs}_{0.56}\text{Sb}_{0.44}$ multiple quantum well samples were prepared for the study of inter-subband absorption. Figure 2.10a illustrates the structure of these samples, in which the AlAsSb layer is now reduced to 6 nm. The three samples have

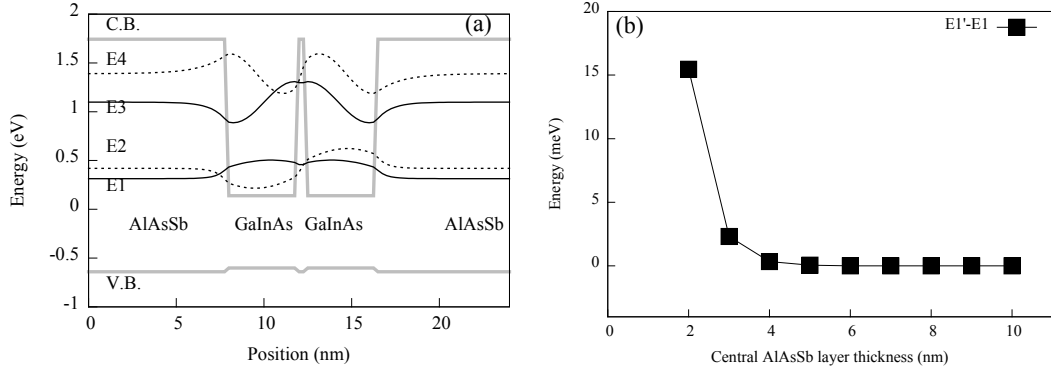


Figure 2.9: The determination of minimal $\text{AlAs}_{0.56}\text{Sb}_{0.44}$ barrier layer thickness. (a) In coupled-double quantum wells, the split between originally degenerated levels E_2 - E_1 serves as an indication of coupling between them. (b) Calculated energy split as a function of central barrier thickness.

5 ML (S1346), 7 ML (S1329) or 9 ML (S1347) of GaInAs in each period of their quantum wells. These samples were grown under the same conditions as previous ones except that semi-insulating InP:Fe substrate was used to suppress free-carrier absorption in the substrate, and the GaInAs layers are intentionally doped with Si ($5 \times 10^{18} \text{ cm}^{-3}$) to populate conduction-band ground-level. To increase the inter-subband absorbance, the number of quantum well contained in these samples is now increased to 100. To protect surface AlAsSb layer from oxidation, all the samples were finished with a 5 nm thick $\text{GaAs}_{0.51}\text{Sb}_{0.49}$ layer.

After the growth, the samples are made into multiple reflection waveguides: they are first thinned to a thickness of about 280 μm and cleaved into slabs around 8 mm wide and 16 mm long. After a series of mechanical polishing and chemical etching, they are shaped into multi-reflection ‘test’ samples and their accompanying ‘reference’ samples without epitaxial layer. The photo in figure A.2 (page 119) gives an example of such a multi-reflection waveguide.

Room PL characteristics

To assure that the optical qualities of these samples were not degraded during mechanical processing, PL experiments were performed on the epitaxial side of these multiple-reflection waveguides. Figure 2.10b shows room temperature PL spectra of these samples. They are actually as strong as unprocessed samples and this assures the integrity of epitaxial layer. The PL spectra of sample S1329 (7ML) has a line-width of 84 meV, which is actually not broader than that of a similar 10 periods sample (S1309). This suggests the no extra inhomogeneity has developed during the stacking of large number of quantum wells. The PL peak of sample S1346 (5 ML) is centered at 950 nm, which is not far from the absorption edge of InP substrate as well as the limit of our spectrometer.

Although InP:Fe semi-insulation substrate do not appear in these PL spectra, it may interfere with the measurement of inter-band absorption in this sample.

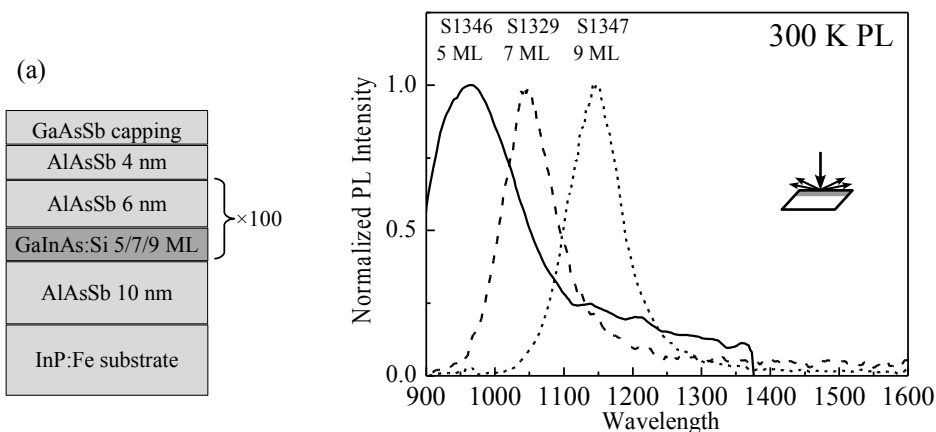


Figure 2.10: (a) Structure of samples S1346, S1329 and S1347. (b) Their room-temperature PL spectra.

Absorbance measurements

To help identify all source of absorption, absorbance measurement is first examined under surface-normal incidence. Figure 2.11 shows the absorption spectra of sample S1329 (7ML) and S1047 (9ML) along with their room temperature PL peak energies marked by arrows. In these absorption spectra, each sample has a steep absorption edge. Since the absorption edges red-shifts in the same manner as their PL energies, they are attributed to inter-band absorption of GaInAs/AlAsSb quantum wells. The PL energies are separated with absorption edges by a moderate Stokes-shift of about 50 meV, which could be either a result of inhomogeneity or band-filling (Moss-Burstein shift)⁵. The absorption spectrum of a third sample S1346 (5 ML) is not shown here, for its inter-band absorption cannot be discriminated from the absorption coming from InP substrate.

Following that, the absorption in these samples was measured under multiple-reflection configuration. Figure 2.12 gives the absorption spectra of sample S1329 (7 ML) and S1347 (9 ML) measured under the two orthogonal polarizations as an example. Under TE-polarization, the absorption spectrum is composed of several steps. Each of these steps could correspond to an absorption mechanism; the step located at 1150 nm is identified as the inter-band absorption edge in GaInAs/AlAsSb quantum wells, and the step around 1600-1700 nm is attributed to the GaAs_{0.51}Sb_{0.49} protection layer, which has a band-gap of about 0.72 eV (1.7 μm) at room temperature. The TE-polarized absorbance

⁵At 300 K, n -doping level of $5 \times 10^{18} \text{ cm}^{-3}$ in a 7 ML-thick Ga_{0.47}In_{0.53}As quantum well would result in a Fermi-level 13 meV above E_1 . $E_1 - E_C = 0.47 \text{ eV}$ is taken from tight-binding calculations.

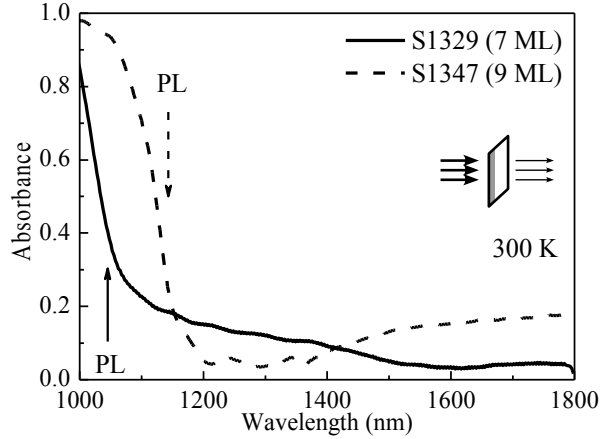


Figure 2.11: Absorption spectra of sample S1329 (7 ML) and S1347 (9 ML). Incident light enters the sample by its epitaxial face. The arrows indicate the wavelength where room temperature PL peaks appear.

steps down to almost zero when the wavelength is reaching reaches 2000 nm. In contrast, from 1400 nm until the detector limit of 2150 nm, the TM-polarized absorption almost does not decrease. The gap between the TM and TE absorbance thus signifies the polarization dependent (anisotropic) absorbance of GaInAs/AlAsSb quantum well.

The polarization dependent absorbance is better revealed when absorption data is presented as $\log_{10}(T_{TE}/T_{TM})$. Figure 2.13 presents the anisotropic absorption of samples S1347 (9 ML) along with the other two samples under study S1346 (5 ML) and S1329 (7 ML). Although only a fraction of a full absorption peak is observed for sample S1047 (9 ML) within the limit of detector, complete anisotropy peaks are observed for the other two samples. According to the discussion on equation (2.5) (page 28), the peaks in $\log_{10}(T_{TE}/T_{TM})$ plot thus represent the E_1 - E_2 inter-subband absorption in GaInAs/AlAsSb quantum wells. Based on the magnitude of these anisotropy spectra and the dimensions of the samples, we determine the inter-subband absorption coefficient $\alpha_{E_1-E_2}$ to be roughly in the order of $1 \times 10^3 \text{ cm}^{-1}$.

For the 7 ML quantum well sample S1329, its inter-subband absorption peak appear at 1900 nm (0.65 eV) and it has a line-width of about 300 nm (120 meV). Its inter-subband transition energy is lower than the 0.8 eV theoretical value expected for a perfect $\text{Ga}_{0.47}\text{In}_{0.53}\text{As}/\text{AlAs}_{0.56}\text{Sb}_{0.44}$ quantum well. By further decreasing the quantum well thickness to 5 ML (S1346), its inter-subband transition energy is almost the same as the 7 ML sample (S1329), rather than continuing shifting towards shorter wavelength as is predicted by tight-binding calculations. At the same time its 600 nm (210 meV) line-width is even larger than the 7 ML sample (S1329). It seems the inter-subband wavelength saturates at 1900 nm although quantum well as thin as 5 ML is used.

Similar inter-subband wavelength limit has been separately reported by Neogi *et al.* and Cristea *et al.*, and in their experiment the inter-subband absorption also saturates

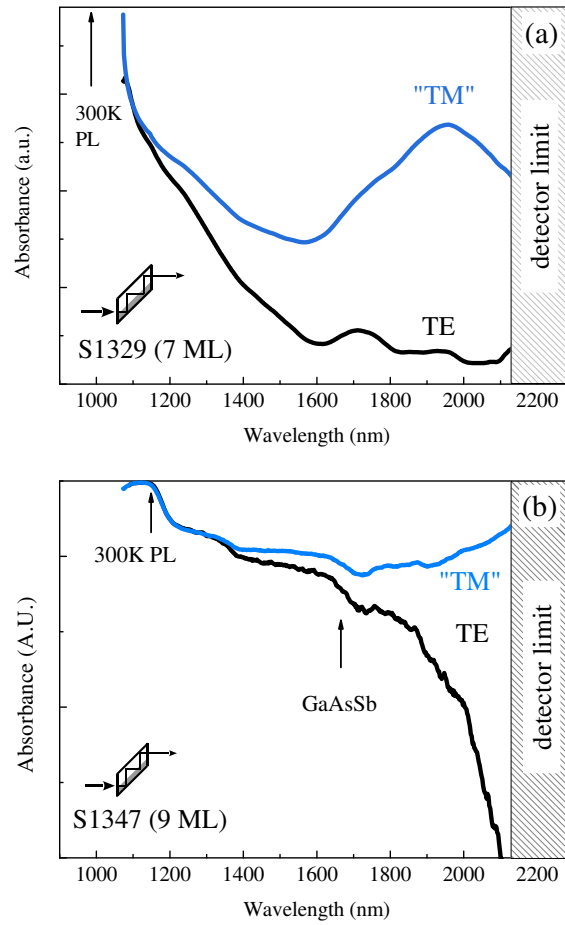


Figure 2.12: Absorption spectra of samples S1329 (7 ML) and S1347 (9 ML) under different polarizations. The incident-light enters the multi-reflection samples by their facets.

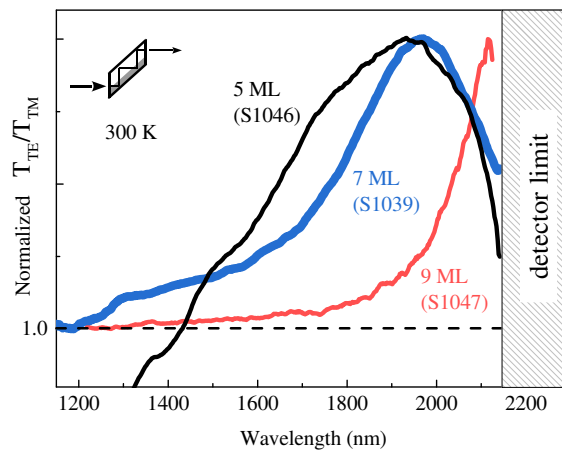


Figure 2.13: Anisotropic absorption spectra of GaInAs/AlAsSb quantum well samples S1346 (5 ML), S1329 (7 ML) and S1347 (9 ML). The anisotropy data is calculated using T_{TM}/T_{TE} and then normalized to enable comparison between the spectra.

at about 1900 nm [19, 30]. In figure 2.14, the current inter-subband absorption data are compared with both tight-binding calculations and experimental data of Neogi *et al.* . The two sets of experimental results are very close to each other, which indicate the results of Neogi *et al.* are reproducible, and in turn validate the experimental results we have. Last but not least, unlike Ga_{0.47}In_{0.53}As, AlAs_{0.56}Sb_{0.44} lattice-matched to InP substrate is a less known material for many respects [31, 32]. Even reported values of band-alignment between (Ga)InAs and AlAsSb differ [4, 19, 33, 34], which can significantly influence energy simulations.

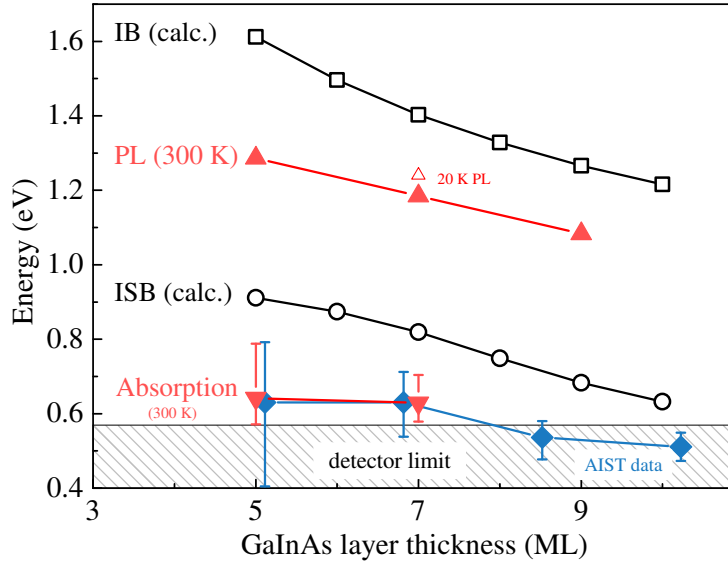


Figure 2.14: Experimental PL and inter-subband absorption peak energies compared to tight-binding calculated transition energies. “AIST” data are extract from [19]

Summary

In this section, we have presented a study of inter-subband properties of Ga_{0.47}In_{0.53}As/-AlAs_{0.56}Sb_{0.44} quantum wells. After a series of structure optimization, epitaxial growth, waveguide fabrication, PL characterization and inter-subband absorption measurements of these samples, we have obtained near-infrared inter-subband absorption for the first time in FOTON laboratory.

However, the goal of inter-subband transition in 1.55 μm -band was still not achieved. By reducing the GaInAs quantum-well thickness from 7 ML to 5 ML, the inter-subband energy saturates at 1.9 μm rather than moving towards 1.55 μm . Through calculations, Cristea *et al.* has suggested that further reducing GaInAs quantum well thickness won't help achieve shorter inter-subband absorption wavelength [30]. For an even thinner GaInAs/AlAsSb quantum well, its perturbed interface region could be comparable or even larger than its quantum-well thickness. All kind of imperfection coherent to GaInAs-

/AlAsSb interface could have played its role in degrading its inter-subband properties. In the coming sections, we will present an investigation on GaInAs/AlAsSb interfaces using microscopic studies.

2.4 The effects of surface terminations

There are two types of interfaces in a GaInAs/AlAsSb quantum well: the AlAsSb-on-GaInAs (upper) interface and GaInAs-on-AlAsSb (lower) interface. The different cation/anion transitions at the interfaces deserve to be treated differently and surface terminations should be adapted to the chemical nature of each interface.

In this section, we will first present a study on how different surface termination methods can influence the structural and optical properties of GaInAs/AlAsSb quantum wells. Following that, microscopic structure and composition analysis were performed to enable a closer look at the various interfaces in these samples, which may give more insight into all kinds of imperfections that have prevented us from achieving 1.55 μm inter-subband absorption.

Table 2.2 lists three sets of surface terminations that will be examined in this section. Surface terminations for AlAsSb-on-GaInAs (upper) interfaces are numbered in letters ($\langle\text{A}\rangle$, $\langle\text{B}\rangle$, $\langle\text{C}\rangle$) while those for GaInAs-on-AlAsSb (upper) interfaces are referenced by numbers ($\langle\text{1}\rangle$, $\langle\text{2}\rangle$, $\langle\text{3}\rangle$). These surface terminations could have different effects on the growth surface. For example, long-time growth interruption under As_2 flux is *supposed* to help purge Sb floating on the surface, while long-time Sb_2 growth interruption can make the growth surface Sb-rich in order to prevent the first layers of AlAsSb being Sb-poor[25].

A series of three $\text{Ga}_{0.47}\text{In}_{0.53}\text{As}/\text{AlAs}_{0.56}\text{Sb}_{0.44}$ samples were prepared to incorporate each of the three sets of surface terminations. The growth conditions were the same as before and these structures were elaborated in three consecutive growth runs to ensure consistent growth conditions. Conductive *n*-type InP substrates were used but the epitaxial structures were not intentionally doped. Figure 2.15 gives a representative illustration of their structure. Each sample only contains 10 periods of quantum-well and GaInAs layers as thick as 7 nm (24 ML) were used to better separate the two types of interfaces.

Macroscopic studies

XRD structural characterizations were performed on these samples to assess the effect of surface termination on their structural properties. Symmetric ω - 2θ scans were recorded in the vicinity of InP (004) reflection. Both period thickness and average lattice mismatch of the epitaxial structure are extracted from such measurements and their results are listed in table 2.3. The quantum-well period thicknesses of the three samples are very

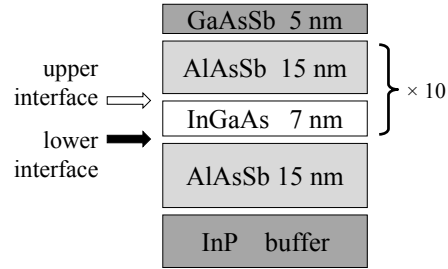


Figure 2.15: Sample structure used in the study of surface termination methods. The different types of interfaces are indicated by arrows.

Table 2.2: The various surface termination methods along with their numbering scheme that is used throughout section 2.4 and section 2.5.

Sample	S726 S831	S727 S830	S728 S829
Upper interface AlAsSb-on-GaInAs	$\langle A \rangle$ (As + Sb) 5 s	$\langle B \rangle$ As 5 s then (As + Sb) 5 s	$\langle C \rangle$ As 5 s then Sb 20 s
Lower interface GaInAs-on-AlAsSb	$\langle 1 \rangle$ As 5 s	$\langle 2 \rangle$ Sb 20 s then As 5s	$\langle 3 \rangle$ As 25 s

close to each other within an error margin of 1%, but the average lattice-mismatches in these samples are significantly different.

Samples S829 has the largest compressive misfit strain (0.40%) among the three samples, which means it has largest average lattice constant. Compared to samples S831 which has a mismatch of 0.24%, the long-time Sb₂ growth interruption used in AlAsSb-on-GaInAs interface treatment $\langle C \rangle$ in S829 seems to be responsible for increased average lattice constant, and difference between S829 and S831 is equivalent to converting 4 ML of AlAs_{0.56}Sb_{0.44} into pure AlSb or to incorporate large amount of Sb in Ga_{0.47}In_{0.53}As layer within each period of such quantum well. Similarly, S830 has a mismatch (0.38%) comparable to samples S829 (0.40%), and the long-time Sb₂ grow-interruption used in GaInAs-on-AlAsSb interface $\langle 2 \rangle$ seems to have similar effect.

The XRD study thus indicates the surface terminations can have significant influence on the structural properties of GaInAs/AlAsSb quantum wells, and they can be used to tune the strain in quantum well structures [35].

Table 2.3: Structural parameters and PL characteristics of samples S829-S831

Sample	Period (nm)	Mismatch (%)	PL Energy (eV)	Integrated Intensity. (A.U.)	Line width (meV)
S829	20.2	0.40	0.849	2049	55
S830	20.3	0.38	0.855	2190	44
S831	20.1	0.24	0.855	4098	59

The optical properties of these samples were then characterized by low temperature PL. The PL spectra were recorded from 15 K up to 160 K and 532 nm laser was used as excitation source with a maximum excitation density of about 4 kW/cm². Various PL characteristics of these samples are listed in table 2.3.

Figure 2.16 displays 15 K PL spectra of the three samples. A first remark on these spectra would be that samples (S831) has significant higher PL yields that the other two samples. This samples actually has shortest growth interruption time among the three samples and this seem to suggest that long-time growth interruption may not be good to optical properties of GaInAs/AlAsSb quantum wells. Although MBE growth proceeds under high-vacuum conditions, various impurities like O₂ are still present in the growth chamber and they are difficult to get rid of. Some of these impurities have high affinity to III-V materials and they tend to can incorporated in epitaxy thin film during long-time growth interruption. These impurities may form deep levels in the materials and they become efficient non-radiative recombination centers; little amount of their incorporation would significantly enhance non-radiative recombination rate and thus the PL yield is reduced.

At the same time, these PL energy peaks are located at almost the same energy with

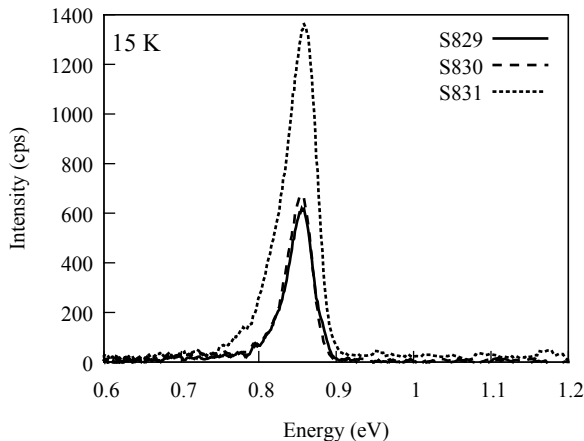


Figure 2.16: Low temperature PL spectra of samples S829, S830 and S831. The sample temperature was 15 K and excitation power was 4 kW/cm^2

only 5 mV difference between samples S829 and the other two. This indicates that the PL energy is actually independent of the surface termination methods used. Specifically for sample S830, where long-time Sb_2 growth interruption were used at GaInAs-on-AlAsSb interface $\langle 2 \rangle$, no extra amount of Sb should have been incorporated around the GaInAs-on-AlAsSb than the other two samples; if so, the PL energy of sample S830 would red-shift by much larger than 5 meV with regard to the other two samples.

We thus have compared the three types of surface terminations at the interface between GaInAs and AlAsSb using PL and XRD. The results of these macroscopic characterizations show that surface terminations have significant influence on both the structural properties and optical quality of GaInAs/AlAsSb quantum wells. Additionally, they remind us that PL emission intensity can be influenced by unattended factors so that it should not be used as the only criteria to evaluate the quality of a sample. To understand how the surface terminations are correlated to the microscopic structures near the GaInAs/AlAsSb interface, we have launched a series of microscopic investigations on all the interfaces we have studied.

Microscopic study by cross-sectional scanning tunneling microscopy

Another sample S844 was prepared specially for X-STM observations. It contains various GaInAs/AlAsSb pairs so that it integrates all the previously studied six surface termination methods. The structure of this samples is illustrated in figure 2.17 . The substrate as well as epitaxially grown InP layers in these samples are doped with Si so as to make the whole structure conductive. By integrating all the interfaces into one sample, all the layers and interfaces can be measured with the same STM tip and tunneling conditions. In order to isolate all the interfaces from each other, the GaInAs/-AlAsSb pairs are separated by 10 nm-thick InP spacer layers. The surface terminations

are numbered in the same way as previously studied samples (table 2.2, page 36). The STM cross-section was obtained by cleaving along one of its $\{110\}$ natural cleavage surface under ultra-high vacuum conditions. STM images were then taken under constant current mode with negative samples bias. The X-STM observations and analyses were performed by Samuel Mauger at Technische Universiteit Eindhoven.

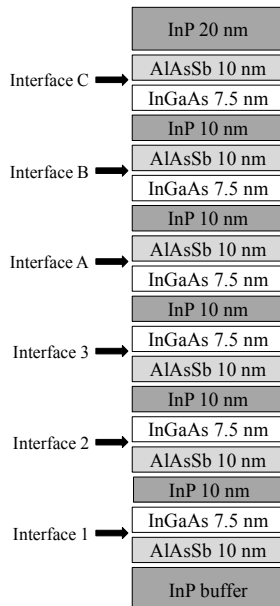


Figure 2.17: Sample structure of S844

Figure 2.18a displays a large-scale atomically resolved X-STM images of samples S844. Under the large negative bias used, filled states of group-V elements are probed and the image contrast mainly reflects topology (surface height) information of the cleaved surface. Each spot in the image represents an anion atom, and antimony atoms appear brighter than arsenic ones. Due to the vertical rearrangement of surface atoms (buckling), only every other $\bar{1}10$ atomic row is probed along $[001]$ direction so that the distance between these atomic row is actually 2 ML. Figure 2.18a presents a large-scale X-STM image showing various alloy layers and interfaces of samples S844, while figure 2.18b and figure 2.18c give a closer look at the GaInAs-on-AlAsSb interface $\langle B \rangle$ and AlAsSb-on-GaInAs interfaces $\langle A \rangle$.

In order to quantitatively assess the unintentional incorporation of Sb into subsequent GaInAs layer, the distribution of antimony atoms is extracted from the STM image. Since Sb atoms appear at higher altitude in STM image than arsenic atoms, they can be identified on the STM image using automated procedures based on topology information. Figure 2.19 illustrates how Sb-counting is performed in practice. At first, the original STM image in 2.19a is flattened by a spatial filter to remove the slow varying components in its topology information. Then Sb-atom identification algorithm is performed on the processed image 2.19b, to identify Sb atoms by their altitudes and each * symbol in

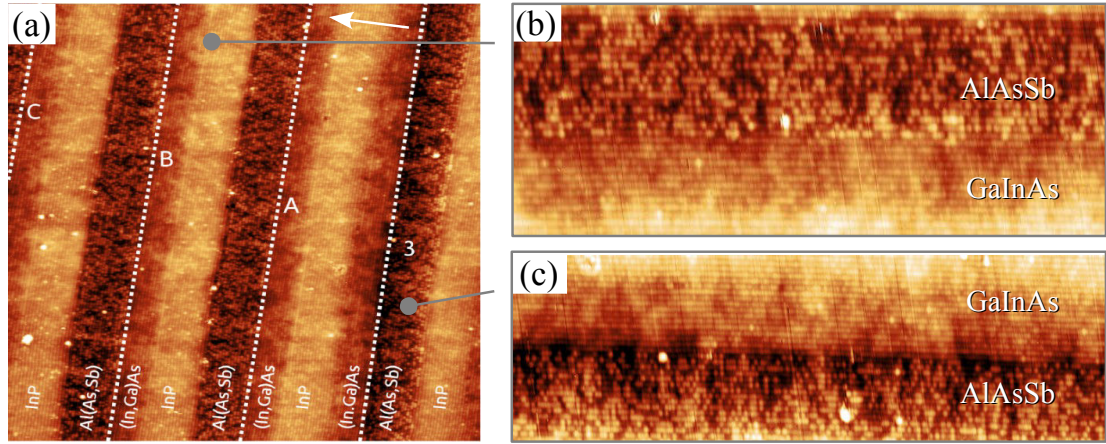


Figure 2.18: Large scale X-STM images of sample S844 (a). The image was taken under constant current mode with negative samples bias ($V_{\text{sample}} = -3.5$ V, $I = 40$ pA). The scanned area is $100 \times 100 \text{nm}^2$. The various interfaces are annotated in place and the growth direction is indicated by the white arrow. (b) magnified view of AlAsSb-on-GaInAs interface $\langle B \rangle$. (c) magnified view near GaInAs-on-AlAsSb interface $\langle 3 \rangle$.

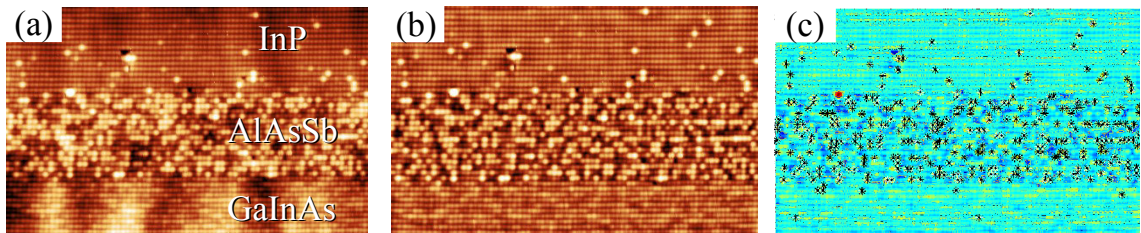


Figure 2.19: Sb-atom identification process in near InP-on-AlAsSb interface. (a) Original image (b) after high-pass spatial filter (c) detected Sb-atoms.

figure 2.19c represents a detected Sb atom. The central band where most Sb atoms are concentrated correspond to the AlAsSb layer, while the Sb atoms lying out of this region thus correspond to unintentionally incorporated Sb atoms segregated from AlAsSb layers. Various useful statistics can be extract from such measurements.

Figure 2.20b presents the Sb-distributions obtained near the GaInAs-on-AlAsSb interfaces of samples S844. Each data point in these figures represents the portion of Sb atoms detected in a $[\bar{1}10]$ atomic row over a length of 50 nm. The measured Sb content in AlAs_{0.56}Sb_{0.44} layer is around 0.23–0.45, which is sometimes lower than its nominal Sb-content of 0.44 in AlAsSb layer. This is due to the fact the automated procedure failed to recognize every Sb atoms, especially when they are closely packed. At the two ends, these profiles presented in figure 2.20 show sharp Sb-concentration onset but they also have segregation tails as long as 8 ML.

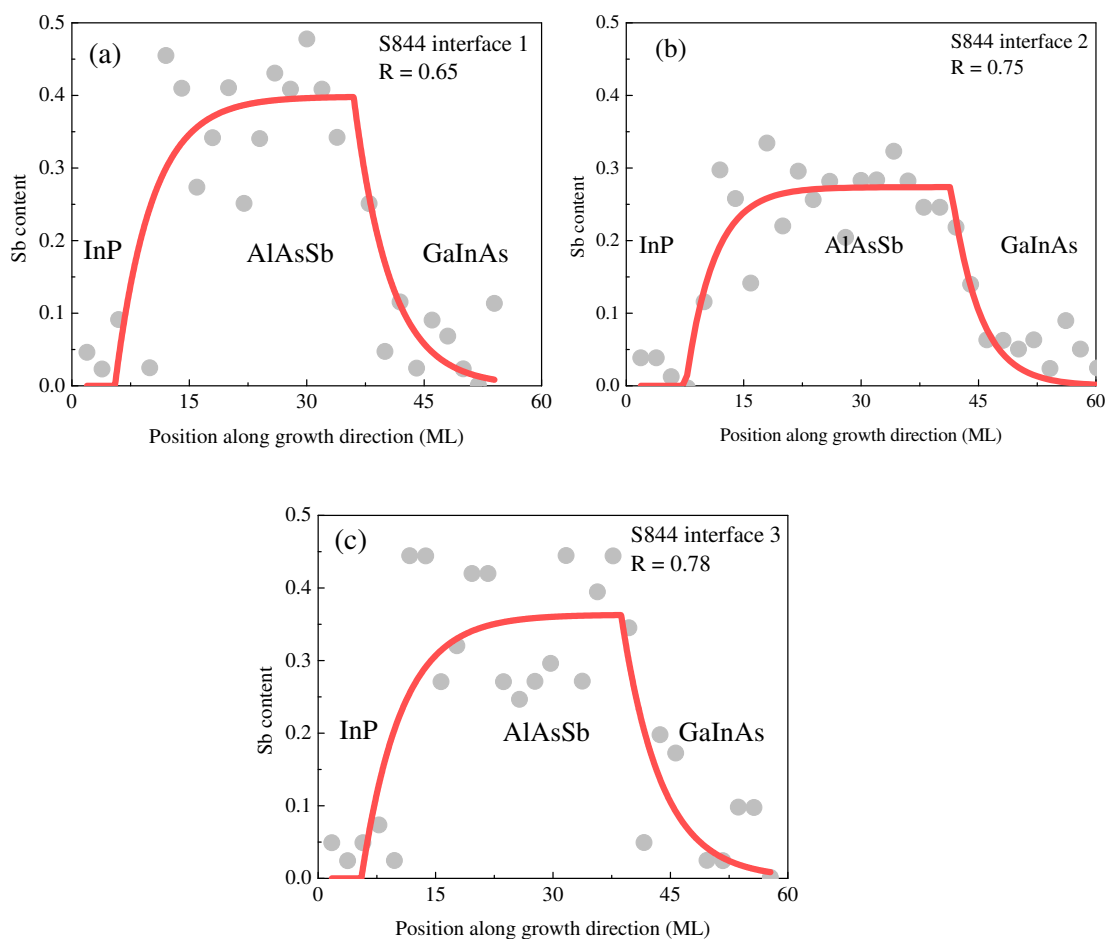


Figure 2.20: Segregation profiles of Sb near three GaInAs-on-AlAsSb interfaces of samples S844.

To have further meaningful quantitative description of the segregation of Sb, these

Table 2.4: Fitting parameter for Sb segregation profiles in sample S844. The error bars represent the standard deviation of the fitting results.

Interface		x_0	R	$S \pm dS$
GaInAs-on-AlAsSb	⟨1⟩	0.40 ± 0.03	0.65 ± 0.10	0.9 ± 0.4
	⟨2⟩	0.27 ± 0.01	0.76 ± 0.05	1.0 ± 0.3
	⟨3⟩	0.36 ± 0.03	0.68 ± 0.10	0.9 ± 0.4

distribution are fit to the segregation model of Muraki [36] :

$$\begin{cases} x_n = x_0(1 - R^n) & N \geq n \geq 1 \\ x_n = x_0(1 - R^N)R^{n-N} & n > N \end{cases} \quad (2.6)$$

This model has been successfully applied to the segregation profile of indium, and the obtained segregation parameter R provides good quantitative description of indium's segregation behavior [36]. Applied to the current study, n is the index of atomic layers and the two ends of AlAsSb layer marked by $n = 0$ and $n = N$. This model assumes that during the formation of each AlAsSb layer, R fraction of Sb atoms segregates into subsequent layers for every one portion of Sb deposited. The Sb concentration x_n reaches a stable concentration of x_0 in the inner part of AlAsSb layer, but 'transient' Sb distribution present at the onset ($n = 0$) and at the termination ($n = N$) of the AlAsSb layer. As is demonstrated in figure 2.20, Muraki's model describes well the Sb distribution near AlAsSb layer.

The similar procedure is repeated near three the GaInAs-on-AlAsSb interfaces and their fitting parameters are given in table 2.4 by expressing the credibility of such fitting in error margins. Segregation coefficients R ranging from 0.65 to 0.76 are found for the different surface termination method used. To have an idea of Sb-incorporation in GaInAs layer, the total number of segregated Sb atoms can be summed by :

$$S = \sum_N^{\infty} x_0(1 - R^N)R^{n-N} \approx -x_0/\ln R \quad (2.7)$$

The integration results are listed in table 2.4, and the S values are found to be about one full mono-layer for all the three interfaces under study in spite of the different surface termination methods used. Interface ⟨2⟩ has experienced 20 s Sb₂ growth interruption followed by another 5 s under As₂, but it has only get 0.1 ML more Sb incorporated in the GaInAs layer following it than in the case of interface ⟨3⟩, which has experienced as long as 25 s Sb-purging As₂ growth-interruption. The consistent Sb-incorporation levels among the three samples thus agree well with the previous PL observation, where PL energy is independent of surface termination method (table 2.3, page 37). However, to understand why surface terminations had little effect on unintentional Sb-incorporation, we need to know how Sb exists on the growth surface.

A Sb-rich surface reconstruction is usually considered to be terminated with an incomplete layer of Sb-Sb dimers atop another complete Sb-mono-layer [37]. Steinshnider *et al.* have pointed out that only the surface Sb-Sb dimers are responsible for the Sb-atoms segregated into subsequent layers[38]. For the current study, this suggests that the amount of segregated Sb atoms is actually determined by the surface reconstruction of AlAsSb surface and the three surface termination methods used in this study may had little or no effect on the amount of excess Sb on AlAsSb surface.

On the other hand, the 1 ML of Sb unintentionally incorporated into a 7 ML-thick GaInAs layer would result into a Sb-concentration of 14%. This may account for the large energy difference existing between calculated inter-band energy and experimental PL energies in section 2.2 (figure 2.6, page 25).

Summary

In this section, we have studied the influence of different surface terminations on the properties of GaInAs/AlAsSb quantum wells using both macroscopic and microscopic analyses. The different surface termination methods have shown significant influence on both the structural and optical properties of GaInAs/AlAsSb quantum wells. The microscopic studies reveal that as much as 1 ML Sb can be unintentionally incorporated into subsequent GaInAs layer, which could explains the 200 meV difference between experimental PL energy observed in GaInAs/AlAsSb quantum wells and those calculated theoretical values; it could also contribute to non-achievement of 1.55 μm inter-subband transition.

2.5 The impact of digital alloy growth

The GaInAs / AlAsSb coupled double quantum well structure illustrated in 2.9a is used by many research groups to achieve 1.55 μm inter-subband devices. Such structure has many adjustable parameters like the composition of GaInAs quantum well and the thickness AlAsSb central barrier. These parameters enable high degree of band-engineering but they also jeopardize the controllability and reproducibility of epitaxial growth . Different GaInAs compositions require additional set of calibrated indium and gallium fluxes. At the same time, group-III elements fluxes cannot be rapidly changed during MBE growth, so that it is difficult incorporate GaInAs of different composition in one structure.

“Digital alloy” is an MBE technique than enable the growth of $\text{Ga}_x\text{In}_{1-x}\text{As}$ of arbitrary composition x with the same set of molecular beam flux as $\text{Ga}_{0.47}\text{In}_{0.53}\text{As}$. It mimics random GaInAs alloy by depositing GaAs and InAs alternately rather than simultaneously, and the composition of ‘digital’ GaInAs is determined by the ratio between GaAs and InAs deposited in each deposition cycle. Digital alloy as a method has

been practiced in the growth of several ternary alloys like AlGaAs, GaInAs and AlAsSb. These digital alloys were found to have comparable or even superior properties than their “conventional” counterparts[39].

In order to evaluate the impact of integrating digital alloy in the growth of GaInAs/AlAsSb structure, a set of three GaInAs/AlAsSb multiple quantum wells samples, S728 S727 and S726, were grown using digital $\text{Ga}_{0.47}\text{In}_{0.53}\text{As}$ alloy layers. In each digital alloy deposition cycle, 0.43 ML GaAs and 0.48 ML InAs were deposited to match the composition of $\text{Ga}_{0.47}\text{In}_{0.53}\text{As}$. To ensure flux stability, 5 s grow interruption is performed between each GaAs/InAs flux switching, and the overall growth rate is equivalent to 0.07 ML/s, which is lower than the 0.2 ML/s conventional growth rate of $\text{Ga}_{0.47}\text{In}_{0.53}\text{As}$. Except for the growth method of GaInAs layer, these three samples are made to have identical structure and surface termination methods in previously studied samples S829, S830 and S831. These samples are first characterized by XRD for structural parameters and low temperature PL for optical properties.

Macroscopic properties

PL spectra of these samples were actually measured within the same test-run as previous samples S829–S831, and their PL spectra were recorded from 15 K to about 160 K. Figure 2.21a gives a comparison of all the PL spectra while the various PL characteristics are summarized in table 2.5. PL spectra of digital-alloy samples present more than 10 times higher PL yield than conventional samples. Figure 2.21b further shows a comparison of PL quenching speed of digital-alloy sample S728 and its counterpart S829 (conventional). With increasing temperature, the PL signals of digital alloy attenuate slower than a conventional sample, so that it has a higher barrier for the thermal activation of non-radiative processes. These characteristics of digital alloy samples suggest the use of digital GaInAs has significantly improved the optical properties of GaInAs/AlAsSb quantum wells. Nevertheless, the various interface treatments have noticeable influence on the PL emission energy of digital alloys, which is not observed in conventional samples. This is evidenced by a PL energies difference of 25 meV existing between samples S726 and S728, while the PL peaks of conventional samples are separated by no more than 5 meV.

Structural properties of these digital-alloy samples were then analyzed by XRD . The ω - 2θ scan of sample S727 is compared with its conventional counterpart S830 in figure 2.22. The digital-alloy sample S727 displays only a few satellite peaks; in contrast, its conventional counterpart sample S830 shows much more satellite peaks and even Pendellösung fringes were resolve. The abundant satellites peaks and fringes in conventional samples suggest that the periodicity in the sample is good and all the layers within the samples are relatively flat and macroscopically homogeneous; this agrees with the previous X-STM observations. For digital-alloy samples, the absence of these

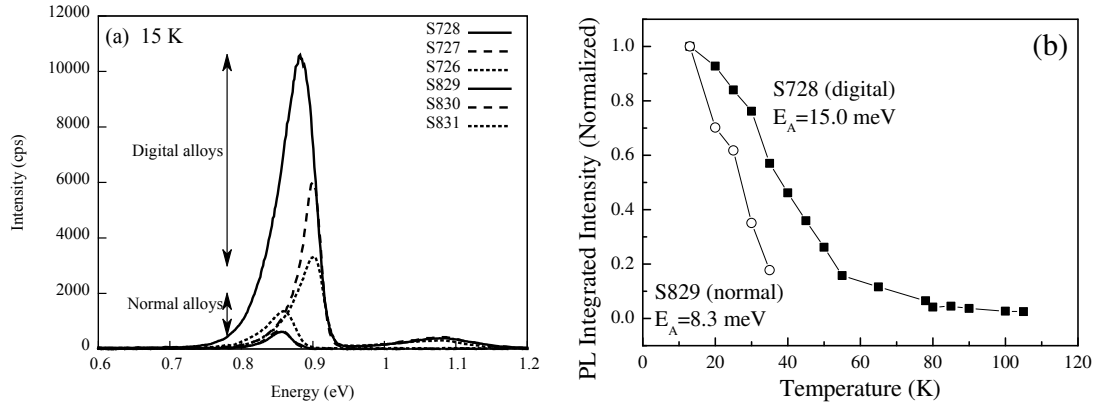


Figure 2.21: (a) Low temperature PL spectra of samples for digital-alloy samples and conventional samples. (b) PL quenching in S728 and S829.

Table 2.5: Characteristics extracted from PL measurements

	Sample	Peak Energy (eV)	Integrated Intensity (A.U.)	Line width (meV)	E_a (meV)
Digital	S728	0.873	17273	65	15.0
	S727	0.893	17193	46	10.5
	S726	0.898	8069	54	-
Conventional	S829	0.849	2049	55	8.3
	S830	0.855	2190	44	7.9
	S831	0.855	4098	59	11.6

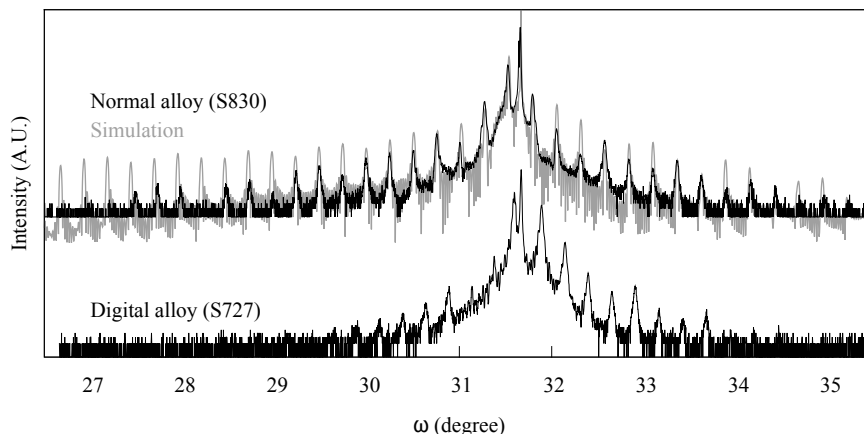


Figure 2.22: XRD $\omega-2\theta$ pattern of sample S831 and its digital-alloy counterpart S727. It is superposed onto simulated XRD pattern in gray.

features could be a result of inhomogeneity layers and rough interfaces.

So far, the PL studies indicate the use of digital GaInAs enhances the optical properties of GaInAs/AlAsSb quantum wells, but the XRD structural analyses suggest digital alloy samples have degraded structural properties as compared to conventional alloys. In order to understand such contradicting interpretations, we again turn to X-STM for a microscopic observation of digital GaInAs.

Microscopic study

An additional sample S680 was grown and prepared for X-STM studies of digital alloy GaInAs. This sample has exactly the same structure as the previously studied S844 (figure 2.17, page 39) except that digital GaInAs layers were used instead of conventional ones. The sample is cleaved by one of its $\{110\}$ natural cleavage plane, and STM measurements were performed under constant current mode with negative sample bias. Under such conditions, filled states in group-V element are probed. Figure 2.23a shows a large-scale X-STM image of sample S680, while figure 2.23b features a magnified view of a GaInAs layer and an AlAsSb one.

Noticeable alternating contrast appears in the GaInAs layer. To better reveal this feature, averaged height profile were extracted along $[\bar{1}10]$ direction in digital GaInAs layers. Figure 2.24 presents the height profile within digital GaInAs layer number $\langle 1 \rangle$, along with its counterpart extracted from the previously studied conventional GaInAs samples. Fluctuations exist in both GaInAs layers, but the amplitude of fluctuation is much larger in digital alloy than in conventional alloy.

Under the negative sample bias, only filled state of arsenic atoms are probed in GaInAs layer. Although large negative samples bias was employed to suppress electronic contrast, compositional inhomogeneity can still be reflected in STM image: since GaAs

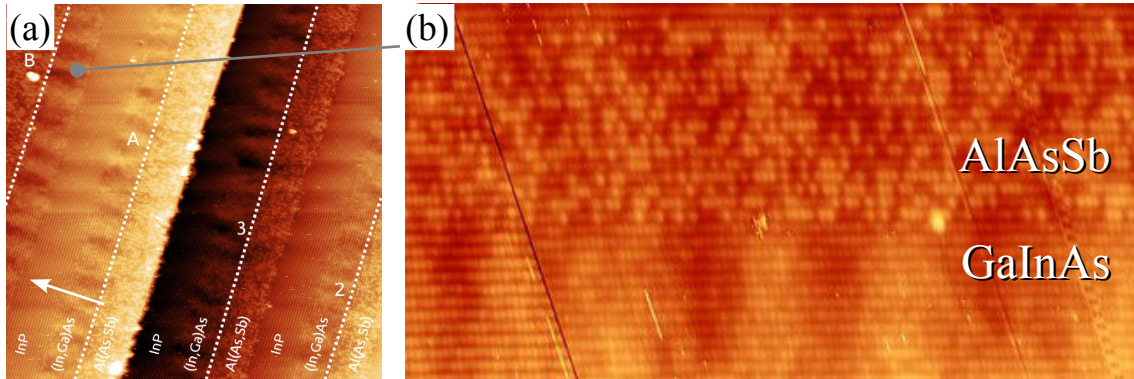


Figure 2.23: (a) Large X-STM image of digital alloy sample S680. The growth direction is marked by white arrow. (b) magnified view near the AlAsSb-on-GaInAs interface. The image was taken under constant current-mode with negative samples bias ($V_{\text{sample}} = -3.0$ V, $I = 43$ pA). The scanned area is $100 \times 100 \text{nm}^2$.

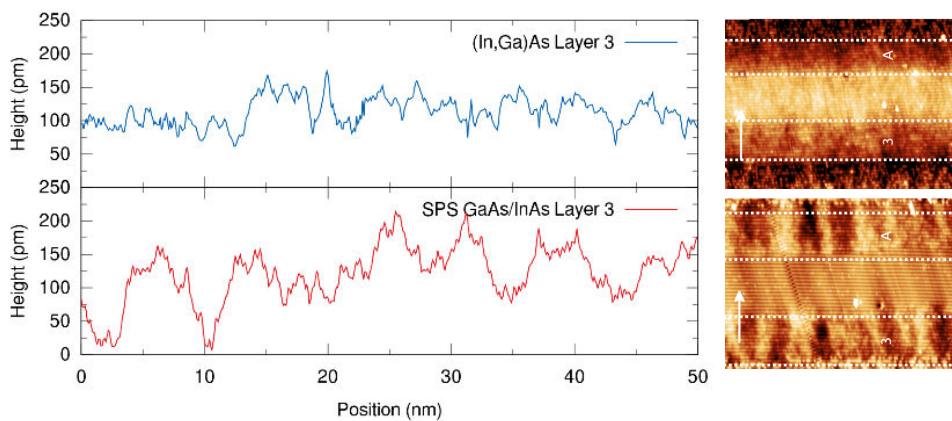


Figure 2.24: Comparison of STM surface profiles along [110] direction, taken in (upper) digital GaInAs alloy layer 3 in samples S680 and (lower) conventional GaInAs layer 3 in samples S844. SPS, short period super-lattice is synonym of digital alloy.

has a larger band-gap than InAs, the STM tip is descended to keep the tunneling current constant when passing Ga rich-zones in GaInAs layer, while it is pulled up when passing through InAs rich zones. Therefore, the columns with brighter contrast in figure 2.23b are identified as indium-rich zone while darker ones are gallium-rich. Therefore, the alternating contrast in digital GaInAs layers actually reflects lateral modulation of its composition.

Such lateral composition modulation has been observed in the growth of quite a few semiconductor alloys, including conventional GaInAsP layer [40, 41] and digital GaInAs alloy when GaAs/InAs deposition cycle is long [42]. Lateral composition modulation is propagated along with strain field but surface segregation could have played an important role [43].

The observed lateral composition modulation in digital GaInAs alloy helps reconcile the disagreeing XRD and PL results. In one hand, the inhomogeneity in GaInAs layer degrades X-ray diffracting conditions so that fewer satellite peaks appear in XRD pattern. In the other, Indium-rich zones in the digital GaInAs layer effectively provide better confinement for both electrons and holes due to its smaller band-gap. Carriers inside such zones are less likely to participate in non-radiative processes that are related to disorders and defects near the GaInAs/AlAsSb interface. Therefore, the carriers in digital GaInAs layer with severe composition modulation are less sensitive to temperature change than a conventional homogeneous GaInAs layer. Meanwhile, the surface origin of lateral composition modulation and surface processes also explains why PL emission energies of digital alloy are sensitive to interface treatment method used.

Summary

In this section, we have examined the possibility of using digital GaInAs alloy in GaInAs/AlAsSb quantum wells. It was intended to increase flexibility in the growth of future complex GaInAs/AlAsSb structures. However, the introduction of this technique has incurred large inhomogeneity within the GaInAs layer. For the specific example of GaInAs/AlAsSb quantum well, such inhomogeneity can be improve the PL yields and it risks to be mistaken for an improvement in overall optical quality.

Conclusion

Through the studies presented in this chapter, we have achieved near-infrared inter-subband absorption at $1.9\ \mu\text{m}$ using InP-based $\text{Ga}_{0.47}\text{In}_{0.53}\text{As}/\text{AlAs}_{0.56}\text{Sb}_{0.44}$ quantum wells from scratch. Since the goal of inter-subband transition in $1.55\ \mu\text{m}$ telecommunication band was not achieved, we have launched a series microscopic investigation to understand the underlying mechanisms that prevent us from reaching this goal. The microscopic observations of GaInAs/AlAsSb quantum wells have found the interior of

the alloys is not perfectly homogeneous. More importantly, these studies have shown that as much as 1 ML Sb can be unintentionally incorporated into subsequently GaInAs layer.

Since many of the imperfections are inherent to the complexity of GaInAs/AlAsSb structure and they are difficult to eliminate using normal growth techniques. Nevertheless, it has been reported that the use indium-rich $\text{Ga}_{0.8}\text{In}_{0.2}\text{As}$ layer in GaInAs/AlAsSb structure can effectively shorten the inter-subband transition wavelength to about $1.73\ \mu\text{m}$ [30]. In the next chapter, we attempted to advance this idea by using pure InAs and to fabricate strained InAs/AlAsSb quantum wells.

References

- [1] B. F. Levine, “Quantum-well infrared photodetectors”, *Journal of Applied Physics* **74**, R1–R81 (1993).
- [2] J. P. Commin et al., “High peak power 3.3 and 3.5 μm InGaAs/AlAs(Sb) quantum cascade lasers operating up to 400 K”, *Applied Physics Letters* **97**, pages (2010).
- [3] R. Akimoto et al., “All-optical switch based on intersubband transition in quantum wells”, in *IEEE/LEOS winter topicals meeting series, 2009* (2009), pp. 154–155.
- [4] I. Vurgaftman et al., “Band parameters for III–V compound semiconductors and their alloys”, *Journal of Applied Physics* **89**, 5815 (2001).
- [5] C. Manz et al., “Epitaxial growth of GaInAs/AlGaAsSb quantum cascade lasers”, *Journal of Crystal Growth* **301–302**, 893–896 (2007).
- [6] P. K. Basu, *Theory of optical processes in semiconductors: bulk and microstructures* (Oxford University Press, 2003), 470 pp.
- [7] T. Akiyama et al., “1.55 μm picosecond all-optical switching by using intersubband absorption in InGaAs-AlAs-AlAsSb coupled quantum wells”, *IEEE Photonics Technology Letters* **14**, 495–497 (2002).
- [8] S.-i. Gozu et al., “Cross phase modulation efficiency enhancement in $\text{In}_{0.8}\text{Ga}_{0.2}\text{As} / \text{Al}_{0.5}\text{Ga}_{0.5}\text{As} / \text{AlAs}_{0.56}\text{Sb}_{0.44}$ coupled double quantum wells by tailoring interband transition wavelength”, *Applied Physics Express* **2**, 042201 (2009).
- [9] G. W. Cong et al., “Experimental and theoretical study of cross-phase modulation in InGaAs/AlAsSb coupled double quantum wells with a AlGaAs coupling barrier”, *Physical Review B* **80**, 035306 (2009).
- [10] R. Akimoto et al., “Ultrafast intersubband optical switching in II–VI-based quantum well for optical fiber communications”, *physica status solidi (b)* **243**, 805–812 (2006).
- [11] J. Song et al., “Growth and characterization of ZnSe/BeTe superlattices”, *Journal of Crystal Growth* **229**, 104–108 (2001).
- [12] B. S. Li et al., “ZnSe interlayer effects on properties of (CdS/ZnSe)/BeTe superlattices grown by molecular beam epitaxy”, *Journal of Applied Physics* **99**, 044912 (2006).
- [13] A. Waag et al., “Molecular-beam epitaxy of beryllium-chalcogenide-based thin films and quantum-well structures”, *Journal of Applied Physics* **80**, 792–796 (1996).
- [14] F. Guillot, “Développement de nanostructures à base de semiconducteurs III-Nitrides pour l’optoélectronique infrarouge”, PhD thesis (Université Joseph-Fourier - Grenoble I, 2007).
- [15] M. Tchernycheva et al., “Systematic experimental and theoretical investigation of intersubband absorption in GaN/AlN quantum wells”, *Physical Review B* **73**, 125347 (2006).

-
- [16] T. Mozume et al., “1.45 μm intersubband absorption in InGaAs/AlAsSb grown by molecular beam epitaxy”, *Japanese Journal of Applied Physics* **38**, 1286–1289 (1999).
- [17] C. V.-B. Tribuzy et al., “Femtosecond pump-probe spectroscopy of intersubband relaxation dynamics in narrow InGaAs/AlAsSb quantum well structures”, *Applied Physics Letters* **89**, 171104 (2006).
- [18] T. Akiyama et al., “Very low saturation intensity and ultrafast response of 1.5 μm intersubband absorption in n-doped InGaAs/AlAsSb MQW”, *ELECTRONICS LETTERS* **36**, 362–364 (2000).
- [19] A. Neogi et al., “Absorption saturation of near-infrared intersubband transition in lattice-matched InGaAs/AlAsSb quantum wells”, *Physica E: Low-dimensional Systems and Nanostructures* **7**, 183–186 (2000).
- [20] A. Neogi et al., “Temperature-insensitive intersubband-transitions in InGaAs/AlAsSb multiple quantum well designed for optical communication wavelength*”, *Japanese Journal of Applied Physics* **40**, L558–L560 (2001).
- [21] T. Akiyama et al., “Nonlinearity and recovery time of 1.55 μm intersubband absorption in InGaAs-AlAs-AlAsSb coupled quantum wells”, *Electronics Letters* **37**, 129–130 (2001).
- [22] A. V. Gopal et al., “Understanding the ultra-low intersubband saturation intensity in InGaAs-AlAsSb quantum wells”, *Quantum Electronics, IEEE Journal of* **39**, 299–305 (2003).
- [23] R. Akimoto et al., “All-optical demultiplexing of 160–10 gbit/s signals with mach-zehnder interferometric switch utilizing intersubband transition in InGaAs/AlAs/AlAsSb quantum well”, *Applied Physics Letters* **91**, 221115 (2007).
- [24] J.-M. Jancu et al., “Empirical spds* tight-binding calculation for cubic semiconductors: general method and material parameters”, *Physical Review B* **57**, 6493–6507 (1998).
- [25] R. Kaspi and K. R. Evans, “Sb-surface segregation and the control of compositional abruptness at the GaAsSb/GaAs interface”, *Journal of Crystal Growth* **175–176, Part 2**, 838–843 (1997).
- [26] T. Mozume et al., “Dopant-induced interface disorder in InGaAs/AlAsSb heterostructures lattice matched to InP grown by molecular beam epitaxy”, *Journal of Crystal Growth* **227–228**, 577–581 (2001).
- [27] T. Mozume and N. Georgiev, “Interface control of InGaAs/AlAsSb heterostructures”, *Thin Solid Films* **380**, 249–251 (2000).
- [28] P. Chavarkar et al., “Effect of sb composition on lateral oxidation rates in AlAs[sub 1-x]Sb[sub x]”, *Applied Physics Letters* **76**, 1291 (2000).
- [29] F. H. Julien and P. Boucaud, “Optical intersubband absorption and emission in quantum structures”, in *Optical spectroscopy of low dimensional semiconductors* (Sept. 1996).
- [30] P. Cristea et al., “Tuning the intersubband absorption in strained AlAsSb/InGaAs quantum wells towards the telecommunications wavelength range”, *Journal of Applied Physics* **100**, 116104 (2006).
- [31] T. Mozume et al., “Optical functions of AlAsSb characterized by spectroscopic ellipsometry”, *physica status solidi (a)* **205**, 872–875 (2008).
- [32] J. Y. Kim et al., “Optical properties of AlAs_xSb_{1-x} alloys determined by in situ ellipsometry”, *Applied Physics Letters* **103**, pages (2013).
- [33] S. Bhargava et al., “Staggered to straddling band lineups in InAs/Al(As, sb)”, *Applied Physics Letters* **74**, 1135 (1999).
- [34] Y.-H. Li et al., “Revised ab initio natural band offsets of all group IV, II-VI, and III-V semiconductors”, *Applied Physics Letters* **94**, 212109 (2009).
- [35] S.-i. Gozu et al., “Strain control of InGaAs/AlAs/AlAsSb quantum wells by interface termination method between AlAs and AlAsSb”, *Journal of Crystal Growth* **323**, Proceedings of the 16th International Conference on Molecular Beam Epitaxy (ICMBE), 39–41 (2011).
- [36] K. Muraki et al., “Surface segregation of in atoms during molecular beam epitaxy and its influence on the energy levels in InGaAs/GaAs quantum wells”, *Applied Physics Letters* **61**, 557 (1992).

- [37] U. Resch-Esser et al., “Microscopic structure of GaSb(001) $c(2\times 6)$ surfaces prepared by sb decapping of MBE-grown samples”, *Physical Review B* **55**, 15401–15404 (1997).
- [38] J. Steinshnider et al., “Origin of antimony segregation in GaInSb/InAs strained-layer superlattices”, *Physical Review Letters* **85**, 4562–4565 (2000).
- [39] R. Kaspi and G. P. Donati, “Digital alloy growth in mixed As/Sb heterostructures”, *Journal of Crystal Growth* **251**, 515–520 (2003).
- [40] T. Okada et al., “Growth of strained InGaAs layers on InP substrates”, *Journal of Applied Physics* **81**, 2185–2196 (1997).
- [41] A. Ponchet et al., “Lateral modulations in zero-net-strained GaInAsP multilayers grown by gas source molecular-beam epitaxy”, *Journal of Applied Physics* **74**, 3778–3782 (1993).
- [42] D. Follstaedt et al., “Spontaneous lateral composition modulation in InAlAs and InGaAs short-period superlattices”, *Physica E: Low-dimensional Systems and Nanostructures* **2**, 325–329 (1998).
- [43] C. Dorin and J. M. Millunchick, “Lateral composition modulation in AlAs/InAs and GaAs/InAs short period superlattices structures: the role of surface segregation”, *Journal of Applied Physics* **91**, 237–244 (2002).

Chapter 3

Sb-mediated Growth of InAs/AlAs_{0.56}Sb_{0.44} Strained Quantum Wells for Inter-subband Applications

InAs/AlAs_{0.56}Sb_{0.44} quantum well has an even deeper electron confinement potential than Ga_{0.47}In_{0.53}As/AlAs_{0.56}Sb_{0.44} and this makes it yet another candidate material system for InP-based near-infrared inter-subband applications. Besides, since Ga is completely removed from the structure, this new material system does not suffer from various inhomogeneity problem that is associated with Ga_{0.47}In_{0.53}As/AlAs_{0.56}Sb_{0.44}. However, the growth of strained InAs layer on InP substrate is a challenge for conventional MBE growth, because InAs deposition on InP substrate switches to three-dimensional growth mode upon a very small quantity of InAs deposition.

In section 3.2, we will demonstrate that the use of Sb-mediated growth makes the deposition of pseudomorphic InAs layer possible. Section 3.3 further finds out the limit of the pseudomorphic InAs layer. To prepare such quantum well for inter-subband absorption studies, strain compensation is applied to enable stacking of multiple InAs/AlAs_{0.56}Sb_{0.44} quantum wells in section 3.4. Finally, a preliminary study on inter-subband absorption in these structures will be presented in section 3.5.

3.1 Properties of InAs/AlAs_{0.56}Sb_{0.44} strained quantum well

In figure 3.1, the band-alignment of InAs/AlAs_{0.56}Sb_{0.44} quantum well is compared with that of a Ga_{0.47}In_{0.53}As/AlAs_{0.56}Sb_{0.44} quantum well. The InAs/AlAsSb quantum well has a even larger conduction-band offset $\Delta E_C^\Gamma \approx 1.7$ eV than the previously studied GaInAs/AlAsSb. For two quantum wells with the same well-layer thickness, an InAs-/AlAsSb quantum well has lower inter-band energy than a GaInAs/AlAsSb quantum well, because pure InAs has a much smaller band gap (0.35 eV 300 eV eV, 300 K) than Ga_{0.47}In_{0.53}As (0.74 eV). However, since InAs has smaller electron effective mass than Ga_{0.47}In_{0.53}As, its conduction-band subbands are more widely separated than its GaInAs/AlAsSb counterpart, thus it has can achieve higher inter-subband transition energy and larger oscillator strength.

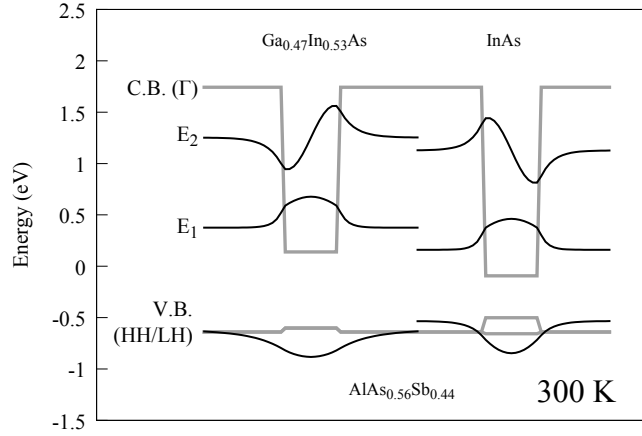


Figure 3.1: A comparison of conduction band subbands in Ga_{0.47}In_{0.53}As/AlAs_{0.56}Sb_{0.44} and InAs/AlAs_{0.56}Sb_{0.44} quantum wells. The subband’s wave-functions are superposed on their energy levels. They were simulated using $k \cdot p$ calculations.

In order to determine the structural parameters of InAs/AlAs_{0.56}Sb_{0.44} quantum for 1.55 μm inter-subband transition, the transition energies in InAs/AlAsSb quantum wells were simulated by empirical tight-binding calculations. The InAs/AlAsSb quantum wells were modeled by super cells containing 34 ML AlAs_{0.56}Sb_{0.44} and InAs ranging from 5 to 10 ML while the wave-functions are expanded using an extended $spds^*$ -basis. This specific method is developed by Jean-Marc Jancu[1], and the simulations were performed by Soline Richard.

Figure 3.2 plots simulated transition energies as a function of InAs layer thickness. To obtain inter-subband transition at 0.8 eV (1.55 μm), it is necessary to achieve a 7 ML-thick (2.1 nm) InAs layer in InAs/AlAsSb quantum well. This thickness is actually small for a usual quantum well. However, it is larger than the Matthews-Blakeslee’s critical thickness of plastic relaxation for InAs grown on InP substrate (presented in figure 1.5, page 14). Direct InAs deposition on InP substrate usually leads to the formation of

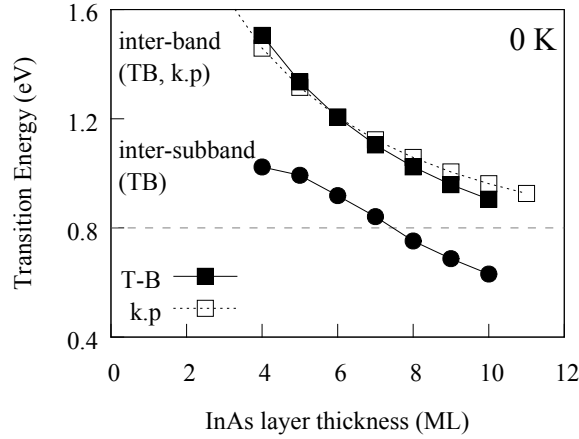


Figure 3.2: Transition energies of InAs/AlAs_{0.56}Sb_{0.44} simulated by tight-binding calculations; the inter-band transition energy are given in filled squares while inter-subband transition energies in filled circles. For comparison, inter-band transition energies calculated using $k \cdot p$ method are given in empty squares.

coherent three-dimensional nanostructures like quantum dots once the deposition is over a critical thickness of 2 ML (section 4.1, page 76). The growth of coherent islands is not without limit and continuing deposition after the formation of coherent islands will lead to the formation of large relaxed islands (ripening), and eventually coarse thin film with high density of defects formed by coalescence of these islands [2, p. 295].

Fortunately, there exists various growth technique that can delay the formation of islands. At the same time, by introducing certain impurities known as surfactant during the growth of strained material, it is possible to maintain layer-by-layer growth-mode and delay the formation of three-dimensional islands. In the following sections, we will demonstrate how Sb as a surfactant can assist the growth of pseudomorphic InAs layer on InP (001) substrate.

3.2 Sb-mediated Growth of InAs on InP substrate

Surfactant Effect of Sb

Surfactant-mediated growth of strained epitaxial layer has great technological importance and the maintenance of two-dimensional growth mode was its earliest and most intended use. The surfactant effect as a growth technique and existing theories on its mechanisms have been thoroughly reviewed by many authors [2–4]. It is known that Sb atoms tend to segregate and they virtually “float” on the growth front [5]. By forming specific dimer arrangement, it effectively reduces surface energy of growth surface and modifies the energetics and kinetics of underlying growth process.

Harmand *et al.* have demonstrated that the use of Sb-mediated growth can enable the growth of strained Ga_{0.8}In_{0.2}As layer on GaAs substrate [6]. The FOTON labora-

tory has also achieved “thick” InAs layer on InP substrate using Sb-mediated growth [7]. Figure 3.3 shows a strained InAs/Ga_{0.47}In_{0.53}As quantum well grown on InP (001) substrate using Sb-surfactant-mediated growth. Although the InAs-layer is as thick as 10 ML, it has flat interface and no defect like dislocation is observed around it. Further TEM analyses indicate that only Sb-incorporation in the InAs layer was very low.

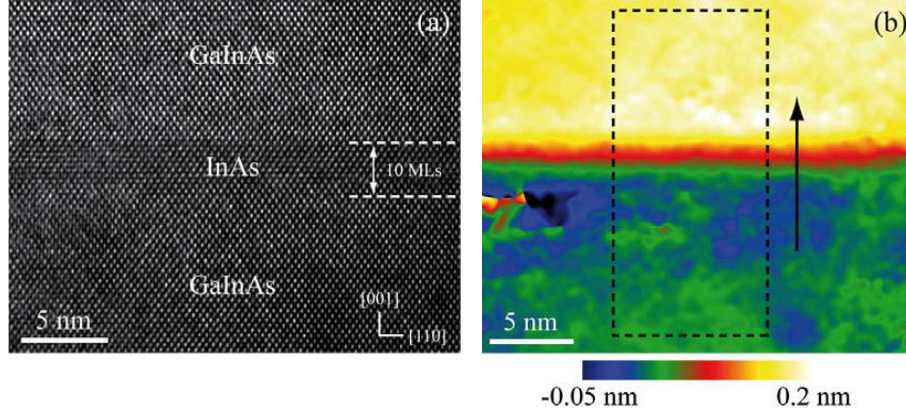


Figure 3.3: 10 ML thick InAs layer grown by Sb-mediated growth on InP (001) substrate. (a) Its high-resolution TEM observation. (b) Accompanying map of U_z displacement in which the InAs layer is more easily distinguished. In the map, variation of color signifies spatial variation of lattice-constant (a_z), but there is no direct correspondence between a color and a specific lattice-constant (material). [7].

In the growth of InAs/AlAsSb quantum well, the surface of AlAsSb buffer layer itself is Sb-rich, and the accumulation of Sb on the growth surface could be sufficient to help maintain two-dimensional growth mode of InAs layers. To verify this, we thus have examined InAs/AlAsSb growth carried out both with and without the supply of Sb during the deposition of InAs.

Effectiveness of surfactant effect

Two InAs/AlAs_{0.56}Sb_{0.44} single quantum well structures, S845.1 and S846.1 were grown with or without Sb co-deposition during the growth of InAs layer. Figure 3.4a illustrates the structure of these samples. They were grown on InP (001) substrate under the same conditions as previous Ga_{0.47}In_{0.53}As/AlAs_{0.56}Sb_{0.44} samples. After the deoxidation of InP substrate, a InP buffer layer was grown to ensure the flatness of growth surface. However, due to a technique problem related to arsenic valved-cell, a significant portion of arsenic is incorporated into their In(As)P buffer layer. Therefore, the thickness of InP buffer layer was kept as low as possible. After that a 15 nm-thick AlAs_{0.56}Sb_{0.44} layer was grown. The 10 ML thick InAs layer were grown either with Sb₂ co-deposition for S845.1, or without it for S846.1 by blocking the Sb₂ flux using its shutter plate. Following that, a 20 s growth interruption was performed under combined As₂ and Sb₂ fluxes, before the InAs(Sb) deposition was covered by another 15 nm-thick AlAs_{0.56}Sb_{0.44}

layer. Finally, the top surface of the structure is finished by a final 5 nm GaAs_{0.51}Sb_{0.49} protecting layer. Additionally, to enable comparisons of surfactant effect on different substrate orientations, two extra InAs/AlAs_{0.56}Sb_{0.44} samples S845.2 and S846.2 were grown on InP (113)B substrates accompanying their “.1” counterparts grown on (001) substrates¹.

The InAs/AlAs_{0.56}Sb_{0.44} made on InP (001) substrate were characterized by XRD to assess the crystalline quality of their InAs layer, and their $\omega-2\theta$ scans in the vicinity of InP (004) reflection are displayed in figure 3.4b. Three diffraction peaks are identified for each sample: (004) reflection of InP substrate at 31.6°, the diffraction peak of In(As)P buffer layer at about 31° and InAs-related peak between 29°-30°. The InAs peaks are very weak and at the same time very broad. This is expected for the small volume and small thickness of InAs layers. The diffraction from sample S845.1 (+Sb) is much stronger than that of S846.1 and even Pendellösung fringes are resolved, which assures relatively good interface flatness throughout the structure. In order to acquire strain state of InAs layer within these samples, XRD pattern of a nominal 10 ML InAs/AlAs_{0.56}Sb_{0.44} quantum-well (with In(As)P buffer layer) was simulated by assuming that the InAs layer be completely strained. The simulation result is overlaid with XRD patterns in figure 3.4b, and its agreement with S845.1’s XRD pattern suggests that InAs layer grown with Sb co-deposition is fully strained. In contrast, the InAs peak from sample S846.1 is even weaker and it has shifted towards higher angles, which suggests that plastic relaxation could have probably occurred within InAs layer when no Sb is supplied *during* the deposition of InAs.

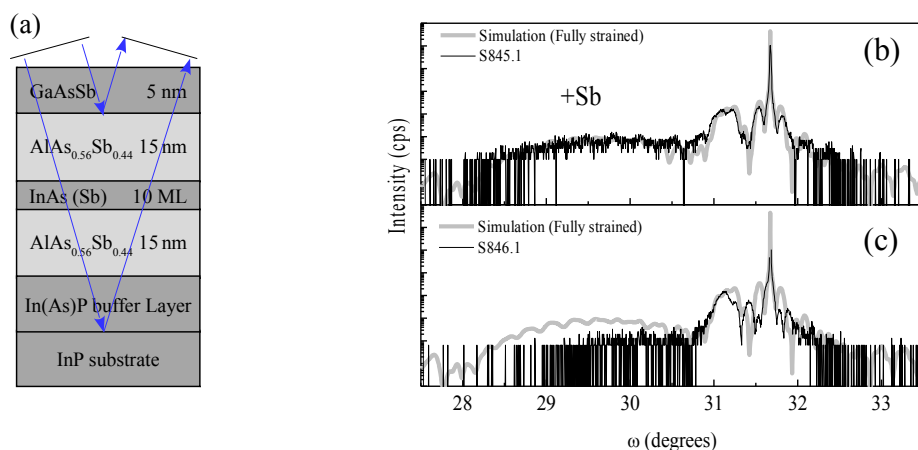


Figure 3.4: Structural properties of InAs/AlAs_{0.56}Sb_{0.44} single quantum well samples S845.1 and S846.1. (a) A schematic illustration of their structure (b) XRD $\omega-2\theta$ scans near InP (004) reflection.

Low temperature PL measurements were performed on these samples to assess their

¹In case two samples are prepared in the same growth run, the one made on (001) substrate is given “.1” suffix, while its counterpart made on high-index substrate like (113)B is named “.2”.

optical properties. The PL spectra were recorded under 12 K and they are grouped by the substrate orientations in figure 3.5. The PL energy of samples S845.1 is located at about 0.81 eV, while PL of other samples are both red-shifted and broadened. Since these samples contain almost the same materials, two factors may be responsible for the observed PL energy shift: different level of Sb-incorporation into InAs layer, and the formation of very rough InAs layer. The hypothesis of Sb-incorporation can be dismissed, because if it is true, samples S845.1 should have contained more Sb than S846.1 so that the PL energy of samples S845.1 would be lower than that of samples S846.1, which conflicts with the experimental observations. Therefore, the very rough InAs interfaces and even the formation of InAs islands are responsible for the observed PL shifts: when Sb is supplied with InAs deposition, the surfactant effect of Sb ensures the planarity of InAs deposition so that InAs quantum well is achieved. When Sb is insufficient, rough interface or three-dimensional growth mode accompanies strain relaxation of InAs, which actually agree with the XRD observations. The same strain relaxation could have occurred for S845.2 made on (113)B substrate, even though Sb is supplied during InAs deposition. This result seems to indicate that the Sb's surfactant effect behaves differently on (113)B oriented substrate, and this phenomena will be investigated in chapter 4 (starting from page 75).

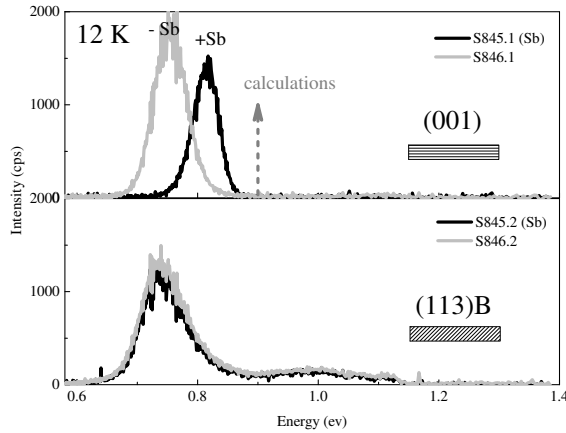


Figure 3.5: Low temperature PL of samples S845.1/2 and S846.1/2

3.3 Sb-mediated growth of pseudomorphic InAs/AlAs_{0.56}-Sb_{0.44} single quantum well

In the previous section, we have demonstrated that it is possible to obtain relatively flat InAs strained layer on InP substrate as thick as 10 ML by using Sb-mediated growth. However, there's still no guarantee that the strained layer is free of defects that is commonly seen for strained epitaxial layer. More importantly, it is useful to know

the upper limit of strained InAs layer thickness that can be achieved using Sb-mediated growth. In this section, a series of InAs/AlAsSb were prepared for both macroscopic and microscopic characterization of their qualities.

More InAs/AlAsSb single-quantum-well structures were fabricated in the same way and under the same conditions as sample S845.1, except that the amounts of InAs depositions now range from 5 to 13 ML. During the growth, the reflective high energy electron diffraction (RHEED) pattern did not show clear chevron-like feature that is characteristic to the formation of quantum dots. Therefore, XRD measurements were performed at first to obtain the structural information about these single quantum wells.

Determination of the limit of pseudomorphic growth

Figure 3.6a displays XRD $\omega-2\theta$ scans of these samples near the (004) reflection of InP substrate. Abundant Pendellösung fringes were resolved for samples with no more than 8 ML InAs deposition inside, while the fringes gradually fade as InAs quantity increases. It is usually difficult to detect X-ray diffraction from as little as 7 ML material using a laboratory equipped XRD instrument. Actually, these fringes originate from interference between diffraction from different material layers, and their periodicities are reciprocally related to distances between interfaces within the sample structure [8]. For most of the samples, two set of fringes were identified by their different periodicities. The one with larger period corresponds to the thicknesses of one of the AlAsSb barrier layers plus InAs layer, while the fringes with small period correspond to total thickness of epitaxial layer including In(As)P buffer layer². The presence of fringes for samples having no more than 8 ML of InAs deposition suggests that the InAs layers have relatively good crystalline quality, while their gradual disappearance for depositions over 10 ML is a sign of roughened interfaces and strain relaxation could have occurred within these structures.

To determine the relaxation of in-plane lattice constant of these Sb-mediated InAs layers, asymmetric $\omega-2\theta$ scans were performed on these quantum well samples. Unfortunately, due to the low volume of InAs within these samples, asymmetric diffraction was only detected for the 13 ML samples. Figure 3.6b demonstrates its two-dimensional reciprocal space map in the vicinity of InP (224)+ reflection. The q_x and q_z are directions in reciprocal space, which are related to in-plane lattice constants along $\langle 110 \rangle$ directions (a_{\parallel}) and vertical lattice constants (a_{\perp}) along [001] direction, respectively. In the figure, the spot with highest intensity represents InP substrate while the other one below it, elongated along q_z direction corresponds to the diffraction from InAs layer. Actually, a vertical slice through the center of InP peak will obtain cross-section similar to those $\omega-2\theta$ scans in figure 3.6a. The InAs spot is located at lower vertical (q_z) position for its larger vertical lattice constant than that of InP, and its large vertical extension reflects

²The fact the interface of between In(As)P buffer layer and InP substrate is a consequence of unintended As incorporation in InP buffer layer; the In(As)P/InP interface itself is actually flat, as is demonstrated by the TEM image in figure 4.8 (page 83).

3.3. Sb-mediated growth of pseudomorphic InAs/AlAsSb single quantum well

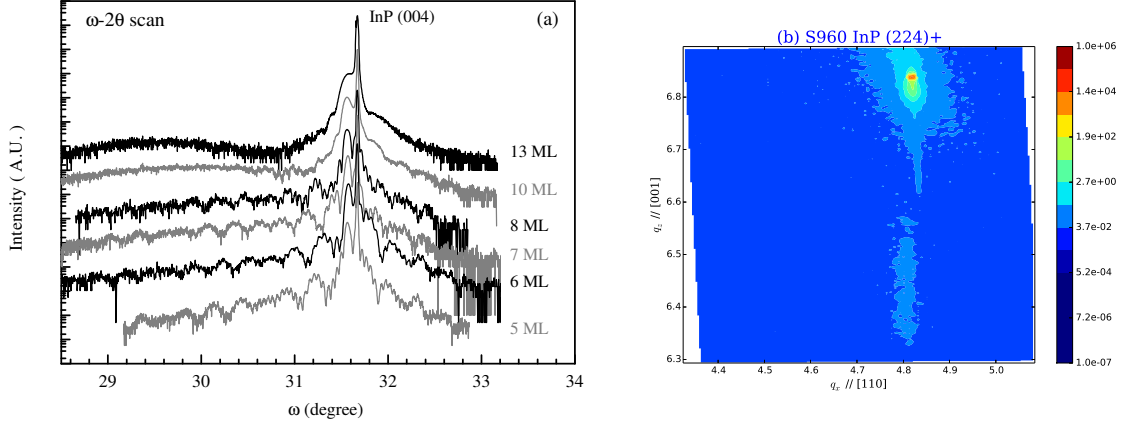


Figure 3.6: XRD analysis of InAs/AlAs_{0.56}Sb_{0.44} quantum wells (a) $\omega-2\theta$ scans with various InAs thicknesses (b) reciprocal space mapping of the 13 ML sample in the vicinity of InP (224)+ reflection

the small thickness along [001] direction. In horizontal directions, the center of InAs spot is nearly aligned with the InP spot but still it is shifted towards smaller q_x by a visible difference. Interpreted in real space, this indicates that the InAs deposition has already plastically relaxed so that its in-plane lattice constant ($a_{\text{InAs},\parallel}$) is slightly larger than that of InP $a_{\text{InP},\parallel} = a_{\text{InP}}$.

To acquire microscopic structural information out of these samples, and also to validate the results of XRD analysis, two InAs/AlAsSb single quantum wells with 7 ML and 12 ML-thick InAs layers were examined by conventional TEM at CEMES (Toulouse), and their dark-field TEM images are displayed in figure 3.7. These images were taken under (002) dark-field imaging conditions so that layers with different composition can be discriminated by their contrasts. Figure 3.7a displays the sample containing 7 ML of InAs deposition. All the layers and interfaces appear flat and homogeneous, with

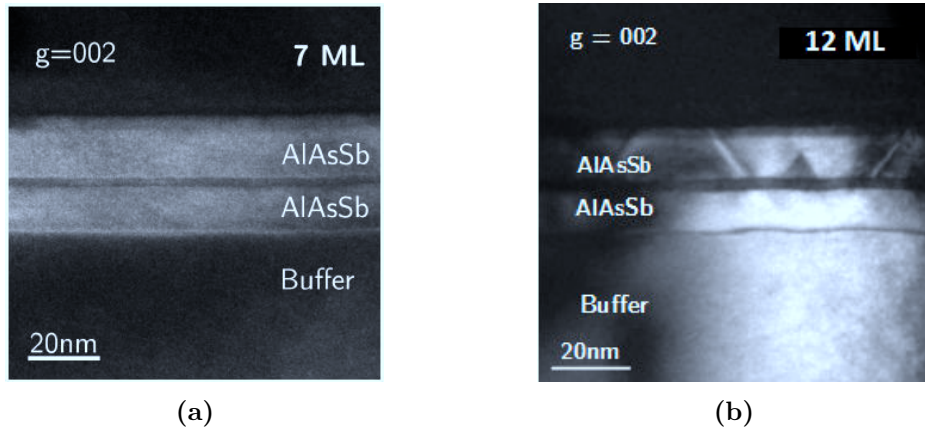


Figure 3.7: TEM (002) dark-field images of the (a) 7 ML sample and (b) 12 ML sample

no trace of island or any other three-dimensional nanostructure. This assures the 7 ML InAs layer intended for 1.55 μm inter-subband application is achieved. On the other side, figure 3.7b shows a 13 ML InAs/AlAsSb quantum well structure. The both interfaces of InAs layer is already undulated and several lines penetrating the upper AlAsSb layer are present. These lines are characteristic to 60° dislocations³ and the emergence of dislocation confirms that plastic relaxation has occurred within the structure. Nevertheless, it's worth noting that the interface between InP buffer layer is already undulated, and such undulation is carried on to InAs layer.

Optical properties of these Sb-mediated samples were then examined using low temperature PL. Figure 3.8b shows their normalized PL spectra while the intensities are separately compared in figure 3.8c. The PL peaks shift towards low energy as the InAs layer thickness is increased, which is expected for their smaller effective gap. With increasing InAs deposition quantity, the PL emission peak intensities increases before the quantum well thickness reaches 8 ML and they decrease afterwards. The increased intensity is expected since there's more InAs in the structures. The diminished PL intensities at large InAs thickness is then probably a result of overall degradation due to plastic relaxation. The PL line width for the 5 ML samples is about 200 meV while the value is smaller for a thicker InAs quantum well. The decreasing slope of inter-band transition energy in figure 3.8a (page 61) indicates that, by adding or removing 1 ML thickness from a thicker quantum well, the associated transition energy change would be much smaller than that for a much thinner quantum well.

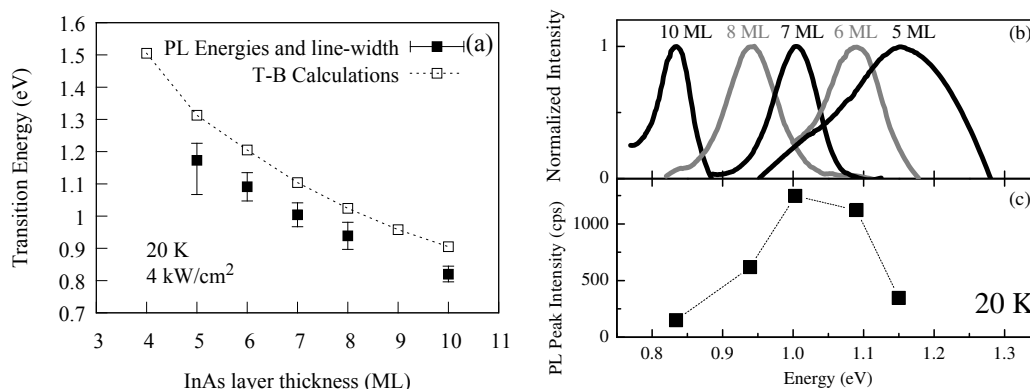


Figure 3.8: Low temperature PL study of InAs/AlAs_{0.56}Sb_{0.44} single quantum wells: (a) PL energies compared with tight-binding calculations previously presented in figure 3.2 Low temperature PL spectra are normalized in (b) to emphasize their the position and width of the emission peaks; their intensities are presented in (c).

In figure 3.8a, these PL energies are compared with the simulated inter-band energies,

³The 60° dislocation in zinc-blende structure is a mixed-type dislocation. Its Burgers vector $|\mathbf{b}| = a_{110}/2$ and it lies along one of the $\langle 110 \rangle$ directions, the dislocation line is parallel to another $\langle 110 \rangle$ direction and its gliding plane is one of the $\{111\}$ planes.

with PL line widths plotted as error margins. The line-widths are in fact no wider than the energy difference brought about by the addition of one ML of InAs in the structure. If the quantum well thickness fluctuation is deemed as the only source of PL line-width broadening, such comparisons indicate the interface roughness within these samples is equivalent to thickness fluctuation of 1 ML. Nevertheless, the experimental PL energies are unanimously ~ 80 meV lower than theoretical values. The incorporation of Sb in InAs layer could again be responsible for such differences, and it's worth studying by quantitative TEM analyses.

Microscopic Study of InAs/AlAsSb Interface

The previously studied 7 ML InAs/AlAsSb TEM sample was examined at a second time by high-resolution TEM to reveal microscopic structure of the InAs layer and its adjacent zones. The analyses was performed by Julien Nicolaï (CEMES, Toulouse) on a FEI TECNAI apparatus with spherical aberration corrections. Figure 3.9a shows a high-resolution TEM image of this sample where atomic resolution was achieved. In this kind of measurement, the composition of observed zone cannot be directly deduced from image contrast. Rather, geometric phase analysis allows quantitative strain analyses using the position of lattice points in high-resolution TEM image. In this technique, a reference lattice constant is first sampled in the AlAs_{0.56}Sb_{0.44} buffer layer. Following that, the out-of-plane lattice constant (a_z) in the region selected by the white rectangle in figure 3.9a is averaged along the in-plane direction and then compared to the reference. Any difference in strain state could reflect difference in composition. Here, the difference of lattice constant is termed as “deformation” using the notation of strain. For instance, figure 3.9b shows an ε_{zz} profile along the growth direction (z), which actually marks by how much the measured vertical lattice constant (a_z) is larger or smaller than in a reference that is taken from AlAs_{0.56}Sb_{0.44} region.

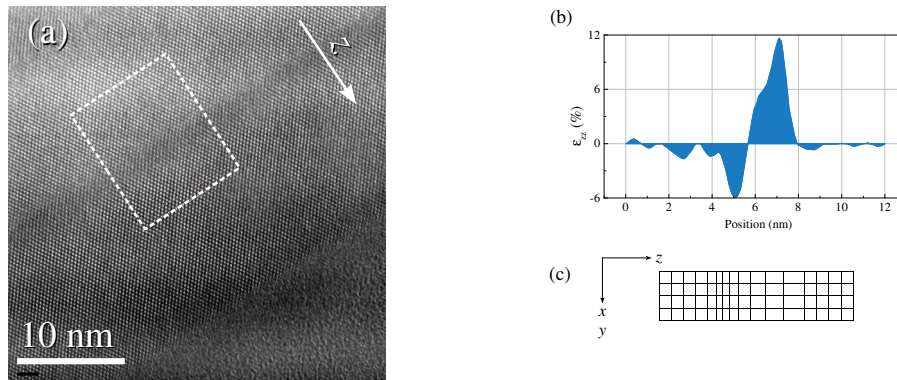


Figure 3.9: TEM study of the 7 ML InAs/AlAs_{0.56}Sb_{0.44} sample. (a) Its high-resolution TEM image and (b) ε_{zz} profile along z direction deduced by geometric phase analysis of the image. (c) gives a schematic illustration of the lattice that the ε_{zz} profile may correspond to.

In figure 3.9b, the regions where the deformation is lower than 0.01% ($z < 4$ nm) is considered to still belong to AlAs_{0.56}Sb_{0.44}. In the vicinity of $z = 5$ nm, where the lower InAs-on-AlAsSb interface is located, the out-of-plane (vertical) lattice constant a_z is about 6% smaller than the reference. By examining possible compounds that can be formed in the epitaxial growth, As-rich AlAs_{1-x}Sb_x or even pure AlAs are found to be candidate composition of this layer, for pure AlAs under tetragonal strain would produce an $\varepsilon_{zz} = -6.6\%$. Positively deformed region located between position $z = 5.5$ and $z = 6.5$ nm are related to the compressively strained InAs layer: when InAs is deformed to be coherent to InP substrate, its vertical lattice constant a_z is 6.7% larger than that of InP⁴. In the zone between $z = 7$ and $z = 8$ nm, where the AlAsSb-on-InAs interface is located, the deformation level has reached unexpectedly 10%. The only materials that can produce such high-level of strain are Sb-rich InAs_{1-x}Sb_x alloys. Eventually, the phase analyses suggest that the region near the InAs-on-AlAsSb interface is deprived of Sb, while the upper AlAsSb-on-InAs interface is enriched of it.

The Sb-rich interface could help explain the difference between experimental PL energies and those calculated by tight-binding calculations. We have simulated the transition energies of InAs/AlAsSb quantum wells with various As-rich lower interface (AlAs) and Sb-rich upper interface using $k \cdot p$ calculations. In figure 3.10 the calculated energies are compared with experimentally observed PL peak energies. The introduction of 1 ML of AlSb or InSb at the upper interface have both resulted in very good agreement between simulated transition energies and experimentally observed PL energies. Although such coincidence is not unequivocal, it does support Sb-rich upper interface concluded by TEM analyses.

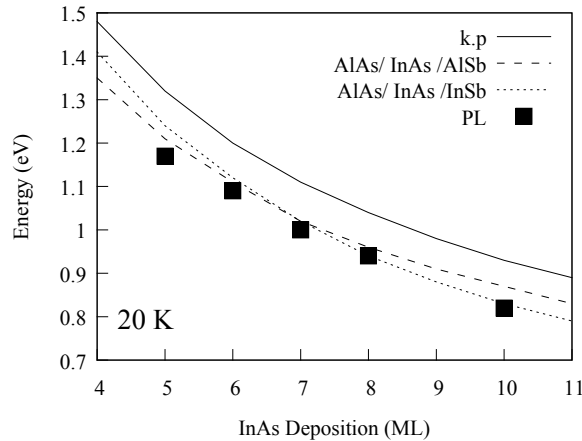


Figure 3.10: Comparison between PL energies of InAs/AlAs_{0.56}Sb_{0.44} single quantum wells and simulated transition energies in InAs/AlAs_{0.56}Sb_{0.44} quantum well with various types of interface layers.

⁴Due to possible surface relaxation in the thinned TEM sample, the observed a_z could be smaller than that in a un-cleaved sample; that is, the $\varepsilon_{zz} = 5.2\%$ may have underestimated the deformation in this layer, and its true value could be closer to its theoretical value $\varepsilon_{zz} = 6.7\%$.

Summary

By applying Sb-mediated growth, we thus obtained 7 ML-thick InAs/AlAsSb single quantum well of good quality, that is required for near-infrared inter-subband applications. At the same time, we determine that the pseudomorphic limit of Sb-mediated InAs layer to be around 10 ML. However, the quantity of InAs in a single quantum well is still too small for any practical use and it is necessary to produce multiple quantum wells by stacking these unit quantum wells. Without proper strain management, the cumulated strain will eventually lead to roughened surface or even plastic relaxation which severely degrades the optical and electronic properties of such multiple quantum well. In the coming section, a study will be presented on strain compensation in InAs/AlAs_{0.56}Sb_{0.44} multiple quantum wells.

3.4 Strain compensation in InAs/AlAs_{0.56}Sb_{0.44} multiple quantum wells

Strain compensation on InP substrate is a technique that allow the epitaxial growth of strained material with zero macroscopic strain [9]. Materials having smaller lattice constants are employed to compensates in-plane lattice constant dilatation brought about by materials having larger lattice constant, and vice versa. To compensate the strain caused by InAs/AlAs_{0.56}Sb_{0.44} quantum well, the simplest choice would be inserting certain amount of AlAs in each period of InAs/AlAs_{0.56}Sb_{0.44} in the middle of AlAs_{0.56}Sb_{0.44} barrier layer. This can be achieved by simply blocking Sb flux for certain time during the growth of AlAs_{0.56}Sb_{0.44} layer. The quantity of AlAs m required for compensating the strain introduced by 7 ML of InAs can be found by letting :

$$m \cdot \frac{a_{\text{AlAs}} - a_{\text{InP}}}{a_{\text{AlAs}}} + 7 \cdot \frac{a_{\text{InAs}} - a_{\text{InP}}}{a_{\text{InAs}}} = 0 \quad (3.1)$$

in which a_{\square} is natural (relaxed) lattice constant of each material. The solution to the above equation indicates zero net-strain InAs/AlAs_{0.56}Sb_{0.44} structure can be obtained by inserting about 6 ML of pure AlAs in the middle of AlAs_{0.56}Sb_{0.44} layer.

In order to find the actual quantity of AlAs required for compensating the strain introduced by 7 ML of InAs, we prepared several series of InAs/AlAs_{0.56}Sb_{0.44} multiple quantum well samples with the amount of AlAs in each period of quantum well varying from 6 to 8 ML. The unit structure in these samples is illustrated in figure 3.11a and it is repeated ten-time in each sample.

In this study, we compare two series of the samples. For the first series of two samples S980 and S981, their AlAsSb-on-InAs interfaces were terminated by 30 s As-based growth interruptions, which is expected to help purge the excess amount of Sb accumulated on InAs surface. For comparison, the second series of four samples

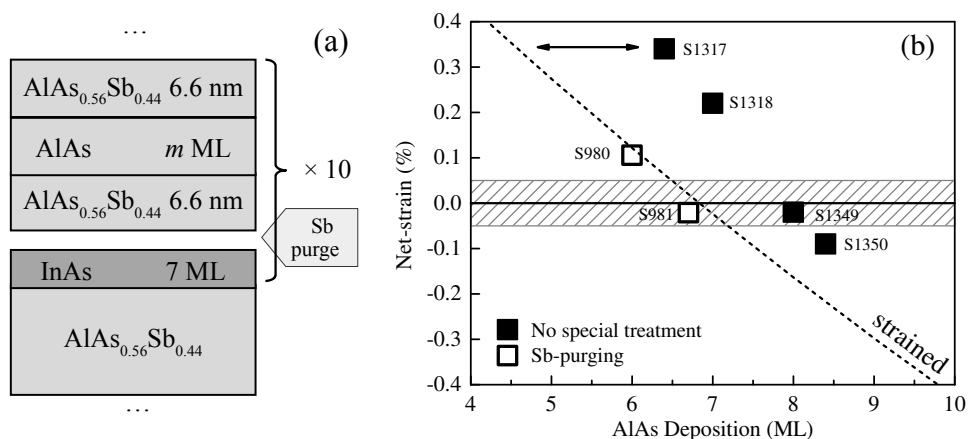


Figure 3.11: Strain compensation studied by XRD. (a) Unit structure of a strain-compensated samples. constant contraction. (b) The relation between amount of AlAs inserted into the structure and the net-strain of the structures.

(S1317,S1318,S1349,S1350), were grown without such Sb-purging procedure.

The net-strain, namely average lattice mismatch, in these multiple quantum wells were measured by routine XRD $\omega-2\theta$ checks and the results are summarized in figure 3.11b. For samples grown with Sb-purge, the evolution of mismatch is well approximated by formula (3.1), and very low level of net-strain was achieved by inserting 6.7 ML (S981) of AlAs in each period of the InAs/AlAs_{0.56}Sb_{0.44} quantum well. In contrast, for the samples without Sb-purge, one more ML of AlAs is generally needed, and 8 ML (S1349) of AlAs is needed to compensate the strain brought about by 7 ML InAs. At the same time, the evolution of residual strain follows different trend and they generally requires one more ML of AlAs to completely compensate the strain. Such difference suggests the Sb-purging growth interruption is equivalent to turning 1 ML of AlAsSb into pure AlAs.

The shaded area in figure 3.11b corresponds to net-strain level lower than 0.05%. According to plastic-relaxation criterion proposed by Matthews-Blackslee (equation (1.2), page 13), lattice mismatch of 0.05% can be tolerated by a epitaxial layer as thick as 760 nm. This thickness is equivalent to the 100-period Ga_{0.47}In_{0.53}As/AlAs_{0.56}Sb_{0.44} samples made for inter-subband absorption studies presented in section 2.2. Since the lowest net-strain levels achieved by strain compensation fall into the shaded area, they can be further stacked to fabricate a 100-period InAs/AlAs_{0.56}Sb_{0.44} multiple quantum wells.

S981, the structures showing lowest mismatch in routine XRD check was further studied by other means. Figure 3.12 a displays an asymmetric XRD reciprocal space map near its InP (224)+⁵ reflection. The red spot in the image corresponds to (224)

⁵The “+” symbol marks an asymmetric reflection with larger incident angle and smaller exiting angle.

diffraction of InP substrate while InAs/AlAsSb super-lattice satellite peaks appear as strips along in-plane directions. The lower panel of figure 3.12 demonstrates horizontal cross-sections taken from the mapping at various satellite peaks and the substrate peak. The horizontal directions in reciprocal space reflect the in-plane directions in real space. The center of these satellite peaks is well aligned with InP (224) reflection, confirming that the epitaxial layers are fully coherent to InP substrate. However, the in-plane line widths of satellites are significantly larger than that of the InP spot. Such observation suggests the interference condition is perturbed in in-plane direction of epitaxial layers.

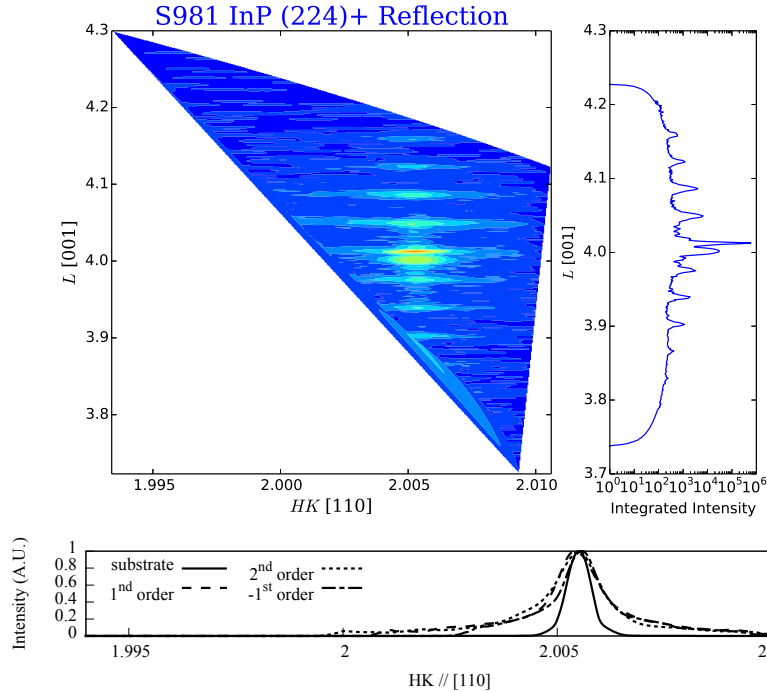


Figure 3.12: Upper panels: Reciprocal-space map of sample S981 and its vertical cross-section. Lower panel: its horizontal cross-sections taken at several satellite peak as well as substrate peak. The intensity is normalized to enable intuitive comparison of line shapes.

Figure 3.13 presents the low temperature PL emission of samples S981, compared with a previously studied 7 ML InAs/AlAsSb single quantum well sample (S958). The PL of multiple quantum well is both red-shifted as well as attenuated as compared to an InAs/AlAs_{0.56}Sb_{0.44} single quantum well, which could be a result of strain relaxation or elevated quantum well thickness fluctuation.

The microscopic structure of this sample is further scrutinized by cross-sectional TEM. Figure 3.14 presents a (002) dark-field TEM image of the structure, in which different layers can be identified by their different contrast and thicknesses. Unlike the previously studied 12 ML InAs/AlAsSb single-quantum-well sample (figure 3.7b), no dislocation is spotted in the observed first periods of the multiple quantum well; this suggests that the system has elastically relaxed by faceting, rather than plastic relaxation

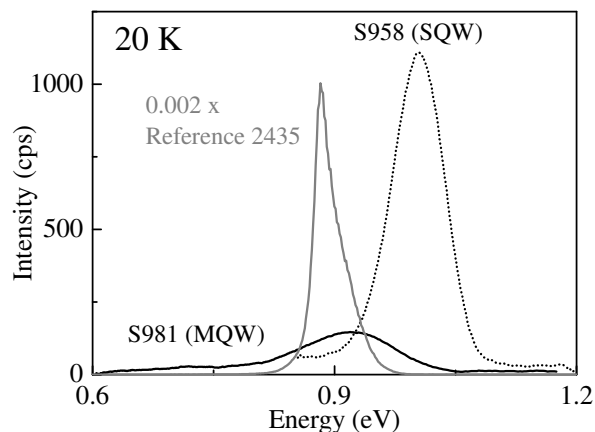


Figure 3.13: Low temperature PL of sample S981 compared to a previously studied 7 ML InAs/AlAsSb single quantum well sample (S958). The reference sample (2435) contains 5 GaInAsP/InP quantum wells and it is diminished by 500 times in the figure. PL emission peak intensity of AlAsSb-based samples is more than 500 times lower than it .

by generating dislocation as is the case of 12 ML InAs deposition (sample S977, TEM image in figure 3.7b).

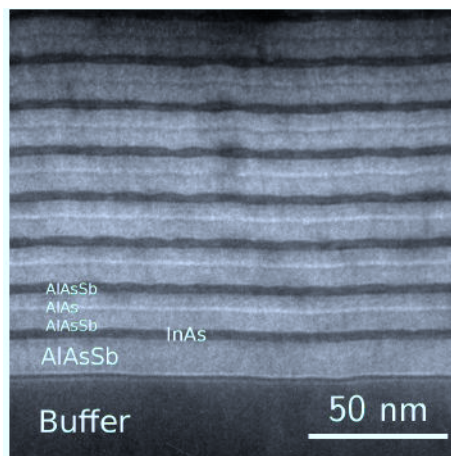


Figure 3.14: TEM (002) dark-field image of sample S981.

Figure 3.15a displays a high-resolution TEM image of samples S981, where the InAs layers are identified by the spacing between them and their thicknesses were found to be varying from 5 to 8 ML. Geometric phase analyses were also performed on the image to help identify the composition of the layers, and figure 3.15b presents the result ε_{zz} profile. ε_{zz} is strongly negative in the vicinity of $z = 9$ while the region from $z = 9.5$ to $z = 12$ is significantly compressively deformed. These features respectively account for the As-rich InAs-on-AlAsSb interface and the compressively strained InAs deposition, which already have been observed the in single quantum well sample (S958, figure 3.9a, page 62). Yet, the deformation level at its AlAsSb-on-InAs interface (5%) is not as

3.5. Polarization-dependent absorption in InAs/AlAs_{0.56}Sb_{0.44} multiple quantum wells

elevated as in the case of the single quantum well sample (S958 10%), despite that the same surface termination method was applied to them. It is also worth to be noted that the AlAs layers already observed in dark field image is not easily identified in the phase analyses; instead, constant negative deformation of 2% is found to be spreading in the middle of AlAs_{0.56}Sb_{0.44}, ranging from $z = 2.5$ to $z = 6$ in figure 3.15b. The in-plane inhomogeneity (undulations) observed in (002) dark-field image (figure 3.15a) could have disturbed the phase analyses so as the measured deformation is spread and averaged in z direction. Such interpretation needs further confirmation; nevertheless, the large fluctuation of InAs layer thickness and inhomogeneity in this sample will unsurprisingly lead to red-shifted PL energy and broadened PL peak in the PL studies.

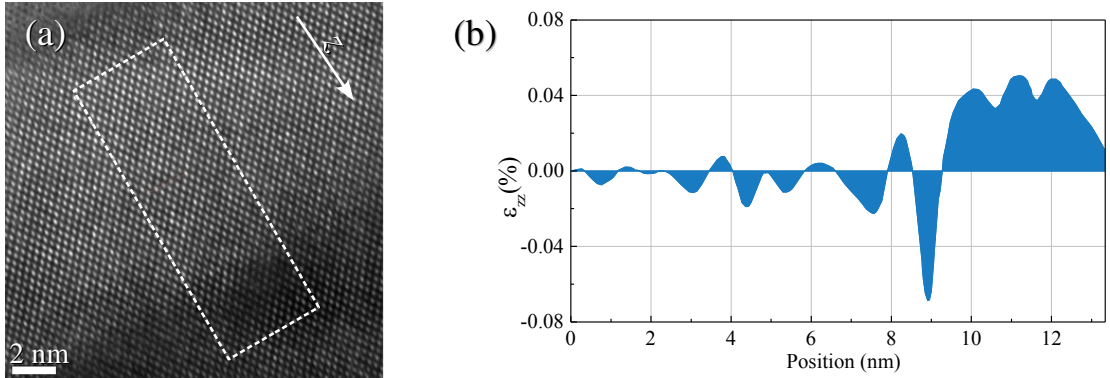


Figure 3.15: TEM observations of sample S981 (a) high-resolution TEM image (b) Geometric phase analysis ε_{zz} profile sampled at two different positions. The white rectangle in (a) indicatively illustrates the area analyzed in (b).

Summary

To conclude this section, we thus have experimented strain compensation in InAs/AlAs_{0.56}Sb_{0.44} quantum well by inserting AlAs layers in its AlAs_{0.56}Sb_{0.44} layer. We were able to achieve InAs/AlAs_{0.56}Sb_{0.44} quantum wells with very low-level of macroscopic net-strain in XRD observation. However, microscopic observations on the same structure indicate it has undulated layers and interfaces. This is thus the origin of broadened PL emission peak and low PL yield.

3.5 Polarization-dependent absorption in InAs/AlAs_{0.56}Sb_{0.44} multiple quantum wells

In this final section, we will present a preliminary study on inter-subband absorption in InAs/AlAs_{0.56}Sb_{0.44} quantum wells. Three strain-compensated InAs/AlAs_{0.56}Sb_{0.44} multiple quantum-well samples, S1363, S1364 and S1365 were fabricated for this purpose. They were prepared in the same manner as the strain-compensated samples presented in

the previous section, except that they were grown on semi-insulating InP:Fe substrates and their InAs layers are n -doped with Si. The three samples all contain 40 periods of InAs/AlAs_{0.56}Sb_{0.44} quantum wells, but they differ by the InAs layer thickness and subsequently the thickness of AlAs strain compensation layer, too. The principal structural parameters of these samples are listed in table 3.1.

Table 3.1: Structural parameters of strain-compensated InAs/AlAs_{0.56}Sb_{0.44} quantum wells made for inter-subband absorption study.

Sample	InAs Quantity (ML)	AlAs quantity (ML)	Period	Total thickness (nm)
S1363	5	6.4	40	≈680
S1364	6	7.4	40	≈680
S1365	7	8.4	40	≈680

After epitaxy growth, these samples were made into multi-reflection wave guide and they were tested in the same way as the Ga_{0.47}In_{0.53}As/AlAs_{0.56}Sb_{0.44} inter-subband absorbance samples in chapter 2, using the same workbench. Unfortunately, no room-temperature PL was detected for these samples so we assessed their inter-band properties by absorption experiments.

Figure 3.16a shows surface-normal incident absorption spectra of these samples at room temperature. The absorption edges in these spectra are in the shape of smooth slope instead of a steep one. Since the strain compensation in these samples was not optimized, the blurred absorption edge could be a result of growing inhomogeneity along the growth direction caused by accumulation of lattice-strain. Nevertheless, these absorption edges do shift towards longer wavelength as expected for thicker InAs quantum wells.

The absorption in these samples is then measured under multi-reflection mode, where the light beam travels in the interior of the samples by several total reflection. Figure 3.16b presents the polarization dependent absorption spectra of these sample, which are presented in (T_{TE}/T_{TM}). In this type of plot, inter-subband absorption between E_1 and E_2 , of which $T_{TE} > T_{TM}$, would appear as a peak above $y = 1$. Nevertheless, the current spectra are exactly the opposite, and valleys below $y = 1$ are observed for every sample which means that $T_{TE} < T_{TM}$.

As is discussed for equation (2.5) (page 28), $T_{TE} < T_{TM}$ is equivalent to $\alpha_{\text{inter-subband}} < \alpha_{\text{interband}}$, which indicate inter-band absorptions, especially the HH₁-E₁ process, could be responsible the observed anisotropy valleys. These valleys are in the same spectral range as the above mentioned absorption edges, and the bottom of these valleys also shift towards longer wavelength with increasing InAs thickness, which is also expected for inter-band absorption. Additionally, the optical properties of highly strained InAs

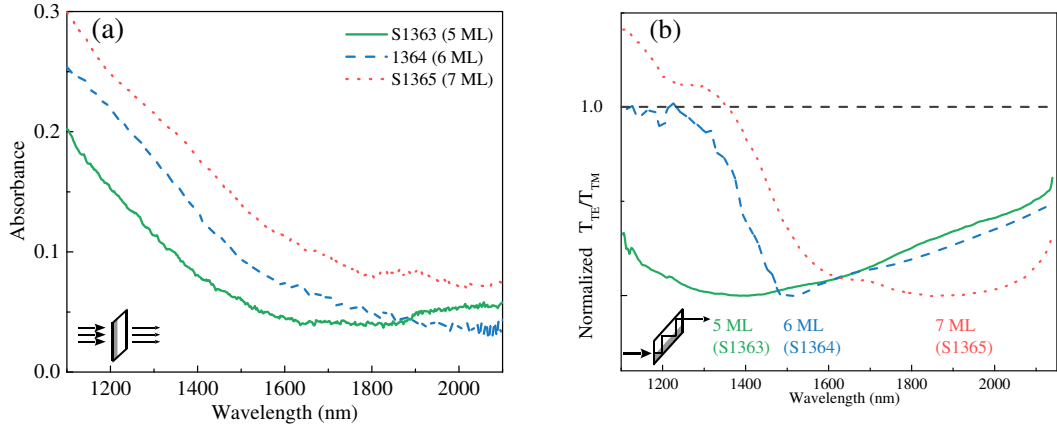


Figure 3.16: Room temperature absorption studies of strain-compensated InAs/AlAs_{0.56}Sb_{0.44} multiple-quantum-well samples. (a) surface-normal incident absorption spectra; (b) anisotropic absorption spectra under multi-reflection configuration (facet-incident).

quantum well could be anisotropic so that its in-plane absorption coefficients may differ ($\alpha_{LH1-E1,y} \neq \alpha_{LH1-E1,x}$ for example); this can also contribute to anisotropy expressed in T_{TE}/T_{TM} plot in figure 3.16b. On the other hand, the selection rules governing the polarization dependence of inter-band absorption may also be relaxed due to the inhomogeneity and microscopic strain existing in the material. So we cannot come to a conclusion of the origin of these absorption valleys (anisotropy) at this time.

Nevertheless, the anisotropic absorption spectra in figure 3.16b seem to be rising constantly and would probably arrive levels above $y = 1$ within the spectra range between 2300 nm and 3000 nm. Limited by the working wavelength of our current workbench, we do not have information on absorption spectra of these samples over 2100 nm. For the time of being, we are still on the development of a new workbench that enables absorption measurement in longer wavelength using an InSb detector.

Photo-induced absorption measurements

At the same time, we have also performed anisotropic absorption measurements using photo-induced absorption technique with the help of François Julien (IEF, Orsay). In his workbench, a Fourier transform infrared spectrometer and an HgCdTe detector was used so that absorption can be studied at longer wavelength.

The photo-induced absorption is a pump-probe technique that allows observation of inter-subband absorption in quantum well without doping. Figure 3.17 schematically demonstrates its experimental setup.

During the experiment, the epitaxial face of the multi-reflection waveguide is pumped by a 514 nm laser operating at 400 mW output, while the absorbance is measured by another probe-light beam that passes through the structure. The conduction-band ground-

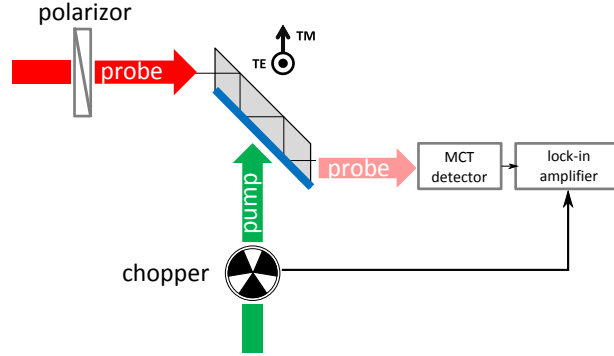


Figure 3.17: Schematic illustration of photo-induced absorption experimental setup.

level in a quantum well is populated by optical injection instead of using high-level n -doping. The photo-induced absorption is then measured by comparing the absorption spectra obtained with and without laser pumping. An advantage of this experiment is that no reference sample is required. In practice, the pump laser is modulated by a mechanical chopper and the photo-induced absorption variation $(\Delta T/T)_{TE}$ and $(\Delta T/T)_{TM}$ is picked up by a HgCdT detector connected to lock-in amplifier. Since the output of lock-in amplifier is the *magnitude* of the signal that is in-phase with laser modulation, it actually reflects the magnitude of photo-induced absorption change $|\Delta T/T|_{TE}$ (or $|\Delta T/T|_{TM}$)

S1056 is a strain-compensated InAs/AlAsSb multiple quantum well sample prepared for this study. This sample has the same structure as the previous studied sample S1361 (7 ML) except that the InAs layer inside S1054 is not doped with Si; it contains 40 periods of strain-compensated quantum wells, 7 ML of InAs is used in each InAs/AlAsSb quantum well and the structure is grown on semi-insulating InP:Fe (001) substrate. XRD check of this samples has shown its net-strain level is as low as -0.04%.

Figure 3.18 shows the photo-induced absorption spectra of sample S1054. The gray solid/dotted lines in this figure represent photo-induced transmittance changes $(|\Delta T/T|_{\square})$ measured under TM and TE probe-light polarizations. The transmittances show significant attenuation in the spectral range from 1.1 μm to 1.6 μm , for which both inter-subband transition ($E_2 - E_1 = 0.8$ eV, 1.55 μm and inter-band transitions ($E_1 - HH_1 = 1.1$ eV, 1.1 μm) could be responsible. Especially, the two curves are separated around 1.2 μm , which signifies an anisotropy of absorption.

The anisotropy absorption is better visualized by representing the data in :

$$\log_{10} \left(\frac{|\Delta T/T|_{TM}}{|\Delta T/T|_{TE}} \right)$$

and this is plotted as the solid black line in figure 3.18. The 1.2 μm peak flags significant absorption anisotropy and it seems to suggest that the optical injection has increased

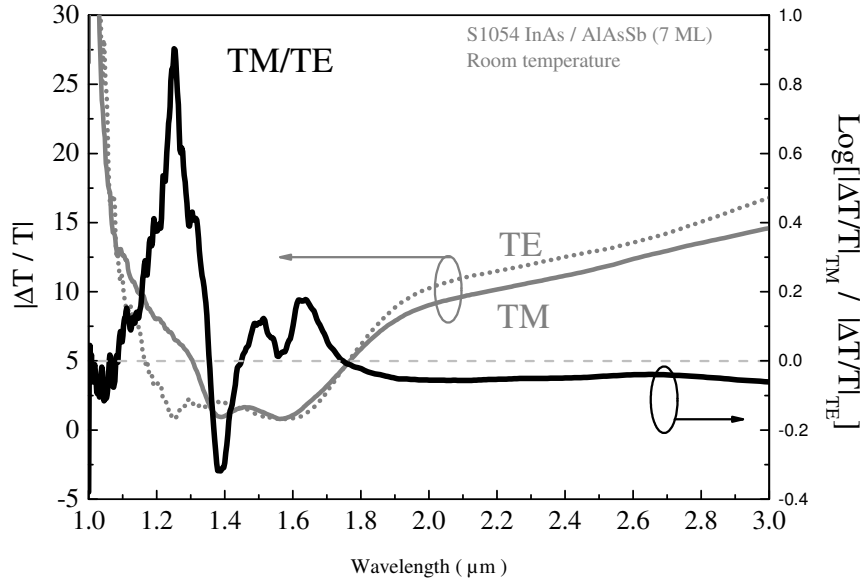


Figure 3.18: Photo-induced absorption spectra of sample S1054.

TM-absorption. This may correspond to the following situation: optical injection fills conduction-band ground-level E_1 and TM-absorption is increased due to E_1 - E_2 inter-subband absorption. Thus the 1.2 μm anisotropy peak could represent inter-subband transition in InAs/AlAsSb quantum wells. Judging by the inter-subband absorption linewidth as large as 600 nm (300 meV for sample S1346, page 33) that we have observed for GaInAs/AlAsSb quantum wells, 1.2 μm (1.0 eV) is actually not far from its theoretical position of 1.55 μm (0.8 eV). Nevertheless, in photo-induce absorption experiment, we only measure the magnitude of absorption change $|\Delta T/T|_{\square}$. It is also possible that the anisotropy peak in figure 3.18 stands for decreased TM-absorption. At the same time, this anisotropy valley is not far from the anisotropy valleys previously presented in figure 3.16b, so that the 1.2 μm anisotropic peak could also be attributed to inter-band processes ($E_1 - HH_1 = 1.1$ eV, 1.1 μm for example).

The difficulty for inter-subband absorption measurement in InAs/AlAsSb quantum wells lies in the fact its inter-band and inter-subband transition energies are actually close to each other. For the time of being, we cannot confirm the above results of absorption studies, without supplementary information on the subband positions in these sample (using photo-reflectance studies for example). Therefore, we have to conclude the study of InAs/AlAs_{0.56}Sb_{0.44} quantum well without inter-subband properties in this thesis, but it will remains a goal for future works.

Conclusion

In this chapter, we have demonstrated how Sb-mediated growth is useful in the growth of strained InAs layer on InP (001) substrate. We first found out that co-deposition of Sb is necessary to maintain its surfactant effect in the growth of InAs/AlAs_{0.56}Sb_{0.44} quantum well, albeit AlAs_{0.56}Sb_{0.44} surface before InAs deposition is already Sb-rich. Then using Sb-mediated growth we have achieved defect free InAs/AlAs_{0.56}Sb_{0.44} single quantum well as thick as 7 ML InAs deposition, which is required for realization of inter-subband transition in 1.55 μm band. By inserting AlAs layer in AlAs_{0.56}Sb_{0.44} barrier, we achieved InAs/AlAs_{0.56}Sb_{0.44} multiple-quantum-well with very low level of macroscopic strain. And eventually we performed preliminary studies on the absorption properties of such structures.

Two additional issues arise through the study of Sb-mediated growth. For one thing, it would be important to know how much Sb get incorporated in these InAs quantum wells under Sb-mediated growth. This topic will be investigated in chapter 5 ([Incorporation of Sb in Strained InAs\(Sb\) Heterostructures](#)). For another, despite Sb-mediated growth has induced two-dimensional growth InAs on InP (001) substrate, but it has seemingly failed to have the same influence on InAs/AlAs_{0.56}Sb_{0.44} structure grown on InP (113)B substrate (S845.2). This surface-orientation dependent surfactant effect would become the central topic of the following chapter 4 ([Sb-mediated Growth of InAs/GaAs_{0.51}Sb_{0.49} Heterostructures on InP Substrate](#)).

References

- [1] J.-M. Jancu et al., “Empirical spds* tight-binding calculation for cubic semiconductors: general method and material parameters”, [Physical Review B](#) **57**, 6493–6507 (1998).
- [2] T. F. Kuech, “Surfactants in semiconductor epitaxy”, in [AIP conference proceedings](#), Vol. 916 (2007), p. 288.
- [3] E. Tournié et al., “Surfactant-mediated molecular-beam epitaxy of III–V strained-layer heterostructures”, [Journal of Crystal Growth](#) **150**, Part 1, 460–466 (1995).
- [4] D. Kandel and E. Kaxiras, “The surfactant effect in semiconductor thin-film growth”, [Solid State Physics Volume](#) **54**, 219–262 (1999).
- [5] R. Kaspi and K. R. Evans, “Sb-surface segregation and the control of compositional abruptness at the GaAsSb/GaAs interface”, [Journal of Crystal Growth](#) **175–176**, Part 2, 838–843 (1997).
- [6] J. C. Harmand et al., “GaInAs/GaAs quantum-well growth assisted by sb surfactant: toward 1.3 μm emission”, [Applied Physics Letters](#) **84**, 3981–3983 (2004).
- [7] C. Gatel et al., “Analysis by high-resolution electron microscopy of elastic strain in thick InAs layers embedded in Ga_{0.47}In_{0.53}As buffers on InP(0 0 1) substrate”, [Acta Materialia](#) **58**, 3238–3246 (2010).
- [8] O. Brandt et al., “Effect of in segregation on the structural and optical properties of ultrathin InAs films in GaAs”, [Applied Physics Letters](#) **61**, 2814–2816 (1992).
- [9] B. I. Miller et al., “Strain-compensated strained-layer superlattices for 1.5 μm wavelength lasers”, [Applied Physics Letters](#) **58**, 1952–1954 (1991).

3.5. Polarization-dependent absorption in InAs/AlAs_{0.56}Sb_{0.44} multiple quantum wells

Chapter 4

Sb-mediated Growth of InAs/GaAs_{0.51}Sb_{0.49} Heterostructures on InP Substrate

InAs/InP quantum-dot based laser is one of the main research activities of FOTON laboratory. These nanostructures are usually obtained by directly depositing InAs on buffer layers that are lattice-matched to InP substrate. In this chapter, we will study the deposition of InAs on the surface of GaAs_{0.51}Sb_{0.49} buffer layer. The growths of such structures on (001) and (113)B-oriented InP substrate have led to very different results: InAs/GaAs_{0.51}Sb_{0.49} quantum wells are obtained on InP (001) substrate, while InAs/GaAs_{0.51}Sb_{0.49} quantum dots are formed under Volmer-Webber growth mode on InP (113)B substrates. The structural and optical properties of these nanostructures will be examined in section 4.2, but it takes another final section 4.3 to understand how the surfactant effect of Sb is responsible for these phenomena.

4.1 InAs quantum dots on grown on (001) and (113)B substrates

The InAs/InP nanostructures made for laser applications are usually obtained by depositing InAs on to a buffer layer that is coherent to InP substrates like $\text{Ga}_x\text{In}_{1-x}\text{As}_y\text{P}_{1-y}$. These nanostructures are usually formed under Stranski-Krastanow growth mode, in which the deposition of InAs switches to three-dimension growth mode only after small amount of deposition. The formation of three-dimensional object is often monitored by reflective high-energy electron diffraction during MBE growth. The onset of InAs nanostructures' formation is accompanied by the appearance of chevron-like diffraction patterns and thus a *critical thickness* required for island formation can be measured. For the smaller lattice mismatch between InAs/InP (3.2%) than between InAs/GaAs (7.2%), experimentally observed critical thickness of InAs deposition on InP (001) substrate varies from 2 ML to 2.5 ML [1, 2], which is slightly larger than that of InAs/GaAs quantum dots (1.5-1.8 ML).

Unlike InAs quantum dots obtained GaAs (001) substrate, the shape of MBE grown InAs nanostructures on InP (001) substrates may vary from elongated 'quantum dashes' to more isotropic quantum dots. AFM images in figure 4.1a demonstrates the shape of InAs/ $\text{Ga}_{0.20}\text{In}_{0.80}\text{As}_{0.44}\text{P}_{0.57}$ /InP (001) quantum dashes formed by 3 ML of InAs deposition, where prism-like quantum dashes are aligned along one of the $\{110\}$ directions. The TEM image in figure 4.1b displays trapezoidal cross-sections of two InP-capped InAs nanostructures [2]. By generalizing more RHEED and TEM observations of InAs/InP(001) deposition, it is speculated that these InP-capped InAs/InP(001) nanostructures have the shape of truncated pyramid with high Miller-index $\{114\}$ facets [3, 4], as illustrated in the inset of figure 4.1b.

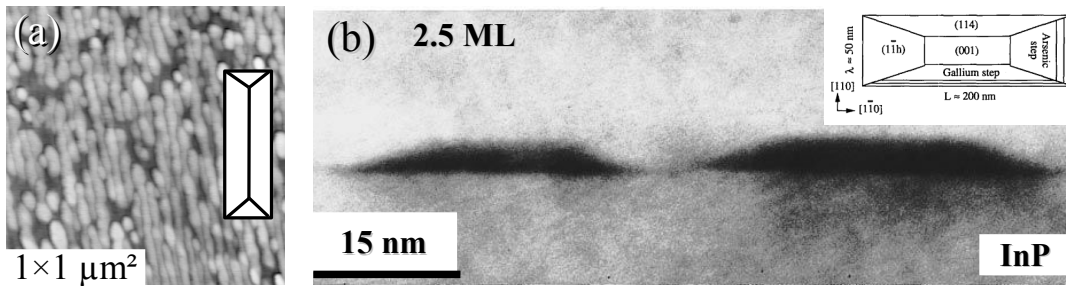


Figure 4.1: AFM and TEM observation of InAs nanostructures grown on InP (001) substrates. (a) AFM plan-view of InAs/ $\text{Ga}_{0.20}\text{In}_{0.80}\text{As}_{0.44}\text{P}_{0.57}$ islands formed by 3 ML of InAs deposition (b) $(0\bar{1}0)$ cross-section view of InP-capped InAs/InP quantum dots formed by 2.5 ML of InAs deposition [2]. Inset of (b): The shapes of InAs/ $\text{Ga}_{0.47}\text{In}_{0.53}\text{As}$ nanostructures generalized by more TEM observations [3]

On InP (001) substrate, isotropic InAs islands can be achieved by using very higher

AsH₃ flow rate (As₂ flux) during the deposition of InAs ; however, by doing so the number density of nanostructures is also reduced. The AFM image in figure 4.2a demonstrates InAs/Ga_{0.20}In_{0.80}As_{0.44}P_{0.57}/InP(001) quantum dots obtained by 2.1 ML InAs deposition under such growth conditions, where large InAs islands are formed by coalescence of smaller ones. The formation of these ripened islands may lead to plastic relaxation of InAs deposition and degrades their optical and electrical properties.

The need for high-density InAs/InP quantum dots can be met by depositing InAs on InP (113)B substrate. The AFM image in figure 4.2b shows InAs/Ga_{0.20}In_{0.80}As_{0.44}P_{0.57}/InP(113)B quantum dots obtained by the same 2.1 ML of InAs deposition. In contrast to what is observed on InP (001) substrate, their density are as high as $5 \times 10^{10} \text{ cm}^{-2}$ and yet no coalesced islands are spotted. Figure 4.2c offers an STM plane-view of a single InAs/Ga_{0.20}In_{0.80}As_{0.44}P_{0.57}/InP (113)B quantum dot formed by 2.1 ML of InAs deposition. The island has different symmetry as compared to its counterparts formed on InP (001) substrate, and its surface is dominated by low Miller-index side facets in {001}, {110} and {111} family.

The critical thickness required for InAs island formation on InP (113)B substrate is determined to be about 1.6 ML [5], which is even smaller than on InP (001) substrate. Low-index surfaces like (001) have well-defined surface reconstruction and they usually has lower surface energy than high-index surfaces like (113). Therefore, the surface of an InAs/InP (113)B quantum dot which is mainly composed of low-index facets, have lower free energy density than an island formed on InP (001) substrate which is composed of high-index facets. By consequence, the nucleation of InAs quantum dot is easier on InP (113)B substrate, so that InAs/InP (113)B quantum dots have smaller critical thickness (volume), smaller average size and higher number density than their counterparts formed on InP (001) substrate.

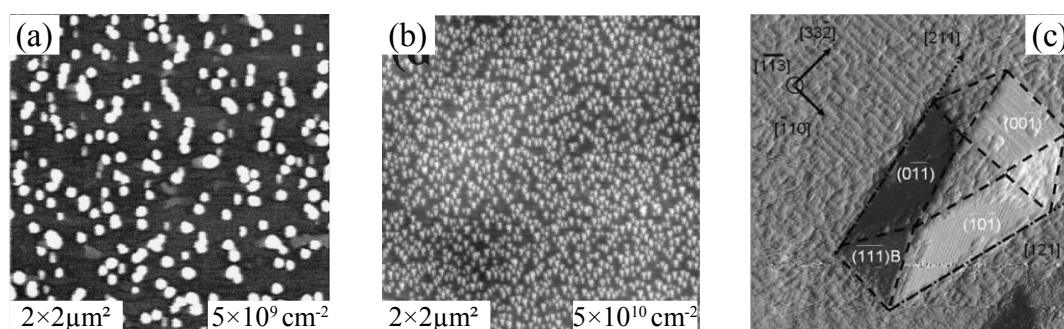


Figure 4.2: (a) and (b) are AFM images of InAs quantum dots formed by 2.1 ML of InAs deposition on (001) and (113)-oriented InP substrates, respectively. [6]. (c) STM plan-view of an individual InAs/InP (113)B island formed by 2.1 ML of InAs deposition; crystallographic orientations of its facets are annotated in-place. [7]. These samples were grown by gas-source MBE.

Most optical applications requires quantum dots be covered by another layer of bar-

rier material to isolate them from surface-related problems. However, this capping layer may raise other concerns due to its intermixing with InAs islands [8]. Figure 4.3a shows an X-STM view of an InP-capped InAs quantum dot sitting on its wetting layer [9]. Unlike surface quantum dots observed by plan-view STM (figure 4.2c) which have relative pointed shape, encapsulated quantum dots are much flatter and they have much larger top facet (plateau).

As a matter of fact, the summit of InAs island is where strain is most concentrated; hence, it is more likely to intermix with capping material so as to relax the strain energy, which could be undesired. The shape of InAs quantum dots can be preserved if Sb is involved in the growth. Figure 4.3b shows an InAs/InP (113)B quantum dot encapsulated by a lattice-matched $\text{GaAs}_{0.51}\text{Sb}_{0.49}$ layer [10], which has more pointed shape than the InP-capped island to its left. Judging by the form of its $(1\bar{1}0)$ cross-section, the shape of the island should be similar to the uncapped InAs/InP(113) island observed by plan-view STM in figure 4.2c. The same shape preserving effect is observed even only elemental Sb is supplied in the growth of InAs quantum dot. Figure 4.3c shows the cross-section of InP-capped InAs/InP (113)B quantum dot that has experienced short Sb_2 irradiation before the growth of capping layer. The island has also has even more pointed shape and Sb atoms, which are identified as individual bright spot in the image, only concentrate at the interface between the island and the InP capping layer. This suggests the mechanism of island shape preservation has its origin in surface processes.

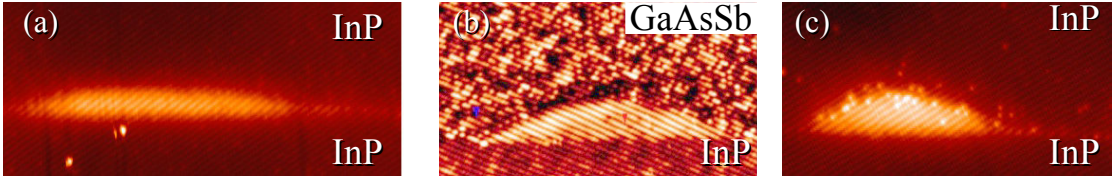


Figure 4.3: High-resolution cross-sectional STM images of capped InAs/InP islands. (a) InP-capped InAs/InP (113) islands [11]. (b) $\text{GaAs}_{0.51}\text{Sb}_{0.49}$ -capped InAs/InP (113) islands (c) InP-capped InAs/InP (113) island annealed under Sb_2 -based growth interruption [10]. These images were taken under constant current mode with negative sample bias. These samples were prepared using solid-source MBE.

Beneficial effect of Sb in the growth of InAs quantum dots have also been reported by many researchers. They include higher island density [12, 13], more uniform island size distribution [14, 15], suppression of coalesced islands [16] and enhanced optical properties [15, 17, 18]. In many of these studies, Sb is supplied before the deposition of InAs, via Sb-containing buffer layer for example. However, the majority of these studies were conducted on GaAs (001) substrate only. In the next section, we will explore the influence of Sb-rich $\text{GaAs}_{0.51}\text{Sb}_{0.49}$ buffer layer on the growth of InAs deposition on both its (001) and (113)B surface. To begin with, we will shortly present InAs/ $\text{GaAs}_{0.51}$ -

Sb_{0.49} as a material system.

4.2 InAs/GaAs_{0.51}Sb_{0.49} quantum wells on InP (001) substrate

InAs/GaAs_{0.51}Sb_{0.49} type-II heterostructure

GaAs_{0.51}Sb_{0.49} is another frequently used antimonide ternary alloys that is lattice-matched to InP substrate. It has a direct band-gap of $E_G^\Gamma = 0.7$ eV at room temperature, and it forms type-II heterostructures when paired with pseudomorphic InAs. Figure 4.4a demonstrates the band-alignment of a quantum well formed by these two materials. Due to the staggered type-II line-up, radiative recombination in such a structure has to occur indirectly between electrons confined in InAs layer and holes distributed in GaAs_{0.51}Sb_{0.49} layer.

The fundamental transition energies in InAs/GaAs_{0.51}Sb_{0.49} quantum well can be calculated using $k \cdot p$ method and figure 4.4b plots $k \cdot p$ simulated transition energies as a function of InAs quantum well thickness. On one side, the calculations indicate mid-infrared emission near 3 μm (0.4 eV) can be achieved with moderate quantum well thickness of 10 ML (3 nm), which makes InAs/GaAs_{0.51}Sb_{0.49} potentially useful for extending emitting wavelength available on InP substrate. On the other side, as we have demonstrated in chapter 3, strained InAs quantum well as thick as 10 ML (3 nm) could be a challenge for MBE growth on InP substrate, even if Sb is used as a surfactant. Fortunately InAs/GaAs_{0.51}Sb_{0.49} quantum dot remains an alternative choice. Similar to a quantum well, the energy levels in a quantum dot are largely determined by its height. Nevertheless, for the same amount of InAs deposited, InAs quantum dots can reach larger height thus longer emission wavelength than a quantum well. Partially relaxed surface of quantum dots makes them less likely to generate carrier trapping defects like dislocations, and at the same time their coherence with the matrix layer ensures their good optical quality.

A very important aspect of type-II heterostructure is its excitation power dependent PL emission wavelength. When the structure is photo-excited, photo-generated electrons and holes are spatially separated by the type-II interface. Such separation creates band-bending and introduces discretized hole-levels near the InAs/GaAsSb interface. This is illustrated in the inset of figure 4.5. By increasing excitation power in PL experiment, larger band-bending is induced and the energy levels of electrons and holes are further separated so that radiative emission of the type-II heterostructure is shifted towards higher energies.

In figure 4.5, calculated fundamental transition energies in a 4 ML (1.2 nm) thick InAs/GaAs_{0.51}Sb_{0.49} quantum well are plotted against excitation powers to the one-third power ($P^{1/3}$). The quasi-linearity found between the two quantities is prevalently used

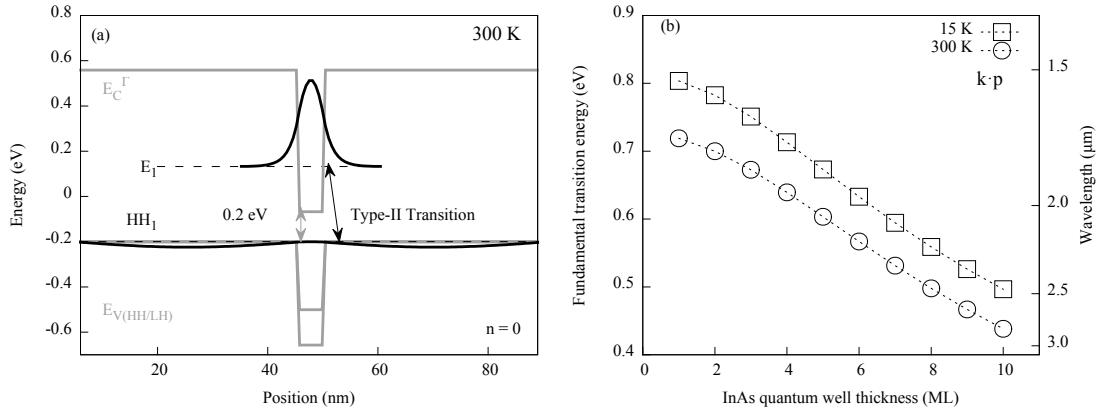


Figure 4.4: InAs/GaAs_{0.51}Sb_{0.49} strained quantum well. (a) shows its type-II band-alignment while (b) displays simulated transition energies in such a quantum well as a function of InAs layer thickness.

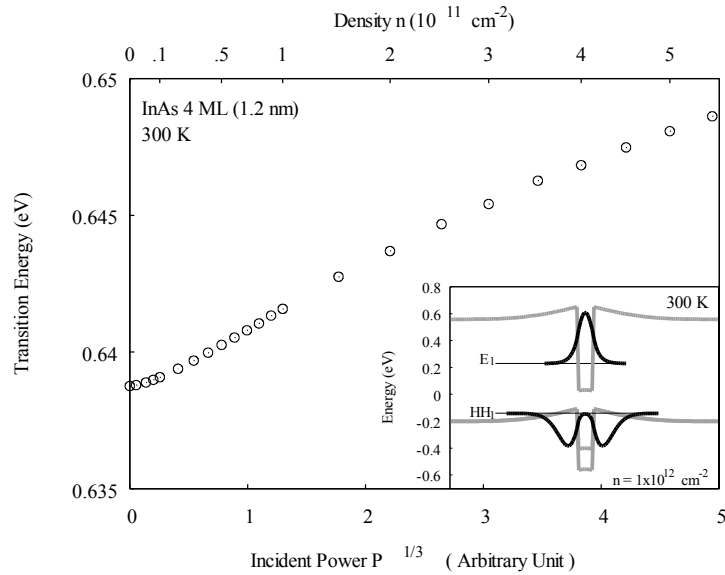


Figure 4.5: Fundamental transition energy in InAs/GaAs_{0.51}Sb_{0.49} quantum well under different excitation powers. Inset: Band-alignment and subband energies in a InAs/GaAs_{0.51}Sb_{0.49} quantum well under injected electron density of $n = 1 \times 10^{12} \text{ cm}^{-2}$. The magnitudes of wavefunctions are superposed on energy levels.

as a signature of type-II hetero-structure. Such linearity also ensures that in case PL emission cannot be measured at low excitation energies, one can still estimate fundamental transition energy of a type-II nanostructure by extrapolating power-dependent PL energies to $P = 0$ ($n = 0$).

Growth of InAs/GaAs_{0.51}Sb_{0.49} quantum well on InP (001) substrate

InAs deposition on (001) surface of GaAs_{0.51}Sb_{0.49} is examined via three types of samples, separately prepared for AFM, PL and cross-sectional TEM observations. All samples presented in this study were grown by solid source MBE on *n*-type InP (001) substrates, and the substrate temperature was fixed at 450 °C during all growth runs. Diatomic As₂ and Sb₂ fluxes were used and the beam equivalent pressure ratio between group V and III elements was kept low during the growth of GaAs_{0.51}Sb_{0.49} alloy to ensure good control over its composition [19, 20]. The lattice-matching condition of GaAs_{0.51}Sb_{0.49} was assured by X-ray diffraction on test samples. The indium growth rate was set to 0.11 ML/s, which was calibrated using strained super-lattice samples.

Each AFM sample contains one layer of InAs deposition on its surface. After the growth of GaAs_{0.51}Sb_{0.49} layer, only 2 s growth interruption under As₂ flux was performed to stabilize the fluxes and immediately InAs of 3, 4 or 5 ML were deposited without supplying Sb. Following that, another growth interruption of 30 s under As₂ flux was performed before the samples were cooled down at the fastest rate possible (~ 1 °C/s) under protection of As₂ flux.

Each sample made for PL characterization contains one layer of InAs deposition embedded in two layers of GaAs_{0.51}Sb_{0.49}. These samples were elaborated under the same conditions as those in the previous set, but the InAs deposition quantity now ranges from 1 ML to 5 ML. The InAs deposition is also annealed under a 30 s As₂ growth interruption and then it is covered by a 40 nm-thick GaAs_{0.51}Sb_{0.49} capping layer. The common structure of these PL samples is illustrated in figure 4.6. In order to suppress type-II transition occurring at GaAsSb/InP interfaces [21], two additional layers of AlAs_{0.56}Sb_{0.44} were added around the two GaAs_{0.51}Sb_{0.49} layers.

An additional sample (S997.1) was prepared for TEM observation. Similar to the PL sample, it contains only InAs deposit of 5 ML. However, this time the InAs surface was annealed under As₂ flux for 5 s before it is covered by a 50 nm-thick GaAs_{0.51}Sb_{0.49} capping layer. The cross sections for TEM observation were prepared under standard procedures consisting of mechanical material removal and ion milling. The TEM observations were performed on a FEI-TECNAI microscope equipped with field emission electron gun and spherical aberration correctors to avoid interface delocalization. TEM observations and analyses were performed by Julien Nicolai from Centre d'Elaboration de Matériaux et d'Etudes Structurales (Toulouse, France).

The contact mode AFM images in figure 4.7 presents the surface morphology of In-

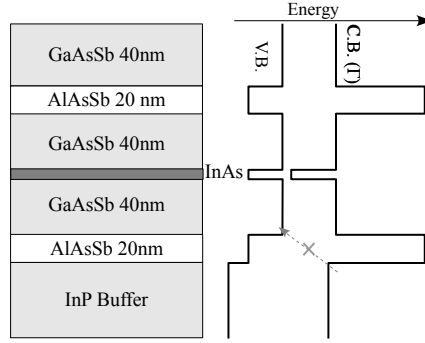


Figure 4.6: Sample structure of PL samples and their band-alignment. Two $\text{AlAs}_{0.56}\text{Sb}_{0.44}$ layers are added around the active region to suppress surface recombination and type-II transition at the $\text{GaAs}_{0.51}\text{Sb}_{0.49}/\text{InP}$ interface, which is marked by the crossed-out arrow.

$\text{As}/\text{GaAs}_{0.51}\text{Sb}_{0.49}$ (001) depositions, which are relatively flat. For 5 ML InAs deposition sample (S1147.1)¹, several island-like objects are scattered over figure 4.7c, but these islands are actually small in height. This is marked by root-mean-square (RMS) surface roughness of about 0.2 nm, which is small compared to cases where ‘real’ quantum dots are formed ($\text{RMS} > 1$ nm). Since the critical thickness of InAs deposition on InP (001) substrate is usually no larger than 2.5 ML without the presence of Sb, the formation of InAs dash or dots is thus the expected behavior for 3–5 ML InAs deposition. We thus attribute the relatively flat surfaces obtained on (001) surface of $\text{GaAs}_{0.51}\text{Sb}_{0.49}$ to surfactant effect of Sb, like in the 7 ML-thick InAs/ $\text{AlAs}_{0.56}\text{Sb}_{0.44}$ quantum well presented in chapter 3.

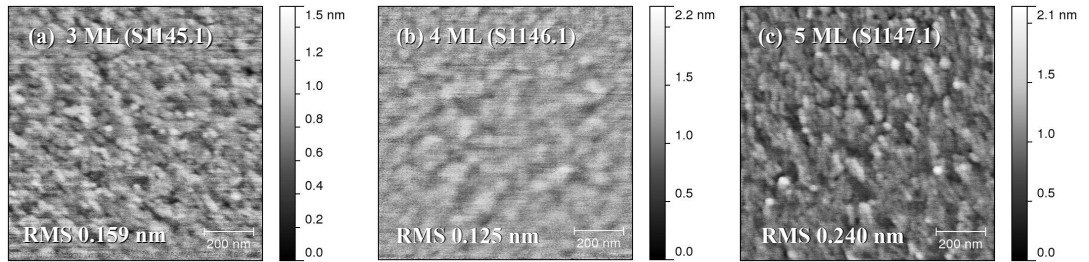


Figure 4.7: Surface InAs deposition on (001) surface of $\text{GaAs}_{0.51}\text{Sb}_{0.49}$, observed by contact mode AFM. The scanned areas are $1 \times 1 \mu\text{m}^2$

Figure 4.8a shows a TEM image of S997-1 (5 ML). This dark-field image was taken under (002) conditions so that each material layer can be distinguished by its chemical contrast. The InAs layer is identified as the bright line between two thick GaAsSb layers, and it forms an entire layer although its interfaces do not appear perfectly flat. Such observation agrees with the flat surfaces observed by AFM inspection and the

¹The suffix “□.1” are given to samples made on (001) substrate, while their counterparts made on (113)B substrates are named “□.2”.

embedded InAs layers can thus be considered as quantum-wells. Figure 4.8b presents a high-resolution TEM image near the InAs layer, which is represented by the dark area that crosses the image diagonally. The InAs layer is fluctuating from place to place and its thickness is determined to be 5–7 ML by applying geometric phase analyses (not shown).

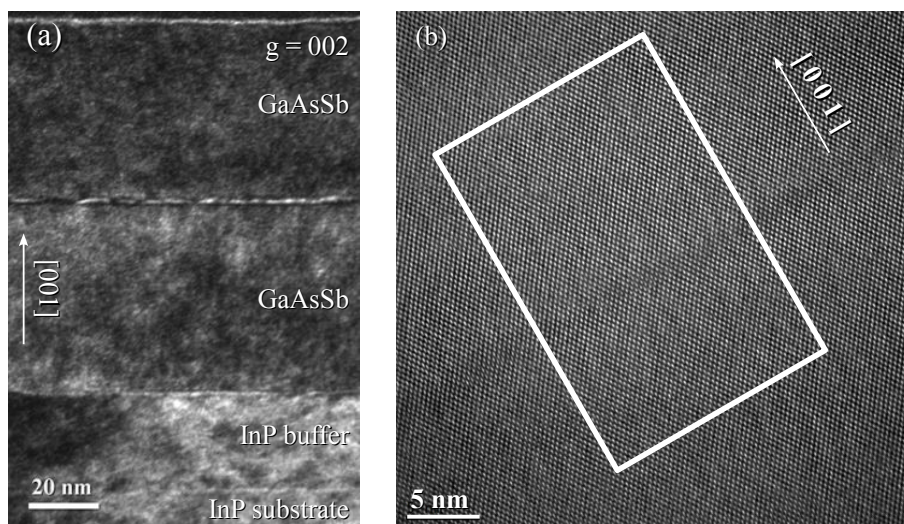


Figure 4.8: TEM cross-section views of sample S997-1 which contains 5 ML of InAs deposition sandwiched by two 50 nm-thick GaAsSb layers. (a) Its dark-field image demonstrating all the layers in the sample (b) an high-resolution image near the InAs deposition.

PL characterization on InAs/GaAs_{0.51}Sb_{0.49} quantum wells were at first performed at room temperature. Figure 4.9a demonstrates PL spectra of InAs/GaAs_{0.51}Sb_{0.49} quantum wells containing from 1 to 5 ML of InAs depositions. Two emission peaks are present in each PL spectra except for the 1 ML sample. Low energy peaks located between 0.6-0.7 eV red-shift with increased InAs deposition, while high-energy peaks at about 0.75 eV are independent of it. Figure 4.9b shows two PL spectra of 4 ML InAs/GaAs_{0.51}Sb_{0.49} quantum well (S1340.1), obtained under different excitation power of 40 times difference. While the high-energy peak remains at constant energy, the lower energy peak blue-shifts as excitation power increases. The PL peak is plotted as a function of cubic root of PL excitation power in the inset of figure 4.9b, and the good linearity between the two quantities is the signature of type-II heterostructures. The low energy peak is thus attributed to InAs quantum-well related type-II transition and the constant PL peak at 0.75 eV is attributed to direct transition within GaAs_{0.51}Sb_{0.49} layer. By comparing the PL energies–carrier density plot presented in figure 4.5, we conclude that the maximum excess carrier density during PL experiment is about $4 \times 10^{11} \text{ cm}^{-2}$.

In the inset of figure 4.9a, and the low excitation power PL peak energies of all PL samples are compared with transition energies calculated under zero-excitation (already

presented in figure 4.5). The two datasets agree well with each other, and the calculations indicate that the fundamental level transition for 1 ML-thick InAs/GaAs_{0.51}Sb_{0.49} quantum well is so close to the band-gap of GaAs_{0.51}Sb_{0.49} that the emission from it could have been submerged by PL emission from GaAsSb layer.

In figure 4.9b, the PL spectra are normalized by the intensities of quantum-well related PL peak. The normalized intensity of GaAsSb peak increases at increased excitation power. This indicates that its associated recombination rate is growing faster than that of quantum-well related process, and it seems to suggest that the direct transition of GaAsSb occurs in the part of GaAsSb layers that is adjacent to quantum well layer. More carriers are generated at higher excitation power, the electrons have greater chance escaping from InAs quantum well so that there is a competition between the indirect transition at the InAs/GaAsSb interface and direct transition near the interface.

Finally, PL characterizations of these samples were also performed at temperatures ranging from 15 K to room temperature. Figure 4.10 demonstrates the temperature dependence of GaAsSb PL emission energy and it has obvious deviation from Varshni's empirical formula ² at low temperature. This suggests that the direct transition in this layer could be related to localized recombination centers, and this partly explains why the PL emission of GaAs_{0.51}Sb_{0.49} as a barrier material is observed.

In short, the above results show that InAs deposition on InP (001) substrate under the presence of Sb leads to the formation of InAs quantum well despite that as much as 5 ML of InAs has been deposited. These results again demonstrate that the use of Sb during InAs deposition on InP (001) substrate can effectively eliminate the formation of islands.

Growth of InAs/GaAs_{0.51}Sb_{0.49} quantum dots on InP (113)B substrate

In this section, the study of structural and optical properties of InAs/GaAsSb nanostructures is carried on InP (113)B substrates through three sets of samples, each prepared for AFM, PL and cross-sectional STM studies. Accompanying each structure grown on (113)B substrate, another sample is simultaneously grown on (001) substrate to facilitate various calibrations. And actually the (113)B AFM (PL) samples were prepared in the same growth runs as the previously presented AFM (PL) samples made on InP (001) substrate. Subsequently, the InAs deposition quantities in this section are actually expressed in (001) ML. (113) crystallographic planes has lower surface density than (001) ones so that one (001) ML equals to 1.9 (113) ML; however, for the two samples prepared in the same growth-run, the thicknesses of InAs deposition are the same on the two types of substrates, and thus the total strain energies stored in InAs deposition are the same on both substrate orientations.

²Varshni's formula on temperature dependent band-gap: $E_g(T) = E_g(0) - \alpha T^2 / (T + \beta)$. α and β are empirical parameters that have to be determined experimentally.

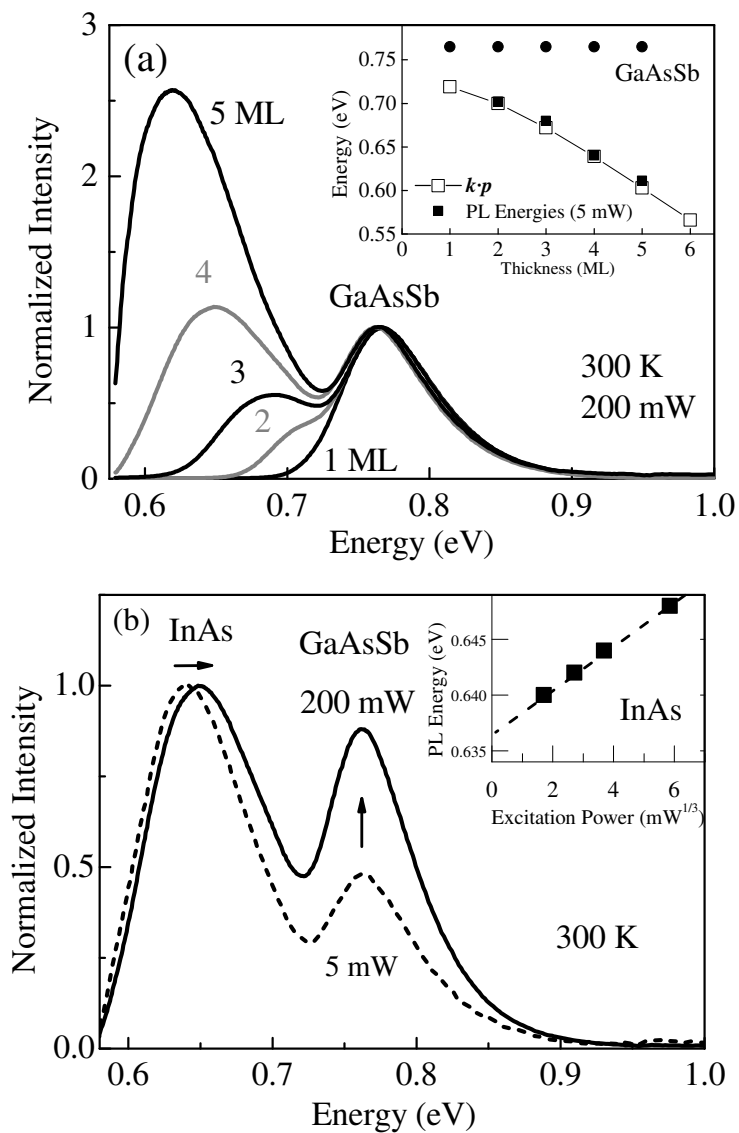


Figure 4.9: Room temperature PL of InAs/GaAsSb (001) quantum well samples. (a) PL spectra of InAs/GaAsSb, normalized by GaAsSb-related emission peak. (b) PL spectra of sample S1340.1 (4 ML) under different excitation powers, normalized by quantum well related emission peaks; the inset shows the excitation power dependence of InAs quantum well emission peak energy.

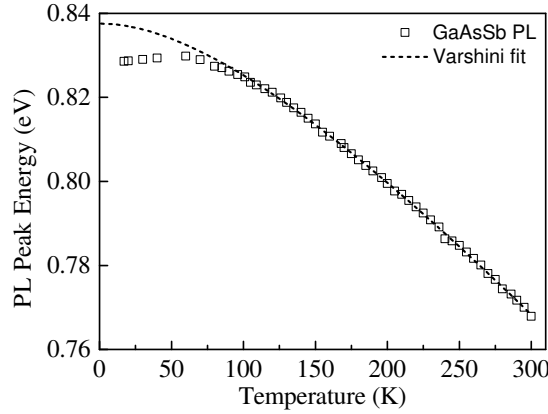


Figure 4.10: Temperature dependence of GaAsSb PL emission peak energy suggests localized levels are involved.

The sample made for X-STM observation contains four planes of InAs deposition of 3, 4, 5 and 6 ML-thick. These QD planes are separated by 40 nm-thick GaAsSb layers to limit strain propagation. Their growth conditions were identical to PL samples, except that the GaAsSb layers were doped with Si to make the entire structure conductive. In X-STM measurements, clean cross-sections were obtained *in situ* by cleaving the samples along one of its $\{110\}$ natural cleavage planes under ultra-high vacuum environment. The STM measurements and analyses were performed by Samuel Mauger at Technische Universiteit Eindhoven (Eindhoven, the Netherlands).

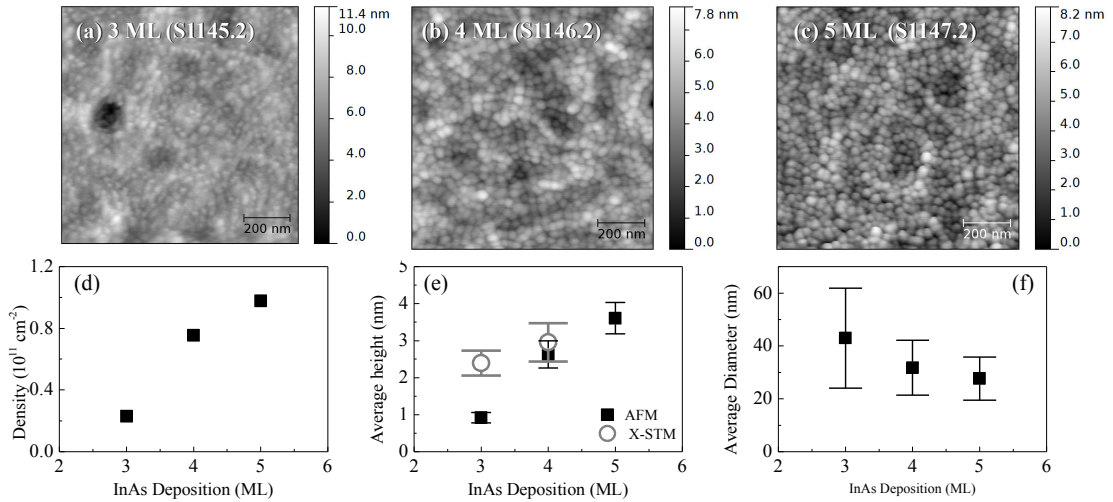


Figure 4.11: AFM observation of InAs islands obtained on GaAsSb (113)B surface. (a) (b) and (c) : AFM surface profile of 3,4 and 5 ML InAs deposition on $\text{GaAs}_{0.51}\text{Sb}_{0.49}$ surface. The scanned areas are $1\ \mu\text{m} \times 1\ \mu\text{m}$. (d), (e) and (f): density, average height and average base diameter of the islands extracted from the AFM images. The error margins for AFM measurements represent the standard deviations of such statistics. The error margin for X-STM measurement in (e) marks the dimension of smallest and largest quantum dot observed.

Surface profiles of unburied InAs deposition were acquired using contact-mode AFM and the recorded AFM images are shown in figure 4.11a-4.11c. In contrast to the flat InAs surface obtained on InP (001) substrate (figure 4.7), InAs depositions on (113)B surface of GaAs_{0.51}Sb_{0.49} have led to the formation of abundant InAs islands. A ‘watershed’ algorithm was applied to these images to identify individual islands and to measure their dimensions³. Statistics on these islands are displayed in figure 4.11d-4.11f. Quantum dot density has reached as high as $1 \times 10^{11} \text{ cm}^{-2}$ by 5 ML InAs deposition, and yet no coalesced island was spotted. Similar high density of quantum dots without defective islands had been observed when Sb is present during the growth of InAs/GaAs (001) quantum dots [16, 18]. The AFM measured island height is constantly increasing from 1 nm to 4 nm as a function of InAs deposition, while their average diameters decrease from over 40 nm to about 30 nm. This is in contrast to the cases where InAs is deposited directly on (113)B surface of InP: the height of island would be independent of InAs deposition once fully developed quantum dots appear after 3 ML InAs were deposited [22]. It’s worth noting that, in figure 4.11a-4.11c, the quantum dots seem to be sitting on periodically fluctuating surfaces; this could arise from slight faceting of underlying GaAs_{0.51}Sb_{0.49} buffer layer via step bunching [23].

PL spectra of the PL samples were recorded at 15 K. Figure 4.12 gives an example of such PL spectra recorded from the 4 ML InAs/GaAsSb (113)B quantum dot sample and two types of PL peaks were detected for this samples. The 0.8 eV peaks are also observed in InAs/GaAsSb (001) samples so that they are attributed to the band-gap of GaAs_{0.51}Sb_{0.49}. The other broad peak in the PL spectrum around 0.6-0.7 eV shift towards higher energies under increasing excitation powers, and the peak maximum is a linear function of the cubic root of excitation power (figure 4.13a,page 89). Such power dependence is thus attributed type-II InAs quantum dots. It worth to be noted that this quantum dot related broad peak is even observed with the sample containing only one mono-layer of InAs deposition, which suggests that, the critical thickness for island formation *could* be even smaller than 1 ML.

Unlike InAs/GaAsSb (001) quantum wells, it is interesting that the GaAsSb emission peaks in InAs/GaAsSb quantum dot structure are broadening and shifting towards high energy under increasing excitation power. During the PL experiment, the photo-generated electrons are confined in InAs quantum dots while the holes are attracted around them. The InAs quantum dots have different shapes and sizes so that the electric field around them could be rather complex. At the same time, at low excitation power electrons tend to occupies larger quantum dots than smaller ones so that the distribution of carriers is also inhomogeneous. For these reasons, the GaAsSb recombination which occurs in the region close to InAs quantum dots is more likely to be influenced by the excitation power than in the case of InAs/GaAsSb quantum well.

³These procedures were performed with the help of software package ‘Gwyddion’

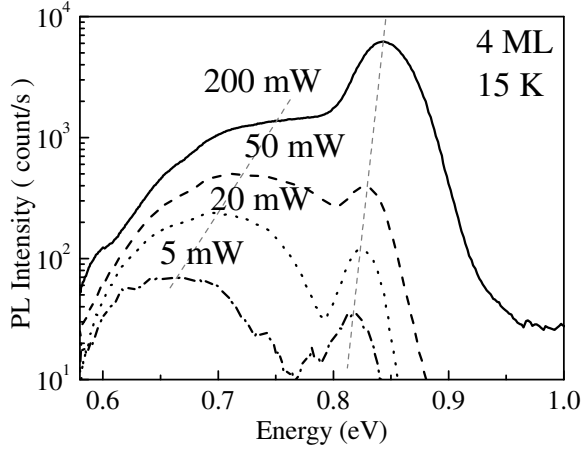


Figure 4.12: Low temperature PL spectra of 4 ML InAs/GaAs_{0.51}Sb_{0.49} quantum dot samples, under different PL excitation power. The maximum excitation power 200 mW correspond to a power density about 4 kW/cm².

Limited by the sensitivity of detector used in PL experiment, some PL peaks cannot be reliably extracted from PL spectra taken under small excitation power, which means the measured PL energies are higher than the actual fundamental transition energies associated with these quantum dots. Here, we estimate the fundamental transition energies of these InAs/GaAsSb quantum dots by extrapolating PL peak energies to zero excitation power. Figure 4.13a demonstrates extrapolation and it suggests that the measured fundamental transition energies could be over-estimated by 50 meV in certain cases. In figure 4.13b the extrapolated PL energies are compared with transition energies calculated for InAs/GaAsSb quantum wells (already presented in figure 4.4b). The PL energies follow a slightly slower slope than those calculated for quantum wells, albeit lateral carrier confinement in quantum dots is not taken into account in such calculations. This indicates that transition energies related to these quantum dots are largely determined by vertical confinement, namely their heights. The PL energies decrease by 22 meV in average for each additional mono-layer of InAs deposited thus they reflect the monotonously increasing height of the InAs/GaAsSb quantum dots already observed by AFM. Such behaviors are radically different from a previous observation obtained of our laboratory, where the height of InAs/InP (113)B quantum dot saturated at 3 ML InAs deposition [22] and their emission energies is limited by its height. The possibility of making large InAs/GaAsSb quantum dots makes this material system potentially useful for mid-wave wavelength applications on InP substrate. At the same time, this suggests that different island formation mechanism could have occurred under the presence of Sb.

We performed microscopic structural characterization of encapsulated quantum dots using X-STM. Figure 4.14 presents large scale X-STM images showing quantum dots formed by 3 and 4 ML InAs depositions. High quality cleaved surfaces were not achieved for zones containing the 5 ML and 6 ML quantum dot planes, probably due to the high

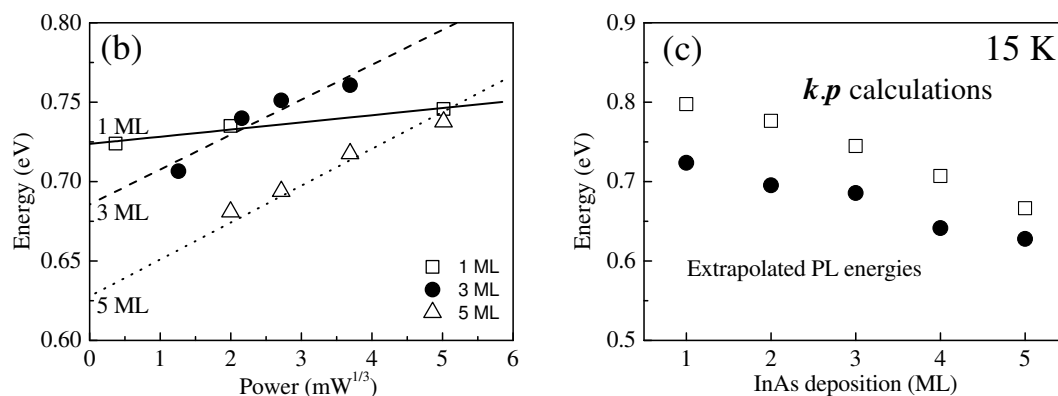


Figure 4.13: (a) Excitation-power dependent PL peak energies of quantum dot related emission. The line segments are linear fit of experimental data. (b) Calculated fundamental transition energy compared with ‘zero-excitation’ PL energy, which are y -intercepts of the line segments presented in (a).

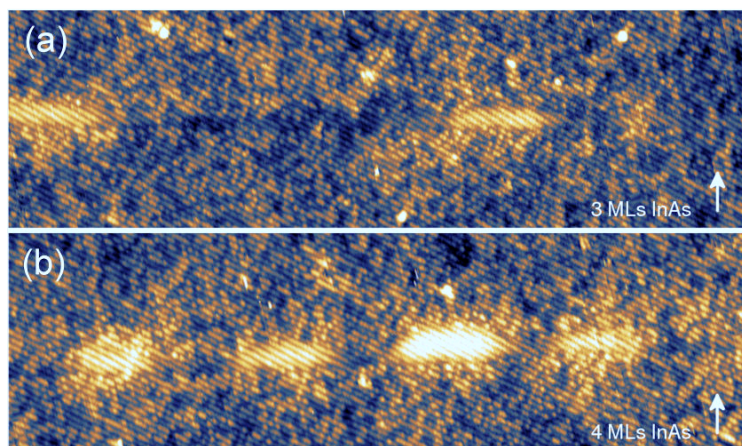


Figure 4.14: X-STM images of buried InAs/GaAsSb (113)B quantum dots obtained by (a) 3 ML and (b) 4 ML InAs deposition. Sample bias of -3.2 V was used and the presented area is $81 \times 24 \text{ nm}^2$.

level of strain. The images were taken under constant current mode with large negative sample bias (-3.2 V). Under such conditions, filled states of group V elements are imaged. The bright zones in the images correspond to indium-rich InAs QDs, while their surroundings with randomly distributed bright dots reflects GaAsSb layers with randomly distributed Sb atoms. The homogeneous contrast inside the quantum dots indicates that they are consisted of almost pure InAs without segregated Sb atoms.

The inter-islands distance in the 4 ML plane is almost 50% smaller than that in 3 ML plan. This is coherent with the sharply increasing island density observed by AFM. Besides, the inter-island spacing has become comparable to the diameter of AFM tip (20 nm) and it explains why the spaces between those islands presented in figure 4.11 were not resolved. In figure 4.11e, the average heights of encapsulated quantum dots

measured by X-STM image analysis are already compared with that of unburied quantum dots measured by AFM, and these values are actually close to each other. Also the height/length ratios of these Sb-mediated GaAs_{0.51}Sb_{0.49}-capped InAs quantum dots are also higher than InP-capped ones. Such results affirm a previous observation that using GaAs_{0.51}Sb_{0.49} as capping layer can avoid the dissolution of InAs quantum dots during encapsulation process (figure 4.3b) [8, 9].

However, by scrutinizing the region between quantum dots, it is also interesting that no wetting layer connecting the quantum dots was observed in either image of figure 4.14. As a matter of fact, the space between two islands, which is also the interface between GaAsSb matrix and GaAsSb capping layer, has even darker contrast than the inner part of GaAsSb. This could be a consequence of Sb depletion during the deposition of InAs. For many quantum dot systems like InAs/GaAs (001) [24, 25], InAs/InP (001) [2], InAs/AlGaInAs (113)B [26] and InAs/InP (113)B [9, 27], InAs islands are formed under Stranski-Krastanow growth mode. Their wetting layer accompanying the formation of InAs islands can be observed by various techniques including X-STM (for example figure 4.3a-4.3a). Combining the fact that no wetting layer related PL emission was detected for these InAs/GaAsSb (113)B quantum dots, we conclude that they were actually formed under Volmer-Weber growth mode. To our knowledge, InAs quantum dots formed under Volmer-Webber growth mode is rare on InP substrate.

Summary

In this section, we have walked through a comparison between InAs/GaAs_{0.51}Sb_{0.49} heterostructures grown on (001) and (113)B-oriented InP substrate. On InP (001) substrate, the InAs deposition remains as two-dimensional layer, where the formation of large InAs island is expected for as much as 5 ML InAs deposition. The annihilation of quantum dots thus agree with the normal surfactant effect of Sb, which is employed in the growth of strained quantum well in chapter 3. And the segregating Sb originated from GaAs_{0.51}Sb_{0.49} surface is thus responsible for the altered growth mode.

On the other hand, when the same material is grown on (113)B substrate, the high-density of quantum dots are formed for any InAs thickness deposited. Moreover, unusual for InAs quantum dots obtained on InP substrates, no wetting layer was observed by neither optical study nor by direct STM observation so that these quantum dots are actually formed under Volmer-Weber growth mode. Such results suggest that the surfactant effect enhances the three-dimension growth mode of InAs instead of suppressing it on InP (113)B substrate. Why Sb as a surfactant has behaved differently on (113)B-oriented substrate is thus left as a question to be answered in the coming section.

4.3 Surface-orientation dependent surfactant effect of Sb

Surfactant effect in epitaxial growth is frequently interpreted as its influence on surface mass transport. They are considered to either globally reduce the diffusion length of cation ad-atoms [28–32] or to create higher barrier for ad-atoms trying to climb surface steps [33, 34], so that the migration of ad-atoms towards island is kinetically blocked.

Such kinetic argument allows a direct explanation to the flat InAs/GaAs_{0.51}Sb_{0.49} layers obtained on (001) InP substrates. Nevertheless, it cannot explain the Volmer-Weber quantum dots grown on GaAs_{0.51}Sb_{0.49} (113)B substrate. For one thing, the formation of high density InAs islands indicates that sufficient mass transport had occurred despite the presence of Sb. For another, the existence of wetting layer in Stranski-Krastanow growth mode is widely accepted as a result of the energetic balance between strain relaxation / facet creation accompanying the island formation and its thickness is supposed to be constant overtime. Therefore, no direct connection can be established between growth kinetics and the absence of InAs wetting layer.

On the other hand, the surfactant effect can also be explained by its capability of the surface energy modification [35–37]. Surfactant elements like Sb tend to segregate and stay on the growth surface; it can saturate dangling bonds on the surface, form dimers structures between themselves, alter the surface reconstruction and reduce the free energy of the growth surface [38]. Figure 4.15 illustrates several possible configuration of InAs deposition on (001) and (113)B surfaces of GaAs_{0.51}Sb_{0.49} buffer layer, along with energy terms governing the choice of growth mode. They are the strain energy (density) ε_{2D}^{WL} , surface energy (density) of Sb-covered InAs wetting layer $\gamma_{InAs:Sb}^{WL}$, the strain energy (density) stored in partially relaxed InAs island ε_{3D}^{QD} , surface energy of its Sb-covered facets $\gamma_{InAs:Sb}^{\square}$ and the interface energy due to wetting layer coverage on the substrate $\gamma_{InAs-GaAsSb}^{\diamond}$. The InAs/GaAs_{0.51}Sb_{0.49} system will choose the configuration with lowest total energy as its equilibrium shape.

In contrast to Stranski-Krastanow InAs quantum dots formed by less than 3 ML of InAs deposition in Sb-free growth on InP substrate, InAs deposition on Sb-rich GaAs_{0.51}Sb_{0.49} (001) surface undergoes two-dimensional growth mode (figure 4.15a) even if as much as 5 ML of InAs has been deposited. This requires the surface energy of InAs (001) wetting layer $\gamma_{InAs:Sb}^{(001)}$ be low enough to compensate the need for strain relaxation. This requirement can be satisfied by the presence of Sb during the growth, where it stabilizes the surface of InAs surface by reducing its surface energy ($\gamma_{InAs:Sb}^{\square} < \gamma_{InAs}^{\square}$). However, we have to point out that surface energy reduction regardless surface orientation does not help maintain two-dimensional growth mode. In fact, by globally reducing the free energy of InAs surface, the side facets of quantum dots are also stabilized (i.e. $\gamma_{InAs:Sb}^{\{114\}} < \gamma_{InAs}^{\{114\}}$ on (001) substrate in figure 4.15b), so that it would become easier to create InAs islands.

Tersoff *et al.* have pointed out that in order to stabilize two-dimensional growth mode, the surfactant has to reduce the surface energy of its wetting layer (top facet)

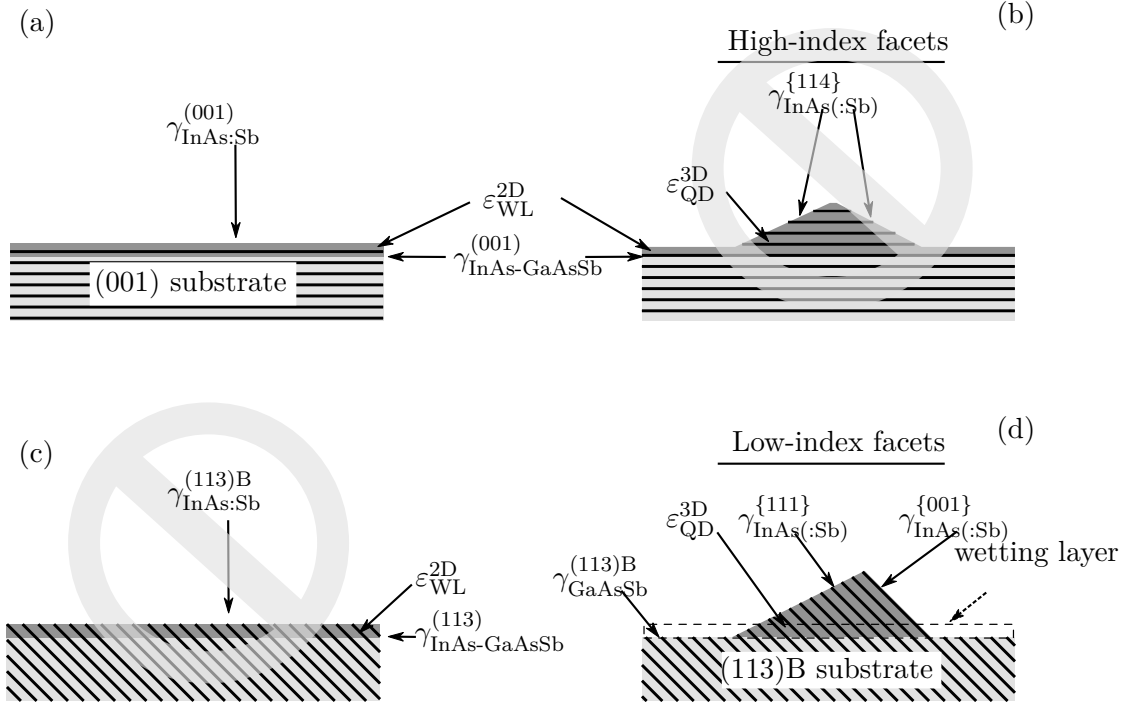


Figure 4.15: Schematic representation of several possible outcome of InAs deposition on (100) and (113) substrate: (a) two-dimensional growth mode on (001) substrate, (b) Stranski--Krastanow growth mode on (001) substrate; (c) two dimensional growth mode on (113) substrate; (d) Volmer-Weber growth mode on (113) substrate.

more than the side facets (edges) of islands [35]. For InAs deposition on (001) surface of $\text{GaAs}_{0.51}\text{Sb}_{0.49}$, this criterion can be met if we assume the presence of Sb stabilize the low-index (001) surface wetting layer while it does not stabilize islands' high-index $\{114\}$ facets to the same extent ($\gamma_{\text{InAs:Sb}}^{(001)} < \gamma_{\text{InAs}}^{(001)}$ while $\gamma_{\text{InAs:Sb}}^{(114)} > \gamma_{\text{InAs}}^{(114)}$). In other words, surface energy modification of surfactant is actually anisotropic.

The hypothesis of surface-orientation dependent surface energy modification also allows concise explanation to why InAs/GaAsSb (113)B quantum dots are formed under Volmer-Weber growth mode. As has been pointed in section 4.1, InAs islands formed on InP (113)B substrate are found to be composed of low-index facets in $\{001\}$, $\{110\}$ and $\{111\}$ families. At the same time, the surface of InAs wetting layer, if it exists, would be (113)-orientated. Therefore, on (113) substrate, when the presence of Sb reduces the free energy of low-index surfaces like (001) while increases that for high-index surfaces like (113), it actually enhances the formation of quantum dots while destabilizes InAs wetting layer, or even eliminates it.

Similar surface-orientation dependent surfactant-induced surface energy modification has already been observed experimentally in other material system. Through the observation of equilibrium shape of Ge/Si island under the influence of Sb, Eaglesham

et al. have concluded that the presence of Sb increases surface energy of 113 facets of Ge islands as compared to the (001) top facets (plateau) [39]. In the lateral MOCVD growth of GaN, Zhang *et al.* have demonstrated that the use of Sb favors the growth of certain facets so that the shape of micrometric GaN ridges is altered [40].

Thus we have proposed anisotropic surfactant effect as an explanation to the different shapes of InAs/GaAs_{0.51}Sb_{0.49} nanostructure observed on (001) and (113)B substrate.

A weakness of the above argument on equilibrium shape is the omission of strain. As is discussed in section 1.3 (page 11), lattice-mismatch and strain energy is essential to the formation of coherent islands and it is a challenge to actually compare the magnitude of strain energy and surfactant induced surface energy change, both theoretically and experimentally.

Conclusion

In this chapter, we have studied surfactant effect of Sb through the comparison of InAs/-GaAs_{0.51}Sb_{0.49} nanostructures grown on InP (001) and (113)B substrates. It is intriguing that quantum wells were obtained on (001) substrates, but quantum dots of high-density were achieved on (113) substrates. We attribute such phenomena to the anisotropic surface energy modification due to the presence of Sb: on (001) substrate Sb stabilize (001) oriented InAs wetting layer so that flat InAs layers were achieved; on (113)B substrate it enhances the faceting of InAs deposition and destabilize (113)B oriented InAs wetting layer so that quantum dots are formed under Volmer-Weber growth mode. By only 5 ML of InAs deposition, the emission wavelength of such type-II quantum dots is already close to 2 μm and mid-infrared emission is expected for higher InAs deposition quantity, which is to be studied in future works.

References

- [1] H. Li et al., “Ordered InAs quantum dots in InAlAs matrix on (001) InP substrates grown by molecular beam epitaxy”, *Applied Physics Letters* **72**, 2123–2125 (1998).
- [2] A. Ponchet et al., “Relationship between self-organization and size of InAs islands on InP(001) grown by gas-source molecular beam epitaxy”, *Applied Physics Letters* **67**, 1850–1852 (1995).
- [3] A. Ponchet et al., “Stability of (114) and (114) facets in III–V compounds under usual MBE conditions”, *Microelectronics Journal* **26**, 783–788 (1995).
- [4] H. R. Gutiérrez et al., “Faceting evolution during self-assembling of InAs/InP quantum wires”, *Applied Physics Letters* **79**, 3854–3856 (2001).
- [5] P. Caroff et al., “Critical thickness for InAs quantum dot formation on (311)B InP substrates”, *Journal of Crystal Growth* **311**, 2626–2629 (2009).
- [6] S. Fréchengues et al., “Wavelength tuning of InAs quantum dots grown on (311)B InP”, *Applied Physics Letters* **74**, 3356–3358 (1999).
- [7] C. Cornet et al., “Single InAs quantum dots morphology and local electronic properties on (113)B InP substrate”, in *Euro-MBE* (Mar. 2011).

-
- [8] G. Costantini et al., “Interplay between thermodynamics and kinetics in the capping of InAs/GaAs(001) quantum dots”, *Physical Review Letters* **96**, 226106 (2006).
- [9] W. Lu et al., “Shape and size control of InAs/InP (113)B quantum dots by sb deposition during the capping procedure”, *Nanotechnology* **22**, 055703 (2011).
- [10] J. M. Ulloa et al., “Effect of a lattice-matched GaAsSb capping layer on the structural properties of InAs/InGaAs/InP quantum dots”, *Journal of Applied Physics* **107**, 074309 (2010).
- [11] C. Çelebi et al., “Capping of InAs quantum dots grown on (311)B InP studied by cross-sectional scanning tunneling microscopy”, *Applied Physics Letters* **89**, 023119 (2006).
- [12] Y. I. Mazur et al., “Coexistence of type-I and type-II band alignments in antimony-incorporated InAsSb quantum dot nanostructures”, *Applied Physics Letters* **100**, pages (2012).
- [13] T. Matsuura et al., “PL characteristics of InAs quantum dots with sb irradiation in growth interruption”, *Journal of Crystal Growth* **278**, 51–56 (2005).
- [14] Y. Osaka et al., “Wideband luminescence of high-density InAs quantum dots on GaAsSb/GaAs layers”, *Journal of Crystal Growth* **10**. 1016/j.jcrysgro.2012.12.042.
- [15] N. Kakuda et al., “Sb-mediated growth of high-density InAs quantum dots and GaAsSb embedding growth by MBE”, *Applied Surface Science* **254**, 8050–8053 (2008).
- [16] D. Guimard et al., “High density InAs/GaAs quantum dots with enhanced photoluminescence intensity using antimony surfactant-mediated metal organic chemical vapor deposition”, *Applied Physics Letters* **89**, pages (2006).
- [17] P. Aivaliotis et al., “Enhancing the dot density in quantum dot infrared photodetectors via the incorporation of antimony”, *Applied Physics Letters* **91**, pages (2007).
- [18] K. Yamaguchi and T. Kanto, “Self-assembled InAs quantum dots on GaSb/GaAs(0 0 1) layers by molecular beam epitaxy”, *Journal of Crystal Growth* **275**, e2269–e2273 (2005).
- [19] J. Harmand et al., “Molecular beam epitaxy of AlGaAsSb system for 1.55 μ m bragg mirrors”, *Journal of Crystal Growth* **175–176, Part 1**, 372–376 (1997).
- [20] C. Renard et al., “Molecular beam epitaxy of (Ga,Al)AsSb alloys on InP(0 0 1) substrates”, *Journal of Crystal Growth* **278**, 193–197 (2005).
- [21] O. Ostinelli et al., “Photoluminescence and band offset of type-II AlGaAsSb/InP heterostructures”, *Semiconductor Science and Technology* **21**, 681–685 (2006).
- [22] S. Fréchengues et al., “Monolayer coverage effects on size and ordering of self-organized InAs islands grown on (1 1 3)B InP substrates”, *Journal of Crystal Growth* **209**, 661–665 (2000).
- [23] R. Nötzel et al., “Tunability of one-dimensional self-faceting on GaAs (311)A surfaces by metalorganic vapor-phase epitaxy”, *Applied Physics Letters* **64**, 3557–3559 (1994).
- [24] P. Offermans et al., “Formation of InAs wetting layers studied by cross-sectional scanning tunneling microscopy”, *Applied Physics Letters* **87**, pages (2005).
- [25] E. Luna et al., “Quantitative study of the interfacial intermixing and segregation effects across the wetting layer of ga(As,Sb)-capped InAs quantum dots”, *Applied Physics Letters* **101**, pages (2012).
- [26] I. Alghoraibi et al., “Self-assembled InAs quantum dots grown on InP (3 1 1)B substrates: role of buffer layer and amount of InAs deposited”, *Journal of Crystal Growth* **293**, 263–268 (2006).
- [27] M. Bozkurt et al., “An atomic scale study on the effect of sb during capping of MBE grown III–V semiconductor QDs”, *Semiconductor Science and Technology* **26**, 064007 (2011).
- [28] R. M. Tromp and M. C. Reuter, “Local dimer exchange in surfactant-mediated epitaxial growth”, *Physical Review Letters* **68**, 954–957 (1992).
- [29] J. Massies and N. Grandjean, “Surfactant effect on the surface diffusion length in epitaxial growth”, *Physical Review B* **48**, 8502–8505 (1993).
- [30] C. W. Snyder and B. G. Orr, “Comment on “Delayed relaxation by surfactant action in highly strained III–V semiconductor epitaxial layers””, *Physical Review Letters* **70**, 1030–1030 (1993).

- [31] B. Voigtländer et al., “Modification of growth kinetics in surfactant-mediated epitaxy”, *Physical Review B* **51**, 7583–7591 (1995).
- [32] E. Tournié et al., “Surfactant-mediated molecular-beam epitaxy of III–V strained-layer heterostructures”, *Journal of Crystal Growth* **150**, Part 1, 460–466 (1995).
- [33] D. Kandel and E. Kaxiras, “The surfactant effect in semiconductor thin-film growth”, *Solid State Physics Volume* **54**, 219–262 (1999).
- [34] I. Markov, “Kinetics of surfactant-mediated epitaxial growth”, *Physical Review B* **50**, 11271–11274 (1994).
- [35] J. Tersoff and F. K. LeGoues, “Competing relaxation mechanisms in strained layers”, *Physical Review Letters* **72**, 3570–3573 (1994).
- [36] R. Kern and P. Müller, “Three-dimensional towards two-dimensional coherent epitaxy initiated by surfactants”, *Journal of Crystal Growth* **146**, 193–197 (1995).
- [37] M. Copel et al., “Surfactants in epitaxial growth”, *Physical Review Letters* **63**, 632–635 (1989).
- [38] J. Chi and A. Katkov, in *Molecular beam epitaxy* (Elsevier, Oxford, 2013), pp. 189–202.
- [39] D. J. Eaglesham et al., “Growth morphology and the equilibrium shape: the role of “surfactants” in Ge/Si island formation”, *Physical review letters* **70**, 966–969 (1993).
- [40] L. Zhang et al., “The addition of sb as a surfactant to GaN growth by metal organic vapor phase epitaxy”, *Journal of Applied Physics* **92**, 2304–2309 (2002).

Chapter 5

Incorporation of Sb in Strained InAs(Sb) Heterostructures

In previous chapters, we have demonstrated how the use of Sb can modify the growth behavior of InAs nanostructures via their surfaces . It is also important to know to what extent Sb incorporates into InAs nanostructures under strain. However, the determination of Sb-concentration at nano-scale is rather tricky and it has become one of the goals of the ANR project NAIADE.

In this final chapter, we will present a preliminary investigation on the incorporation of Sb in strained InAs layer. Using thermodynamic calculations, section 5.1 seek for the right growth condition that can lead to significant Sb-incorporation in strained InAs layer. And the following section 5.2 attempts to assess the concentration of Sb in InAs(Sb)/Al_{0.48}In_{0.52}As nanostructures through optical studies.

5.1 Thermodynamics of Sb-incorporation in strained InAs

The MBE growth of ternary alloys like $\text{InAs}_{1-x}\text{Sb}_x$ is thermodynamically equivalent to the sequence of processes described in figure 5.1¹.

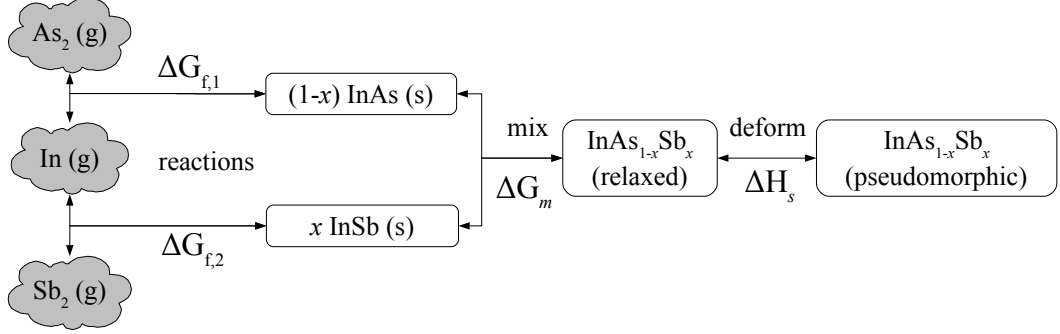


Figure 5.1: Thermodynamics descriptions of the growth of pseudomorphic $\text{InAs}_{1-x}\text{Sb}_x$ layer on InP substrate.

At first, the molecules in gas phase react and generate their corresponding solid compounds InAs and InSb. By forming chemical bonds, the total free energy of the system is reduced by $\Delta G_{f,1}$ and $\Delta G_{f,2}$ respectively, of which the magnitude is the order of 200 kJ/mol: this becomes the main driving force for MBE growth. Then x part of InAs mixes with $(1-x)$ part of InSb binary compounds to form relaxed ternary alloy $\text{InAs}_{1-x}\text{Sb}_x$, and the total energy of system further decreases by ΔG_m . If the $\text{InAs}_{1-x}\text{Sb}_x$ epi-layer is coherent with its substrate, the relaxed $\text{InAs}_{1-x}\text{Sb}_x$ alloy then undergoes tetragonal strain to have the same in-plane lattice constant as the substrate, with associated strain energy $\Delta H_s(x)$ [1]. Provided the input molecular beam pressure (P_{In}^0 , $P_{\text{As}_2}^0$, $P_{\text{Sb}_2}^0$) and fixed growth temperature (T) are known, the Sb composition of $\text{InAs}_{1-x}\text{Sb}_x$ alloy under growth is equivalent to an x that satisfies thermodynamic equilibrium between material in gas phase and solid phase. In order to make the main text clear, the lengthy description and solution process to this thermodynamic problem is left in appendix A.2 (page 120). In the following text, we solely present calculations obtained for the growth of strained $\text{InAs}_{1-x}\text{Sb}_x$ layer on InP substrate under 450 °C.

Figure 5.2 reports calculated compositions of relaxed InAsSb alloy under various growth conditions, where the deformation energy $H_s(x)$ is ignored. This scenario corresponds to the growth of thick and relaxed InAsSb layer, where no macroscopic strain is implicated. For InAsSb layers prepared under beam pressure ratio between group-V and group-III elements greater than unity, the Sb composition x is much lower than Sb-content in gas phase $P_{\text{Sb}_2}/(P_{\text{As}_2} + P_{\text{Sb}_2})$. The relation between the two quantities is

¹The object of these sequence of reactions is only to estimate the chemical potential change of each species. The reactions listed here do not necessarily correspond to what occurs in actual MBE growth, e.g. the gas phase reactions.

a rather nonlinear function, which could make composition calibration of such alloy difficult. The free energy change associated with InSb generation is $\Delta G_{f,2} = -237$ kJ/mol, while that for InAs is $\Delta G_{f,1} = -241$ kJ/mol. The relative small magnitude of InSb's formation energy is thus the origin of the disadvantageous Sb-incorporation in solid phase. Alternatively, efficient Sb-incorporation can be achieved at sufficiently low V/III ratio. It also makes the correspondence between x and $P_{\text{Sb}_2}/(P_{\text{As}_2} + P_{\text{Sb}_2})$ quasi-linear and facilitates alloy composition calibrations.

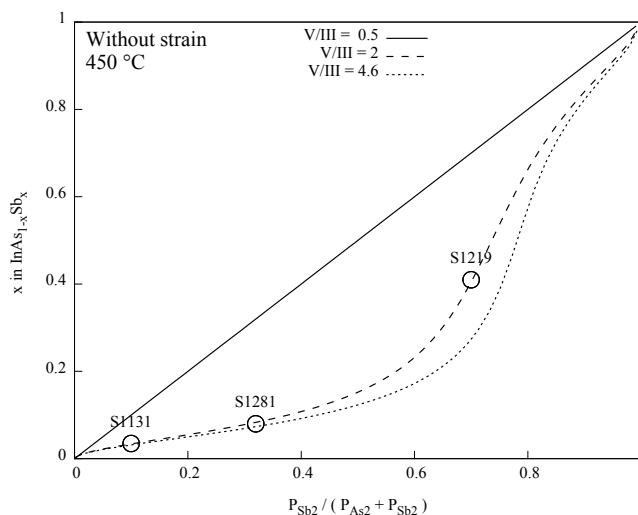


Figure 5.2: Thermodynamic calculations on the composition of relaxed $\text{InAs}_{1-x}\text{Sb}_x$ under various growth conditions.

The lattice constant of InSb and InAs are respectively 10.4% and 3% larger than their substrates InP. Therefore, strain energy stored in pseudomorphic InSb layer could be as high as 44 kJ/mol in contrast to 5 kJ/mol for pseudomorphic InAs layer on InP substrate. The high level of compressive stress induced by the addition of InSb in $\text{InAs}_{1-x}\text{Sb}_x$ layer will make the epitaxial layer further ‘repel’ the incorporation of Sb atoms.

Figure 5.3 presents calculation similar to those presented above but with coherency strain taken into account, so that such calculations correspond to scenario where $\text{InAs}_{1-x}\text{Sb}_x$ layer is grown on InP substrate. At sufficiently low V/III ratio close to 0.5, one can always achieve good Sb incorporation. However, when the epitaxial layer is grown under V/III ratio greater than unity, the incorporation of Sb is only possible by sending beam fluxes containing Sb concentration higher than a threshold value. This threshold actually corresponds to the point where all the As_2 in gas phase is consumed by impinging indium atoms. Such calculated low Sb-incorporation level agrees well with a previous observation on Sb-mediated InAs layer on InP (001) substrate, where TEM analyses did not give signs of significant Sb incorporation in InAs [2].

Although the above results are generally not in favor of the incorporation of Sb in

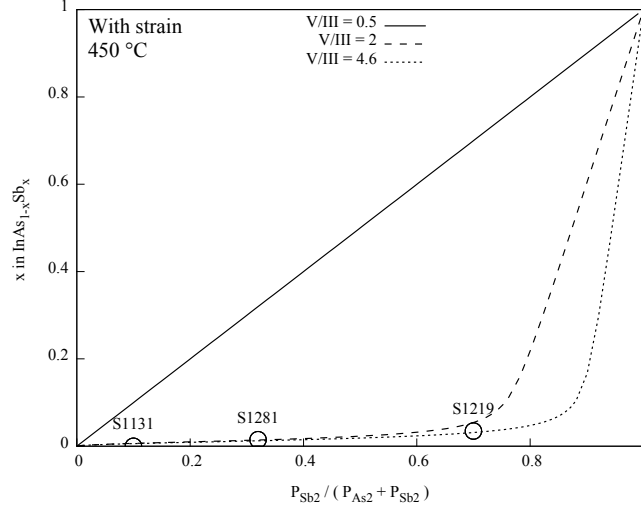


Figure 5.3: Calculated composition of strained $\text{InAs}_{1-x}\text{Sb}_x/\text{InP}$ layer, where the coherency strain is taken into account.

strained InAs layer, it does give some idea on how to increase its incorporation level. For one thing, the comparison between the calculations with and without strain indicate Sb-incorporation would be easier in partially relaxed nanostructures like quantum dot. For another, it would be beneficial to grow $\text{InAs}_{1-x}\text{Sb}_x$ layer under low V/III ratio or high indium growth rate if Sb-incorporation is desired.

In the practice of solid source MBE growth, the intensity of each beam flux is expressed in beam equivalent pressure, which is actually the reading of flux gauge. Current response of such gauges varies for different gas molecules so that beam equivalent ratios could be different from the gas pressure described in the thermodynamic calculations. To correlate the calculations with MBE growth, one has to convert the beam equivalent pressure into gas pressure P_i using :

$$P_i = \text{BEP}_i \cdot T_i^{\text{gas}} / \eta_i \quad (5.1)$$

$$\eta_i = 0.4Z_i/14 + 0.6 \quad (5.2)$$

For each impinging molecular beam i , T_i^{gas} is the temperature of the molecular beam, which is associated with the kinetic energy of its directional motion. And η_i is the ionization efficiency of the molecule, which corresponds to the chance of a molecule being ionized and detected in a Bayard-Alpert vacuum gauge. This quantity is in turn (empirically) estimated by the number of electrons a molecule contains Z_i .

5.2 Sb-incorporation in InAs/Al_{0.48}In_{0.52}As quantum wells

Although there were various demonstrations of how Sb composition in level in InAs deposition can be determined using optical studies [3, 4], the conclusions of such analyses are disputable. For one thing, the use of Sb can extend the PL emitting wavelength in two ways: Sb can get incorporated into InAs thus lowers its band gap; at the same time it can protect InAs nanostructures from being dissolved during the capping process [5, 6]. Both mechanisms would lead to observation of red-shifted PL energy. For another, it is known that the dimensions of a quantum dot have great influence on its optical properties, as we have shown in chapter 4. However, the input structures for the calculations of transition energies are often based on AFM observations of uncapped nanostructures [3, 4], which do not necessarily correspond to those of capped QDs [6, 7]. Therefore, in order to estimate Sb-incorporation level in InAs deposition using optical studies, one has to ensure the planarity of InAs deposition.

Therefore, we choose to study Sb incorporation in the growth of strained InAs(Sb)/Al_{0.48}In_{0.52}As quantum well using PL characterizations. For one thing, under the growth temperature 450 °C, the mobility of Al ad-atoms is relatively low on the growth surface. Under such conditions, the deposition is conform so that if InAs islands are formed during the deposition of InAs(Sb), its outline will be carried on to the final surface of Al_{0.48}In_{0.52}As capping layer. For another, the Al_{0.48}In_{0.52}As layer itself is lattice-matched to InP and it is routinely grown in the laboratory. This alloy is also Sb free so that if any Sb gets incorporated in InAs layer, it can be attributed to Sb supplied during InAs co-deposition.

Figure 5.4a shows the band alignments of three InAs_{1-x}Sb_x/Al_{0.48}In_{0.52}As quantum wells with different Sb concentration. For Sb compositions x between 0 and 0.9, the heterostructure has type-I straddling band alignments. But it turns into type-II staggered line-up when the quantum well is almost composed of pure InSb and this can be easily identified using PL experiment under different excitation powers. To help correlate PL emission energy with Sb incorporation level, we have calculated fundamental transition energies in 5-7 ML-thick InAs_{1-x}Sb_x/Al_{0.48}In_{0.52}As quantum wells with Sb-composition x ranging from 0 to 1, and such results are plotted in figure 5.4b. In the region where $x < 0.8$, the curves in figure 5.4b are almost parallel with each other, separated by about 65 meV for each additional mono-layer of InAs added. At the same time these curves demonstrate constant slope, which indicate PL energy will decrease by 37 meV for each 10% Sb concentration enhancement.

Totally three InAs(Sb)/Al_{0.48}In_{0.52}As samples are compared in this study, for the different $P_{\text{Sb2}}/(P_{\text{As2}} + P_{\text{Sb2}})$ used in during their growth. Theses samples were all grown under 450° on n-type InP (001) substrate. At first, a sufficiently thick InP buffer was grown just following the deoxidation of InP surface to ensure the smoothness of the surface. After that a 50 nm-thick Al_{0.48}In_{0.52}As layer is deposited. Then, the As₂

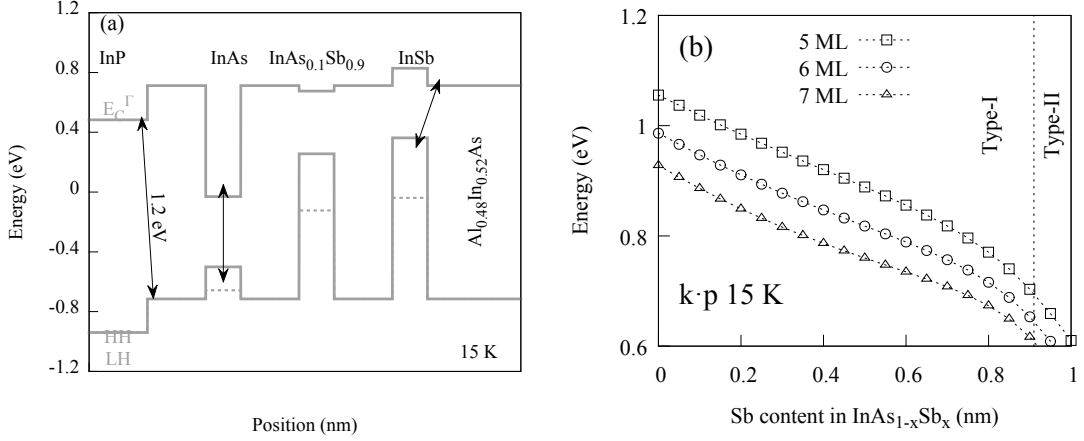


Figure 5.4: InAs_{1-x}Sb_x/Al_{0.48}In_{0.52}As quantum wells of various Sb composition. (a) band alignment $x = 0, 0.9$ and 1 . (b) Calculated fundamental transition energy of an InAs_{1-x}Sb_x/Al_{0.48}In_{0.52}As quantum well where x ranging from 0 to 1 .

Table 5.1: Growth parameters for InAs_{1-x}Sb_x/Al_{0.48}In_{0.52}As samples. Substrate temperature was fixed at 450°C . The “BEP”s are beam equivalent pressures, which correspond to flux gauge readings. The “pressures” are gas pressure converted using formulas (5.2)-(5.1)

	BEP As ₂ 10 ⁻⁷ Torr	BEP Sb ₂ 10 ⁻⁷ Torr	BEP In 10 ⁻⁷ Torr	Pressure Sb ₂ /(As ₂ +Sb ₂)	Pressure (As ₂ +Sb ₂)/In
S1131	18	3.4	1.7	0.12	4.6
S1281	7.5	6.3	1.7	0.38	2.6
S1219	2	8	1.7	0.74	1.5

and Sb₂ fluxes are adjusted to values given in table 5.1 using the action of valves. A 10 s growth interruption was performed to stabilization of the fluxes and 5 ML thick InAs is deposited at indium growth rate of 0.1 ML/s under both As₂ and Sb₂ flux. After that the fluxes are immediately switched back for the growth Al_{0.48}In_{0.52}As and a second 50 nm-thick Al_{0.48}In_{0.52}As layer is deposited. Unlike AlAs_{0.56}Sb_{0.44}, Al_{0.48}In_{0.52}As does not require protection against oxidation in atmosphere so that the sample temperature is down after the growth of this layer. The growth conditions for these samples are also marked by circles in figure 5.2 and 5.3 (page 100) to estimate the level of Sb-incorporation.

Figure 5.5 shows PL spectra of all the three samples recorded under 15 K. The emission peaks general red-shift when higher Sb flux is used, which is also accompanied by abrupt decrease in PL intensity. PL spectra of these samples were also taken under different excitation power, and no power dependence of these PL peak was observed, signifying that all of these InAs_{1-x}Sb_x heterostructures are still of type-I and that their real Sb concentration is lower than 0.90. The line-widths of all these PL peaks are relatively narrow so that it is plausible that the InAs quantum well is formed instead

of InAs quantum dots. Under such assumption, the PL peak energies are compared with calculated transition energies (the 5 ML in figure 5.4b) in the inset of figure 5.5, in attempt to reveal its Sb concentration x in InAs $_{1-x}$ Sb $_x$ layer.

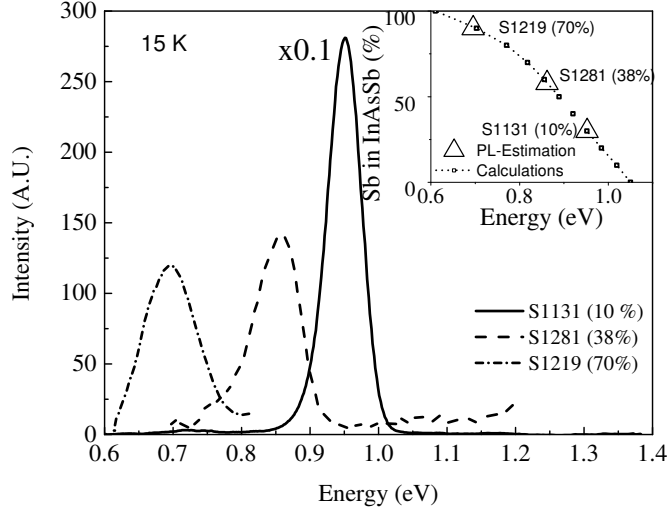


Figure 5.5: PL spectra of InAs(Sb)/Al $_{0.48}$ In $_{0.52}$ As samples. The PL Peak energy is compared with $k \cdot p$ calculations in the inset. Add temperature 15 K and cut the part superior than 1300 or 1250 (n type InP)

The PL peak of samples S1281(38%) is red-shifted by 94 meV as compared to sample S1131(10%). According to the $k \cdot p$ calculations presented in figure 5.4b, this could be related to either 25% higher Sb-incorporation or by +0.3 ML thickness fluctuation. The PL peak of samples S1219 is even red-shifted by 250 meV as compared to S1131(10%), which is equivalent to 70% more incorporated in InAs(Sb) quantum well, or 4 ML increase in quantum well thickness. For sample S1131, relative low Sb flux was used for during the deposition of InAs layer, thus the Sb-concentration in this samples can be considered as 0, which in turn implies a 70% Sb-concentration in samples S1219.

The concentration determination using PL is based on the fact that the InAs $_{1-x}$ Sb $_x$ /Al $_{0.48}$ In $_{0.52}$ As forms quantum well with small thickness fluctuations. Whether this assumption holds is yet to be examined by surface examinations. Figure 5.6 presents contact-mode AFM images of the three samples under study. For samples S1131 which is grown with relative high As $_2$ flux (As $_2$ 7×10^{-7} Torr) and low Sb $_2$ flux (10%), its surface is quite flat, which is marked by a small root-mean-square roughness of 0.2 nm. For samples S1281, of which Sb $_2$ flux accounts for more than 30% of group-V beam pressure, profiles of nano-object emerges and surface roughness is increased. Such observation suggest that nano structures like quantum dots or dashes may have formed during the deposition of InAs $_{1-x}$ Sb $_x$ layer. Such observation may thus invalidate the above composition determination based on PL study results. Further more, for samples S1219, a few deep pits is scattered on its surface, which may originate from defects due

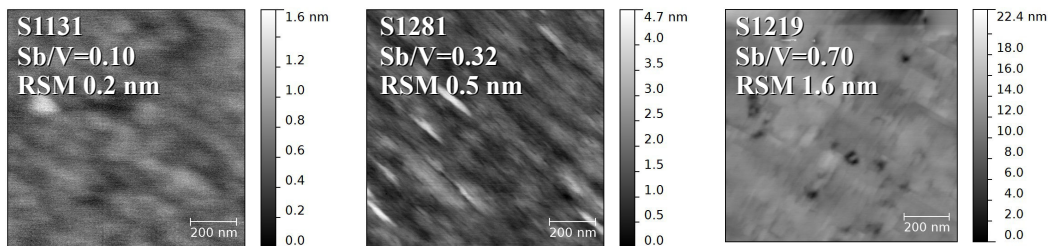


Figure 5.6: AFM surface examination of Al_{0.48}In_{0.52}As/InAs/Al_{0.48}In_{0.52}As samples.

to the formation of nanostructures. Therefore, it's no surprise that its PL intensity has decreased by a factor of 10 as compared to samples S1131.

Eventually, the fluctuated AlInAs final surface observed by AFM makes Sb-incorporation level deduced by PL studies less eloquent. Nevertheless, whether islands are formed or not in InAsSb layer and the chemical composition of these InAs(Sb) layers are yet to be determined by future microscopic studies.

Summary and perspectives

In this short chapter, we attempted to evaluate Sb-incorporation in strained InAs layer in two approaches. At first, Sb-incorporation is estimated by thermodynamics-based calculations. The calculations indicate significant part of Sb can be incorporated in relaxed InAs nanostructures; however, for fully strained InAs layer, the incorporation level of Sb is very low unless molecular beams with very high Sb₂ content is used, which is difficult for our current experimental setup. Alternatively, the calculations also indicate that the incorporation of Sb is more efficient when the InAsSb layer is deposited under low V/III ratio, which will be tested in future grow experiments.

We also performed growth experiments of InAs_{1-x}Sb_x/Al_{0.48}In_{0.52}As quantum wells under different Sb₂ flux and attempted to evaluate its Sb-incorporation level using optical studies. The low temperature PL data shows strong PL energy red-shift when high Sb flux is used during the growth. However, this cannot be attributed solely to Sb incorporation, since AFM studies indicate nanostructures may have formed and their larger vertical size may also have contributed to PL energy red-shift. We thus cannot determine the Sb composition using only optical studies and calculations. It is necessary to study these samples using microscopic chemical analyses in the coming future.

References

- [1] F. Turco et al., "Thermodynamic analysis of the molecular beam epitaxy of AlInAs alloys", *Journal of Crystal Growth* **88**, 282–290 (1988).

- [2] C. Gatel et al., “Analysis by high-resolution electron microscopy of elastic strain in thick InAs layers embedded in Ga_{0.47}In_{0.53}As buffers on InP(0 0 1) substrate”, *Acta Materialia* **58**, 3238–3246 (2010).
- [3] Y. I. Mazur et al., “Coexistence of type-I and type-II band alignments in antimony-incorporated InAsSb quantum dot nanostructures”, *Applied Physics Letters* **100**, pages (2012).
- [4] J. He et al., “Band alignment tailoring of InAs_{1-x}Sb_x/GaAs quantum dots: control of type I to type II transition”, *Nano Letters* **10**, 3052–3056 (2010).
- [5] M. Bozkurt et al., “An atomic scale study on the effect of Sb during capping of MBE grown III–V semiconductor QDs”, *Semiconductor Science and Technology* **26**, 064007 (2011).
- [6] W. Lu et al., “Shape and size control of InAs/InP (113)B quantum dots by Sb deposition during the capping procedure”, *Nanotechnology* **22**, 055703 (2011).
- [7] G. Costantini et al., “Interplay between thermodynamics and kinetics in the capping of InAs/GaAs(001) quantum dots”, *Physical Review Letters* **96**, 226106 (2006).

Conclusions

This thesis presents molecular beam epitaxy growth and characterizations of four Sb-based nanostructures on InP substrate.

Through the study of $\text{Ga}_{0.47}\text{In}_{0.53}\text{As}/\text{AlAs}_{0.56}\text{Sb}_{0.44}$ quantum wells presented in chapter 2, near-infrared inter-subband absorption was achieved. We have launched growth optimizations and microscopic studies in order to understand why the goal of $1.55\ \mu\text{m}$ inter-subband transition was not achieved. Microscopic observations of GaInAs/AlAsSb interfaces indicate that the homogeneity inside the alloy layers is not perfect and that as much as 1 ML of Sb can be unintentionally incorporated into subsequent GaInAs layer.

In chapter 3, we made an effort to achieve near-infrared inter-subband absorption using strained $\text{InAs}/\text{AlAs}_{0.56}\text{Sb}_{0.44}$ quantum wells. Under conventional growth conditions, deposition of InAs on InP (001) substrate would lead to the formation of three-dimensional nanostructures, but we have demonstrated that the growth of two-dimensional InAs layer is made possible by surfactant effect of Sb. Using Sb-mediated growth, we have achieved defect-free $\text{InAs}/\text{AlAs}_{0.56}\text{Sb}_{0.44}$ single quantum well as thick as 7 ML, which is required for the realization of $1.55\ \mu\text{m}$ inter-subband transition. By using AlAs layer for strain compensation, we were also able to achieve $\text{InAs}/\text{AlAs}_{0.56}\text{Sb}_{0.44}$ multiple quantum wells with zero net-strain. Eventually, we showed preliminary investigations on the inter-subband properties of these structures.

In chapter 4, the study of surfactant effect of Sb continues through the growth of type-II $\text{InAs}/\text{GaAs}_{0.51}\text{Sb}_{0.49}$ heterostructures. The growths of such structures on (001) and (113)B-oriented InP substrates have led to very different results: $\text{InAs}/\text{GaAs}_{0.51}\text{Sb}_{0.49}$ quantum wells were obtained on InP (001) substrate, while high-density $\text{InAs}/\text{GaAs}_{0.51}\text{Sb}_{0.49}$ quantum dots are formed under Volmer-Webber growth mode on InP (113)B substrates. We attribute such phenomena to the anisotropic surfactant effect of Sb. It stabilizes low-index surfaces and it increases the surface energy of high-index surfaces. On (001) substrate, Sb stabilizes (001)-oriented InAs wetting layer so that flat InAs layers were achieved, while on (113)B substrate it enhances the low-index facets of InAs island and destabilizes (113)B oriented InAs wetting layer so that InAs island are formed without wetting layer. By only 5 ML of InAs deposition, the emission wavelength of such type-II quantum dots is already close to $2\ \mu\text{m}$, which makes this material system attractive for mid-infrared applications in future studies.

The incorporation of Sb in InAs is an important issue concerning Sb-mediated growth. In the final chapter 5, we attempted to evaluate the incorporation of Sb in strained InAs layer in two approaches. At first, thermodynamics calculations indicate the Sb-incorporation in strain InAs layer is very difficult under normal growth conditions. Then Sb-incorporation in InAs(Sb)/Al_{0.48}In_{0.52}As quantum wells is experimentally studied by photoluminescence. The optical data seem to suggest that a significant portion of Sb is incorporated in this structure, but we do not conclude at this time for cautions: because three-dimensional nanostructures have formed during the deposition of InAs(Sb), the composition determination in these nanostructures requires further microscopic analyses.

Perspective

During this PhD thesis, we have developed technological processes and absorption measurement workbench for the study of near-infrared inter-subband absorption on InP. With these infrastructures, we were able to observe near-infrared inter-subband absorption for the first time in FOTON laboratory. However, the goal of producing a structure that shows inter-subband absorption at 1.55 μm telecommunication band is left unfulfilled, and the inter-subband properties of InAs/AlAs_{0.56}Sb_{0.44} multiple quantum wells are yet to be studied in extended wavelength range. We are actually working on new workbench for this purpose. For the study of surface-orientation dependent surfactant effect in InAs/GaAs_{0.51}Sb_{0.49} heterostructures, future theoretical studies would be helpful to rigorously compare the interplay between anisotropic surfactant effect and lattice strain.

Résumé

Croissance et caractérisation optique des matériaux à base d'antimoine sur substrat InP pour les télécommunications optiques

Le contexte d'études

Désormais, tous les continents habitables sont incorporés dans un réseau d'information unique. Des fibres optiques silice et des composants optoélectronique travaillant à $1,55 \mu\text{m}$ sont indispensables pour les télécommunications à très longue distance et en même temps à grande vitesse. Les composants de la filière InP sont connus dans ce domaine, pour leurs applications comme émetteur et photodiodes à cette longueur d'onde transmise dans un tel milieu avec la moindre perte.

Certains de ces composants de famille semi-conducteurs III-V sont souvent développés voire élaborés par épitaxie par jet moléculaire (également connu sous l'acronyme anglais MBE) sur un substrat InP monocristallin. Reconnu pour ses capacités de réaliser des interfaces d'hétérostructures propres et pour ses contrôles précis d'épaisseur à l'échelle de couche atomique, cette technologie est idéale pour la conception et même pour la fabrication des nouveaux composants optoélectroniques.

L'utilisation des matériaux à base d'antimoine dans la filière InP peut apporter des nouvelles applications de plusieurs façons. Des alliages antimoniures compatible avec substrat InP peuvent former plusieurs alignements de bande qui sont encore peu exploités. La figure R.1 présente l'alignement de bande entre plusieurs alliages ternaires antimoniure et arséniure. Un puits quantique $\text{Ga}_{0,47}\text{In}_{0,53}\text{As}/\text{AlAs}_{0,56}\text{Sb}_{0,44}$ disposent un potentiel de confinement d'électron aussi fort qu'il est possible de produire transition inter-sous-bandes à proche-infrarouge au sein d'une telle structure [1]; cela fait l'objet de l'objectif du chapitre 2 et 3. Cependant, des nanostructures $(\text{Ga})\text{InAs}/\text{GaAs}_{0,51}\text{Sb}_{0,49}$ forment une hétérojonction de type-II où les porteurs sont séparés par cette interface. Ce système de matériaux dispose d'une bande-interdite effective plus petite que celles de chacun des matériaux constituant cette hétérostructure; il est prometteur pour réaliser des applications à des longueurs d'ondes plus longues que $3 \mu\text{m}$ dans la filière InP [2–4].

Par ailleurs, l'antimoine élémentaire est aussi connu pour ses effets surfactant durant

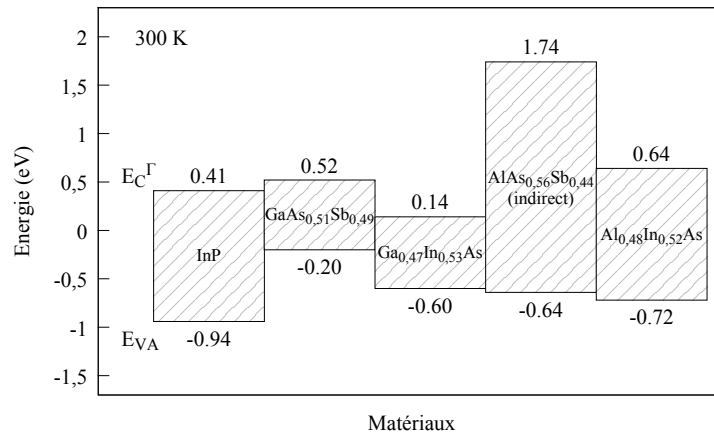


Fig. R.1 : Des matériaux en accord de maille avec InP et leurs alignements de bandes. Les données sont extraites de référence [5].

la croissance épitaxiale des composants désaccordés. D'une part, l'utilisation d'antimoine peut annihiler le mode de croissance 3D et rendre possible la croissance des couches contraintes sans défaut. Permettant ainsi l'introduction de nouvelles hétérostructures, son importance pour la technologie est évidente [6]. Nous proposons cet effet au travers d'études sur des puits quantiques InAs/AlAs_{0,56}Sb_{0,44} pour obtenir des transitions inter-sous-bandes à 1.55 μm dans le chapitre 3. De plus, il est aussi démontré dans certain cas que l'utilisation d'antimoine peut moduler la densité et les dimensions des nanostructures voire améliorer leurs propriétés optiques [7]. Dans le chapitre 4, les dépôts d'InAs ont été réalisés sur la surface de GaAs_{0,51}Sb_{0,49} de différentes orientations pour mieux comprendre l'effet surfactant de Sb.

Pour récapituler, ce travail de thèse porte sur la croissance et la caractérisation optique des nanostructures à base d'antimoine faites sur substrats InP. Elle est composée de quatre études :

- puits quantique Ga_{0,47}In_{0,53}As/AlAs_{0,56}Sb_{0,44} pour réaliser la transition inter-sous-bandes dans proche-infrarouge (chapitre 2, à partir de page 17)
- croissance de puits-quantiques InAs/AlAs_{0,56}Sb_{0,44} sous contrainte sur substrat InP, assistée par l'effet surfactant de Sb (chapitre 3, page 53)
- les différents rôles de l'effet surfactant d'antimoine sur la croissance des nanostructure InAs/GaAs_{0,51}Sb_{0,49} sur substrat InP de différents orientations cristallines (chapitre 4, page 75)
- l'efficacité d'incorporation de Sb dans une couche InAs contrainte (chapitre 5, page 97).

Puits quantiques $\text{Ga}_{0.47}\text{In}_{0.53}\text{As}/\text{AlAs}_{0.56}\text{Sb}_{0.44}$ en accord de maille pour des applications inter-sous-bandes à proche-infrarouge

La relaxation inter-sous-bandes est un processus qui permet de la modulation de signaux optiques ultrarapide, souvent dans l'ordre d'une picoseconde, il peut alimenter des futurs commutateurs du réseau optique [1, 8]. Disposant un offset de bande d'environ 1,6 eV et étant parfaitement en accord de maille avec substrat InP, le puits quantique $\text{Ga}_{0.47}\text{In}_{0.53}\text{As}/\text{AlAs}_{0.56}\text{Sb}_{0.44}$ est l'un des candidats pour réaliser des transitions inter-sous-bandes à 1,55 μm . (section 2.2, page 22)

Dans un premier temps, les paramètres structurels pour cet objectif ont été estimés par des calculs liaison-forte [9]. Affiché dans figure R.2b, ces résultats indiquent qu'il faut l'épaisseur de puits soit aussi fine que 7 monocouche (MC) (2,1 nm). Ensuite, plusieurs multi-puits $\text{Ga}_{0.47}\text{In}_{0.53}\text{As}/\text{AlAs}_{0.56}\text{Sb}_{0.44}$ ont été élaborés avec épaisseurs de puits aux alentours de cette valeur théorique. L'existence d'absorption inter-sous-bandes dans ces structures a été confirmée par son anisotropie (figure R.2a). Cependant les énergies (au pic) des transitions inter-sous-bandes ainsi que celles de transition inter-bandes de ces structures se trouvent plus bas au terme d'énergie que leurs valeurs théorique. De plus l'énergie du pic d'absorption inter-sous-bandes sature vers 0,65 eV (1,9 μm) pour un puits de 5 MC avec un élargissement toutefois notable à plus faible longueur d'onde. Ces résultats sont cohérents avec ceux obtenus par d'autre groupe de recherche et les écarts pourraient être à l'origine de plusieurs non-idéalités dans ces structures ou même lié au paramétrage des calculs. (Section 2.2 et 2.3)

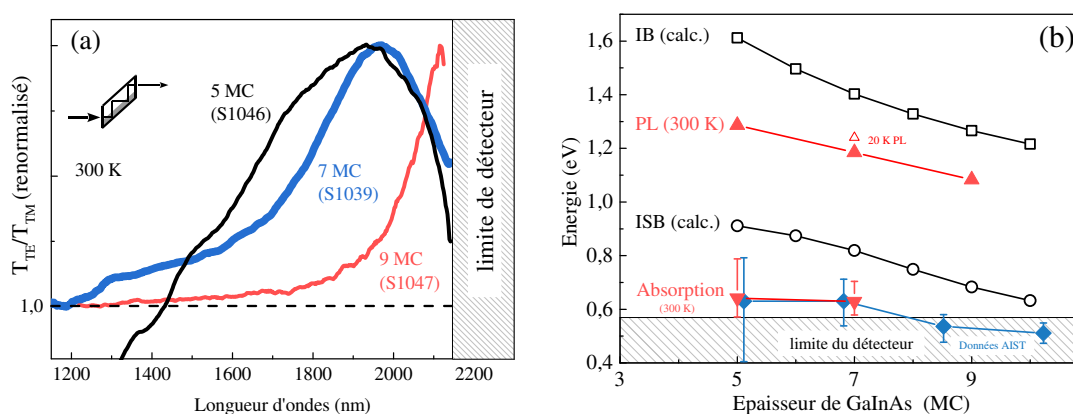


Fig. R.2 : (a) Spectre d'anisotropie d'absorption à l'origine de règle de sélection de transition inter-sous-bande; (b) énergies de transition inter-bandes et celles de transition inter-sous-bandes dans un puits $\text{Ga}_{0.47}\text{In}_{0.53}\text{As}/\text{AlAs}_{0.56}\text{Sb}_{0.44}$. Les valeurs expérimentales sont comparées avec celles estimées par les calculs 'liaison forte'. Les données "AIST" sont extraites de référence [10].

La qualité des interfaces $\text{Ga}_{0,47}\text{In}_{0,53}\text{As}/\text{AlAs}_{0,56}\text{Sb}_{0,44}$ a été examinée par microscopie électronique à effet tunnel (acronyme anglais STM) sur la face clivée. Il est constaté que les alliages $\text{Ga}_{0,47}\text{In}_{0,53}\text{As}$ et $\text{AlAs}_{0,56}\text{Sb}_{0,44}$ se sont mélangés à l'échelle atomique dans les zones d'interface. La distribution d'atomes d'antimoine est déduite de mesures STM et elle met en évidence la ségrégation d'antimoine de la couche d' $\text{AlAs}_{0,56}\text{Sb}_{0,44}$ vers celle de $\text{Ga}_{0,47}\text{In}_{0,53}\text{As}$ suivante. La quantité de Sb incorporée non-intentionnelle est environ 1 MC et elle est quasiment indépendante de traitement d'interface utilisé. (section 2.4, page 35)

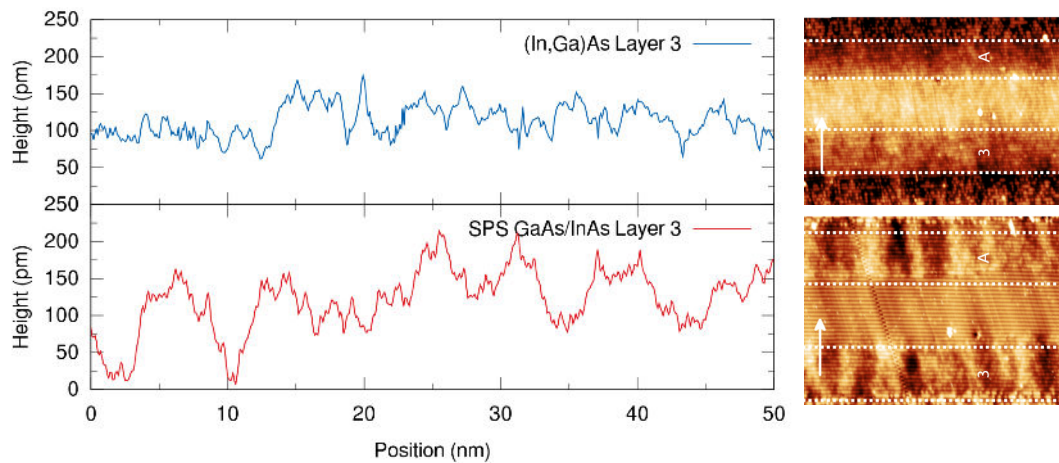


Fig. R.3 : Fluctuation dans l'alliage $\text{Ga}_{0,47}\text{In}_{0,53}\text{As}$ observée par microscope à effet tunnel. En haut : alliage conventionnel ; en bas, l'alliage $\text{Ga}_{0,47}\text{In}_{0,53}\text{As}$ est préparé sous mode d'épitaxie *digital alloy*

En tentant d'améliorer sa qualité, la technique « *digital alloy* » a été expérimentée sur cette structure. La pratique de ce mode d'épitaxie a considérablement amélioré les propriétés optiques en termes de rendement photoluminescence. Pourtant, elle aurait introduit de l'inhomogénéité importante dans l'alliage $\text{Ga}_{0,47}\text{In}_{0,53}\text{As}$, mise en évidence par les observations STM (figure R.3) ; la dégradation structurelle le rend inapte pour des applications éventuelles. (section 2.5, page 43)

La croissance de puits quantiques $\text{InAs}/\text{AlAs}_{0,56}\text{Sb}_{0,44}$ sous contrainte à l'aide de l'effet surfactant de Sb

Les puits quantiques $\text{InAs}/\text{AlAs}_{0,56}\text{Sb}_{0,44}$ sont potentiellement des objets de choix pour la réalisation de composants inter-sous-bandes travaillant à $1,55 \mu\text{m}$, puisqu'ils présentent un potentiel de confinement d'électron encore plus fort que dans le cas de $\text{Ga}_{0,47}\text{In}_{0,53}\text{As}/\text{AlAs}_{0,56}\text{Sb}_{0,44}$. Les calculs liaison-forte sur telles structures indiquent que la réalisation de transition inter-sous-bandes à $1,55 \mu\text{m}$ nécessite chaque période de puits

contiennent une couche d'InAs de l'épaisseur de 7 MC. (section 3.1, page 54)

L'enjeu associé à ce système réside dans la croissance de structures contraintes. Ayant un désaccord de maille de plus de 3%, il est attendu que le dépôt d'InAs sur un substrat InP bascule vers le mode de croissance 3D où des îlots InAs se sont formés au lieu d'une couche entière. Cependant, grâce à l'effet surfactant de Sb, nous avons pu obtenir des puits quantiques InAs/AlAs_{0,56}Sb_{0,44} contraints en fournissant un flux Sb pendant le dépôt d'InAs. Pourtant, il est constaté que cette technique ne fonctionne que pour le dépôt sur substrat InP dont la surface est orienté (001) mais pas pour celle orienté (113)B. (section 3.2, page 55)

La figure R.4 présente des images de microscope électronique à transmission (acronyme anglais TEM) de deux échantillons, chacun ne contient qu'une seule couche d'InAs. Ces observations indiquent que la relaxation plastique avait eu lieu pour l'échantillon contenant 12 MC d'InAs; pourtant l'autre structure de 7 MC d'InAs est exempte de défauts. La limite d'InAs pseudo-morphique a été déterminée à 8–10 MC par des études diffraction de rayons-X sur des structures supplémentaire, et les structures faites sous ce seuil disposent de bonnes propriétés optiques en terme de photoluminescence.

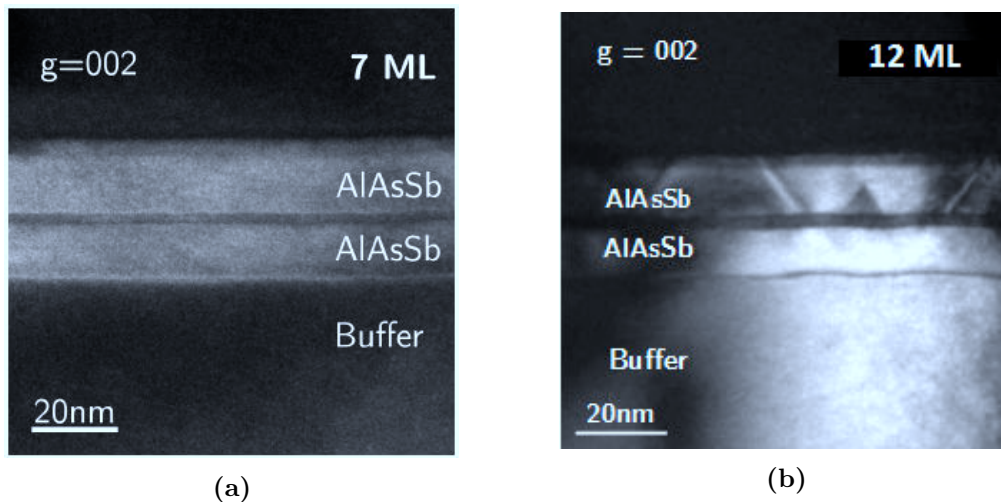


Fig. R.4 : Images TEM de InAs/AlAs_{0,56}Sb_{0,44}, vue par le tranche. L'épaisseur des couches InAs sont (a) 7 MC et (b) 12 MC.

Les énergies des transitions inter-bandes de ces structures ont été obtenues par photoluminescence à basse température; ses valeurs suivent la même tendance que celles simulées avec un décalage, comme il est illustré dans figure R.5. Ce décalage pourrait être attribué à l'interface riche en Sb, mis en évidence par des analyses géométrique de phase sur des résultats TEM de haute résolution. (section 3.3, page 58).

Pour fabriquer des multi-puits InAs/AlAs_{0,56}Sb_{0,44} destinés aux études optiques, il est nécessaire d'éviter que contrainte provenant du dépôt d'InAs s'accumule et vienne dégrader la qualité de l'ensemble de la structure. La symétrisation de la contrainte a été obtenue par l'insertion de couches nanométriques d'AlAs dans les barrières AlAs_{0,56}-

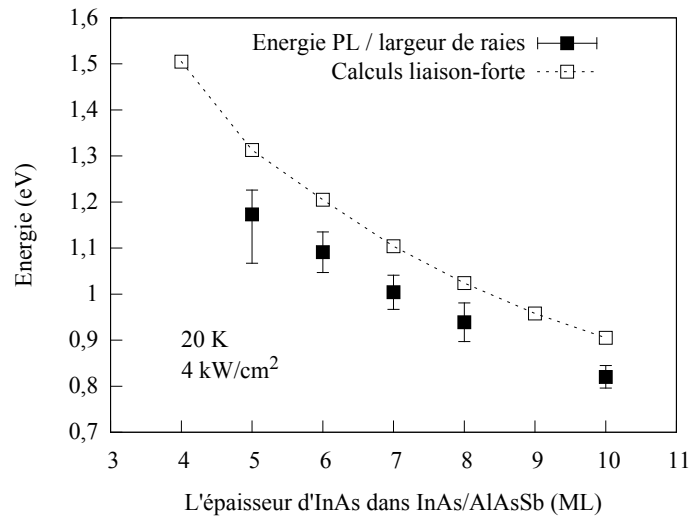


Fig. R.5 : Les puits quantiques InAs/AlAs_{0,56}Sb_{0,44} caractérisés par PL à basse température, où les énergies PL sont comparées avec leurs valeurs théoriques. Les marges d'erreur signifient la largeur de raie du pic PL.

Sb_{0,44}, et des multi-puits InAs/AlAs_{0,56}Sb_{0,44} sans contrainte macroscopique ont été réalisés. Pourtant, les études microscopiques ont démontré que la distribution de contrainte n'est pas parfaitement homogène à l'échelle microscopique. (section 3.4, page 64)

Finalement, de telles structures ont été fabriquées pour étudier la transition inter-sous-bande. Des résultats préliminaires n'ont pu démontrer des signes de l'absorption inter-sous-bande ; cependant il est relevé que les transitions inter-bandes entre le niveau fondamental de bande de conduction et celui de trous légers apparaît dans le spectre d'anisotropie d'absorption, et cela peut masquer l'observation d'absorption inter-sous bande puisque les deux mécanismes d'absorption ne soit pas bien séparées spectralement.

Les rôles de l'effet surfactant de Sb sur la croissance de boîtes quantiques InAs/GaAs_{0,51}Sb_{0,49}

L'effet de l'antimoine en surface sur la croissance de structures InAs/GaAs_{0,51}Sb_{0,49} a été également étudié sur substrats InP selon des différentes orientations de surface. En présence d'antimoine, le dépôt d'InAs sur substrats InP d'orientation (001) conduit à la formation de couche entière d'InAs et par conséquent des puits quantiques de type-II ont été obtenus (image TEM dans figure R.6a). (sous-section 4.2, page 81)

Sur substrats InP (113)B, le même dépôt d'InAs mène à la formation d'îlots quantiques de haute densité. En comparant des îlots observés par microscope à force atomique et ceux vus par STM, il est mis en évidence que des îlots couverts par GaAs_{0,51}Sb_{0,49} ont des dimensions similaires que leurs équivalents en surface ; cela confirme un résultat précédant que la présence de Sb peut préserver la forme des îlots contre la dissolution

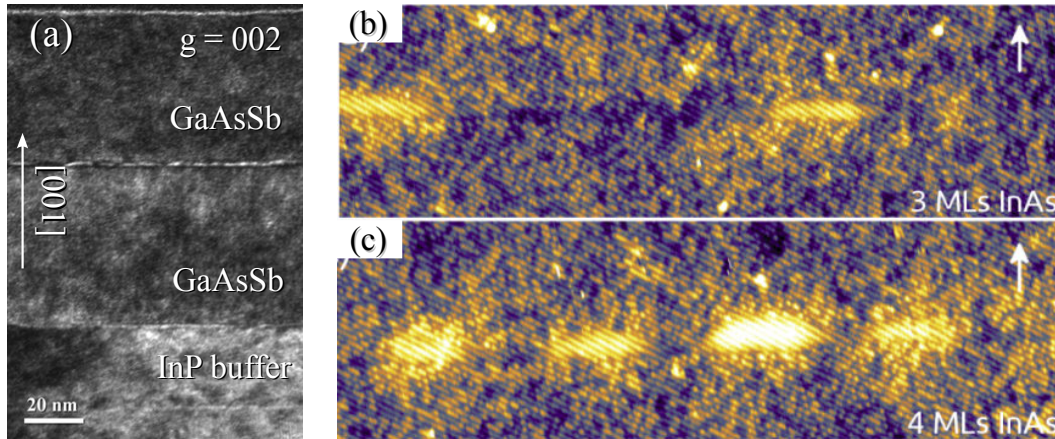


Fig. R.6 : Des nanostructures InAs/GaAs_{0,51}Sb_{0,49}/InP vus par le tranche. (a) Image TEM d'une telle structure faite sur substrat InP (001); (b) (c) images STM de celles élaborée sur surface (113)B de InP

dans la couche d'encapsulation [11] (figure R.7b et R.7c).

Les caractérisations par photoluminescence montrent une forte dépendance des spectres à la puissance d'excitation qui est caractéristique à hétérostructure de type-II. Cependant, le signal PL provenant de couche de mouillage n'a pas été observé, alors qu'elle est couramment observée dans les îlots quantiques formés sous le mode de croissance Stranski-Krastanow. L'absence de couche de mouillage dans ce système est ensuite confirmée par l'observation STM et il est conclu que ces îlots se sont formés sous le mode de croissance Volmer-Webber. (sous-section 4.2, page 84)

Pour comprendre les comportements différents des dépôts d'InAs sur les différentes surfaces de substrat, l'influence de l'antimoine est discutée en termes énergétiques. La modification de l'anisotropie de l'énergie de surface induite par l'antimoine permet d'interpréter nos résultats sur substrats (100) et (113)B. Sb réduit énergie de surface d'InAs de bas-indices (par exemple {001}) mais il augmente celle de surface d'InAs de haut-indices comme {113} et {114}. Pour le dépôt d'InAs sur surface (001) de GaAs_{0,51}Sb_{0,49}, la formation de couche de mouillage orienté (001) est favorisée alors que la formation des îlots composés de facettes de haut-indices orienté {114} est défavorisée; par conséquent, le dépôt d'InAs sur substrat InP reste plat en présence de Sb. Pour le même dépôt sur un substrat InP (113)B, la compétition est inversée: l'utilisation d'antimoine favorise la formation des facettes de bas-indices comme des îlots tandis que la formation d'une couche entière d'InAs orienté (113) est défavorisée; éventuellement des îlots de forte densité sont obtenus. (section 4.3, page 91)

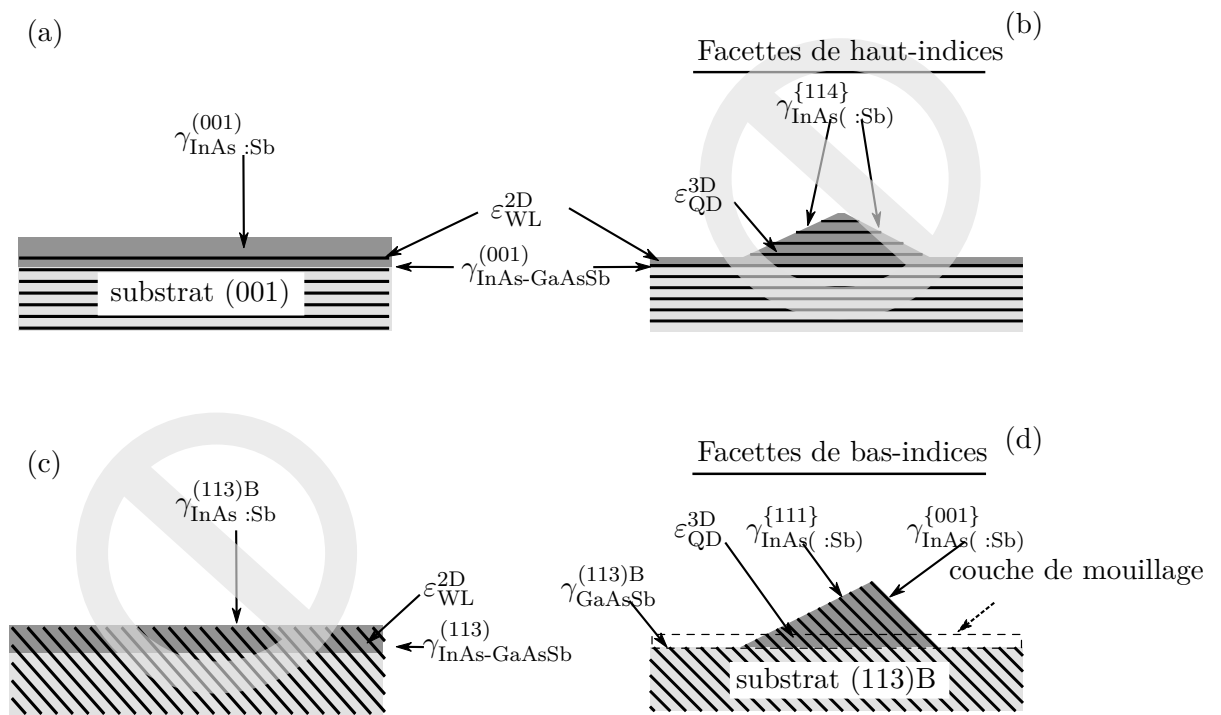


Fig. R.7 : Des possibilités éventuelles de dépôts d'InAs sur les surfaces de GaAs_{0.51}Sb_{0.49}. (a) couche de mouillage formée sur surface (001); (b) un îlot formé sous mode croissance Stranski-Krastanow sur substrat (001); (c) couche de mouillage sur substrat (113)B; (d) Un îlot InAs formé sous mode Volmer-Webber sur surface (113)B de GaAs_{0.51}Sb_{0.49}.

L'incorporation de Sb dans une couche d'InAs sous contrainte sur substrat InP

Ayant une bande-interdite encore plus petite qu'InAs, l'utilisation d'alliage $\text{InAs}_{1-x}\text{Sb}_x$ pourrait aussi étendre des applications de filière InP dans moyen-infrarouge. Pourtant, le niveau d'incorporation de Sb dans une couche InAs pourrait être très limité du à l'introduction d'une contrainte plus importante.

L'incorporation de Sb dans l'alliage $\text{InAs}_{1-x}\text{Sb}_x$ est d'abord estimée par des calculs thermodynamiques. La figure R.8 présente les compositions d' $\text{InAs}_{1-x}\text{Sb}_x$ calculées pour les conditions de croissance couramment utilisées, y compris le rapport de flux entre des éléments de groupe V/III ainsi que le rapport entre les flux d'arsenic et antimoine. Quand la contrainte de cohérence n'est pas incluse dans les calculs, le niveau d'incorporation d'antimoine pourrait être important ; cette situation correspond au dépôt d'InAs(Sb) massif où des couches sont relaxées. Par contre, quand la contrainte est prise en compte, l'incorporation d'antimoine est devenue difficile telle que l'incorporation d'antimoine devient très faible. (section 5.1, page 98 ; section A.2, page 120)

Finalement, l'incorporation d'antimoine dans $\text{InAs}_{1-x}\text{Sb}_x$ a été également examinée avec les puits quantique $\text{InAs}_{1-x}\text{Sb}_x/\text{Al}_{0,48}\text{In}_{0,52}\text{As}$. Au contraire des calculs, les différentes combinaisons de flux pendant le dépôt d'InAs(Sb) ont des influences importantes sur l'énergie de transition dans ces structures. Pour l'instant, ces influences sont attribuées à la formation des nanostructures 3D d' $\text{InAs}_{1-x}\text{Sb}_x$, mise en évidence par l'observation AFM de surface. Cependant, cette conclusion nécessite des études plus approfondies à l'échelle microscopique. (section 5.2, page 101)

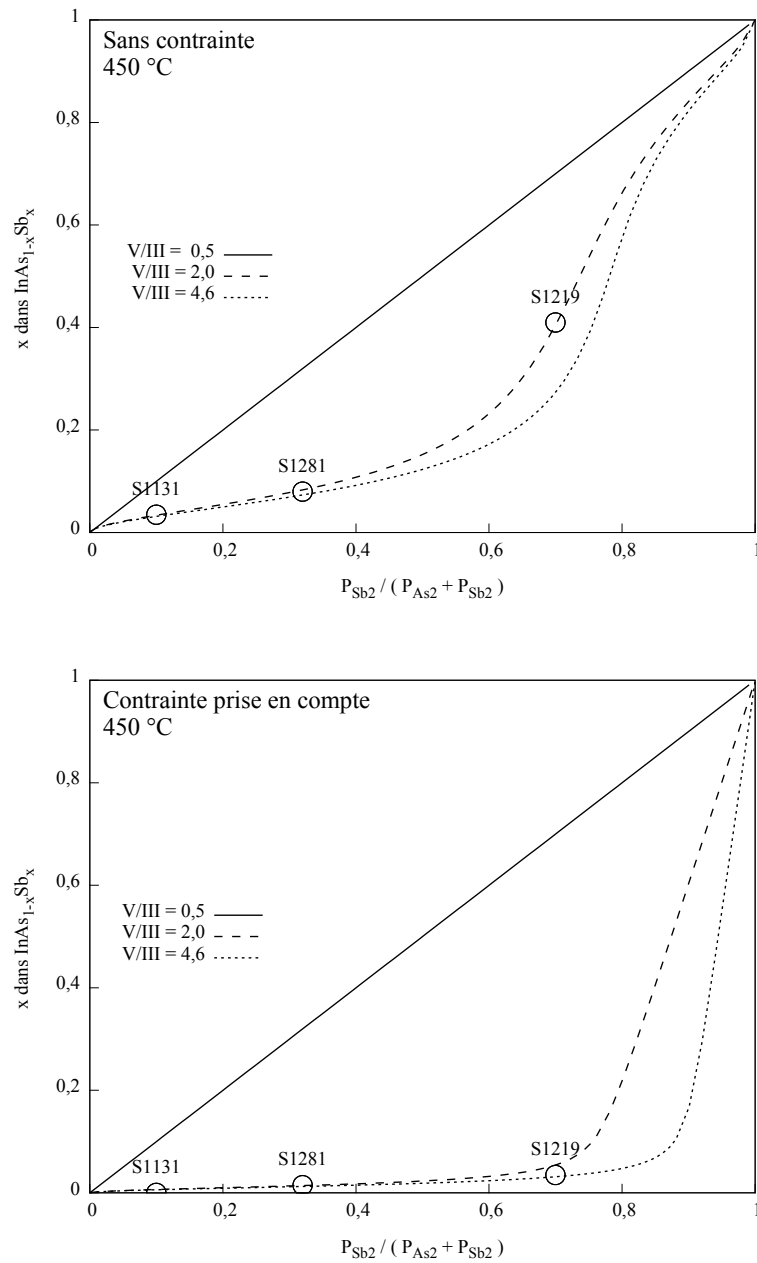


Fig. R.8 : Calculs thermodynamiques sur l'incorporation de Sb d'alliage InAsSb. (a) composition de l'alliage relaxé ; (b) composition de l'alliage sous contrainte en accord de maille avec substrat InP.

Appendices

A.1 Inter-subband absorption workbench

Figure A.1 schematically illustrates the key components in the inter-subband absorption workbench. A compact halogen lamp was employed as light source and a compact spectrometer was used for detection. Since the spectrometer is grating based, second order diffractions has to be filtered by long-pass filters. The fiber based optics makes the experiment setup very portable. This workbench was initially developed by Marianne Prévôt (FOTON).

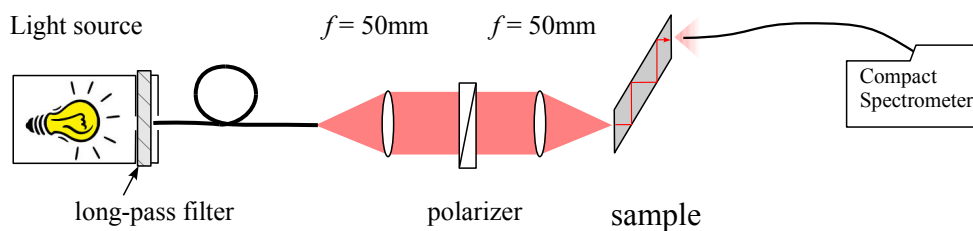


Figure A.1: Current workbench

The photo in figure A.2 gives an example of multi-reflection waveguide used in inter-subband absorption study.

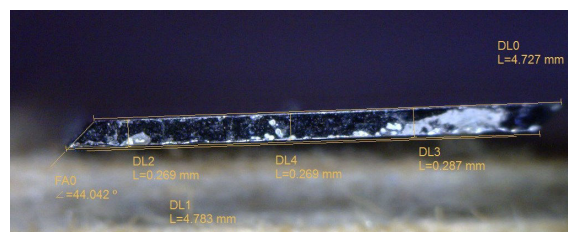


Figure A.2: Multi-reflection waveguide sample S1346.

A concern that may intervene the inter-subband absorption measurements would be chromatic aberrations of the optics. To counteract, we have chosen achromatic lens doublets. To verify that such aberration does not disturb the inter-subband absorption measurement, we have compared a GaN/AlGaIn reference sample using the current

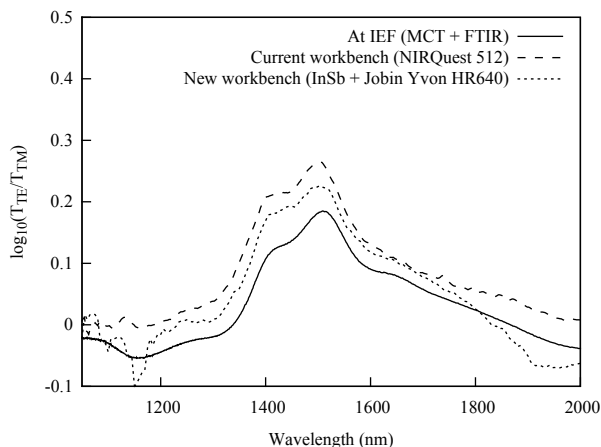


Figure A.3: Tests of inter-subband absorption workbench, comparing results obtained with FTIR (IEF Orsay), current workbench using compact spectrometer, and the new workbench under development using grating spectrometer with InSb detector.

workbench and another workbench at IEF which is well tested. Figure A.3 shows a comparison of the absorption anisotropy spectra. The current workbench was able to reproduce every detail of the absorption anisotropy spectra in the 1100-2100 nm range, which is the range of wavelength that inter-subband absorption of $\text{Ga}_{0.47}\text{In}_{0.53}\text{As}/\text{Al-As}_{0.56}\text{Sb}_{0.44}$ would appear.

A.2 Thermodynamic calculations on the composition of $\text{InAs}_{1-x}\text{Sb}_x$

Thermodynamics

The MBE growth of ternary alloys like $\text{InAs}_{1-x}\text{Sb}_x$ is thermodynamically equivalent to the sequence of processes described in figure A.4.

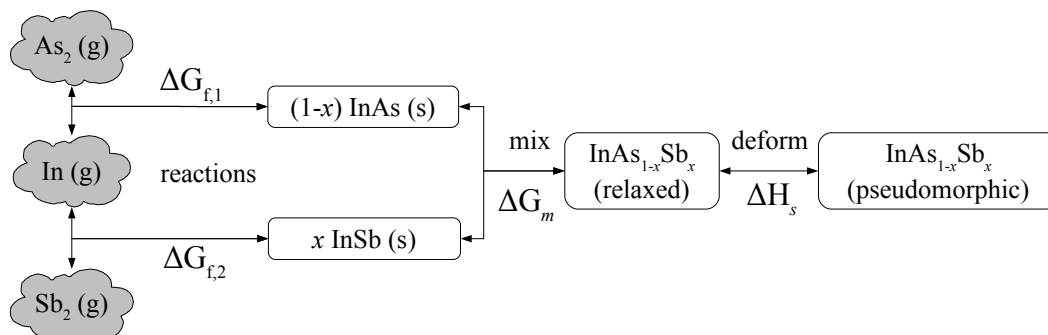


Figure A.4: Thermodynamics descriptions of the growth of pseudomorphic $\text{InAs}_{1-x}\text{Sb}_x$ layer on InP substrate.

When the materials in gas phase and solid are in equilibrium, their chemical potentials satisfy the following equalities :

$$\mu_{\text{In(g)}} + \frac{1}{2}\mu_{\text{As2(g)}} = \mu_{\text{InAs(s)}} \quad (\text{A.3})$$

$$\mu_{\text{In(g)}} + \frac{1}{2}\mu_{\text{Sb2(g)}} = \mu_{\text{InSb(s)}} \quad (\text{A.4})$$

For molecules in gas phases like In, its chemical potential is determined by its standard formation free energy $\mu_{\text{In,f}}^{\ominus}$ and its pressure over the growth surface (P_{In}). For In this is termed as :

$$\mu_{\text{In}}(T) = \mu_{\text{In,f}}^{\ominus}(T) + RT \ln(P_{\text{In}}/P^{\ominus}) \quad (\text{A.5})$$

in which $P^{\ominus} = 101325$ Pa.

The total free energy of $\text{InAs}_{1-x}\text{Sb}_x$ ΔG_{total} formed by N_1 amount of InAs N_2 amount of InSb is expressed as the sum of their standard formation free energies, mixing free energies and coherency strain energy :

$$\begin{aligned} \Delta G_{\text{total}} = & N_1 G_{\text{InAs,f}}^{\ominus} + N_2 G_{\text{InSb,f}}^{\ominus} && \dots && \text{standard formation energies} \\ & + (N_1 + N_2)\Delta G_{\text{m}}(x) && \dots && \text{mixing free energy} \\ & + (N_1 + N_2)\Delta H_{\text{s}}(x) && \dots && \text{strain energy} \end{aligned}$$

in which $x = N_2/(N_1 + N_2)$. The Chemical potential of InAs (InSb) in $\text{InAs}_{1-x}\text{Sb}_x$ alloy is thus by definition the modification of total free energy by introducing unity amount of InAs (InSb):

$$\mu_{\text{InAs}}(x) = \frac{\partial \Delta G_{\text{total}}}{\partial N_1} = G_{\text{f,InAs}}^{\ominus} + \frac{\partial(N_1 + N_2)\Delta G_{\text{m}}(x)}{\partial N_1} + \frac{\partial(N_1 + N_2)\Delta H_{\text{s}}(x)}{\partial N_1} \quad (\text{A.6})$$

$$\mu_{\text{InSb}}(x) = \frac{\partial \Delta G_{\text{total}}}{\partial N_2} = G_{\text{f,InSb}}^{\ominus} + \frac{\partial(N_1 + N_2)\Delta G_{\text{m}}(x)}{\partial N_2} + \frac{\partial(N_1 + N_2)\Delta H_{\text{s}}(x)}{\partial N_2} \quad (\text{A.7})$$

The standard Gibbs free energy of each material is the sum of its standard formation enthalpy and entropy $G^{\ominus} = H_{\text{f}}^{\ominus} - T \cdot S_{\text{f}}^{\ominus}$, which are directly available in standard reference data. For reference, the thermodynamic data used in the calculations of Sb-incorporation in InAsSb layer are listed in table A.2 and A.3.

Regular solution model describes the mixing related energy reduction as [1, pp. 123-128]:

$$\Delta G_{\text{m}}(x) = x(1-x)\Omega + RT [x \ln x + (1-x) \ln(1-x)] \quad (\text{A.8})$$

in which Ω the ‘‘interaction parameter’’ is a quantity that describes the solubility and miscibility of alloy components. Ω value is taken as 2250 kcal/mol for InAsSb, which is

recommended in [1, p. 28]. Thus ‘mixing’ part of chemical potential becomes :

$$\frac{\partial(N_1 + N_2)\Delta G_m(x)}{\partial N_1} = x^2\Omega + R T \ln(1 - x) \quad (\text{A.9})$$

$$\frac{\partial(N_1 + N_2)\Delta G_m(x)}{\partial N_2} = (1 - x)^2\Omega + R T \ln x \quad (\text{A.10})$$

The strain energy associated with epitaxial layer under tetra-orthogonally deformation is [2]:

$$\Delta H_s(x) = \left[C_{11}(x) + C_{12}(x) - 2\frac{C_{12}^2(x)}{C_{11}(x)} \right] \frac{N_A a_0^3}{4} \left[\frac{a(x) - a_0}{a(x)} \right]^2 \quad (\text{A.11})$$

in which N_A is Avogadro’s constant, a_0 is the lattice constant of substrate, $a(x)$ is the lattice constant of relaxed $\text{InAs}_{1-x}\text{Sb}_x$. C_{nn} s are elastic constants of $\text{InAs}_{1-x}\text{Sb}_x$, obtained by linear interpolation the properties of InAs and InSb.

$$\frac{\partial(N_1 + N_2)\Delta H_s(x)}{\partial N_1} = H(x) - x \cdot H'(x) \quad (\text{A.12})$$

$$\frac{\partial(N_1 + N_2)\Delta H_s(x)}{\partial N_2} = H(x) + (1 - x) \cdot H'(x) \quad (\text{A.13})$$

Since almost every term in the expression of $H(x)$ is a function of $x = N_1/(N_1 + N_2)$, the expression for its derivations of N_1 (N_2) becomes rather complicated ; thanks to symbolic math toolboxes, such error prone process can be performed automatically, thus the detailed expression is not listed here. Eventually, the chemical potentials of InAs and InSb in $\text{InAs}_{1-x}\text{Sb}_x$ become:

$$\mu_{\text{InAs}}(x) = \Delta G_{\text{f,InAs}}^{\ominus} + RT \ln(1 - x) + x^2\Omega + H_s(x) - x \cdot H'_s(x) \quad (\text{A.14})$$

$$\mu_{\text{InSb}}(x) = \Delta G_{\text{f,InSb}}^{\ominus} + RT \ln x + x^2\Omega + H_s(x) + (1 - x) \cdot H'_s(x) \quad (\text{A.15})$$

By substituting all quantities into equations , equations (A.3) and (A.4) turn into :

$$P_{\text{In}}P_{\text{As}_2}^{1/2} = \exp(\Delta\mu_1/RT) \quad (\text{A.16})$$

$$P_{\text{In}}P_{\text{Sb}_2}^{1/2} = \exp(\Delta\mu_2/RT) \quad (\text{A.17})$$

in which

$$\begin{aligned} \Delta\mu_1 &= \mu_{\text{InAs(s)}} - \mu_{\text{In(g)}} - \frac{1}{2}\mu_{\text{As}_2(\text{g})} \\ \Delta\mu_2 &= \mu_{\text{InSb(s)}} - \mu_{\text{In(g)}} - \frac{1}{2}\mu_{\text{Sb}_2(\text{g})} \end{aligned}$$

This is equation is ready to be solved under growth condition the following constraints

respectively established by the definition of x and the conservation of material:

$$x = \frac{P_{\text{Sb2}}^0 - P_{\text{Sb2}}}{P_{\text{As2}}^0 - P_{\text{As2}} + P_{\text{Sb2}}^0 - P_{\text{Sb2}}} \quad (\text{A.18})$$

$$P_{\text{In}}^0 - P_{\text{In}} = 2 \left(P_{\text{As2}}^0 - P_{\text{As2}} + P_{\text{Sb2}}^0 - P_{\text{Sb2}} \right) \quad (\text{A.19})$$

$H'(x)$ is a rather complicated expression due to every quantity depends on x . Fortunately, such chores can be dealt with symbolic math tools.

Solution to equation

By dividing equation (A.16) by (A.17) and take the square root of the two side of equation, we have

$$w^{1/2} = P_{\text{As2}}/P_{\text{Sb2}} \quad (\text{A.20})$$

in which:

$$w = \exp [(\Delta\mu_1 - \Delta\mu_2) / RT] \quad (\text{A.21})$$

Equations (A.18) and (A.20) can be written in the form of linear simultaneous equations:

$$\begin{bmatrix} 1 & -w^{1/2} \\ 1 & 1 - x \end{bmatrix} \begin{bmatrix} P_{\text{As2}} \\ P_{\text{Sb2}} \end{bmatrix} = \begin{bmatrix} 0 \\ P_{\text{As2}}^0 + (1 - x)P_{\text{Sb2}}^0 \end{bmatrix} \quad (\text{A.22})$$

By solving the above matrix equation about P_{As2} and P_{Sb2} , these two quantities can be expressed using functions of x . The same is applied to P_{In} :

$$P_{\text{In}} = P_{\text{In}}^0 - 2[P_{\text{As2}} - P_{\text{As2}}] - 2[(P_{\text{Sb2}} - P_{\text{Sb2}})] \quad (\text{A.23})$$

By now, all the unknowns can be expressed in x , and the thermodynamic problem can thus be solved by minimizing the sum of objective function

$$F(x) = \Delta\mu_1^2(x) + \Delta\mu_2^2(x)$$

The definition domain of x is sometimes non-continuous subsets of interval $[0,1]$ so that general solvers are not able to solve such a problem with singularities. We have designed special solver codes for finding the solution x .

Table A.2: Lattice constants and elastic constants of materials used in this study. Data taken from [3].

	a_0 (300 K) Å	C_{11} (300 K) 10 GPa	C_{12} (300 K) 10 GPa	C_{44} (300 K) 10 GPa
GaAs (s)	5.653	11.90	5.34	5.96
GaSb (s)	6.096	8.83	4.02	4.32
InAs (s)	6.058	8.34	4.54	3.95
InSb (s)	6.479	6.67	3.65	3.92
InP (S)	5.869	10.11	5.61	4.56

Table A.3: Standard formation enthalpy and entropy. Elemental indium and gallium data taken from “standard thermodynamic properties of chemical substances” (http://www.update.uu.se/~jolkkonen/pdf/CRC_TD.pdf).

Material	H_f^\ominus (289 K) kJ/mol	S_f^\ominus (289 K) J/(K·mol)	a	b	c
Ga (g)	272	169	3/2 R	–	–
In (g)	243	173	3/2 R	–	–
As ₂ (g)	190.79	240.881	37.196	0.151	-0.201
As ₄ (g)	153.301	327.431	82.939	0.130	-0.515
Sb ₂ (g)	231.207	254.914	36.405	0	-0.1
Sb ₄ (g)	206.522	350.109	83.094	0.013	-0.209
GaAs (s)	-74.056	64.183	45.187	6.067	0
GaSb (s)	-43.932	76.056	44.35	14.226	0
InAs (s)	-58.576	75.730	47.07	7.531	0
InSb (s)	-30.543	87.111	44.769	15.062	0

The thermodynamic properties at given temperature is calculated by the following formulae :

$$H_f(T) = H_f^\ominus(298) + a \cdot (T - 298) + b \cdot 10^{-3}(T^2 - 298^2)/2 - 10^6 c \cdot (T^{-1} - 298^{-1})$$

$$S_f(T) = H_f^\ominus(298) + a \cdot [\log(T) - \log(298)] + b \cdot 10^{-3}(T - 298) - c \cdot 10^6(T^{-2} - 298^{-2})/2$$

A.3 Surfactant effect on the surface of $\text{Ga}_{0.47}\text{In}_{0.53}\text{As}$

In order to clarify the influence of Sb on InAs surface while avoiding discussing the role of strain, we have examined the surface of lattice-matched $\text{Ga}_{0.47}\text{In}_{0.53}\text{As}$ annealed under either Sb_2 -based surface termination or under As_2 one.

Totally four samples were prepared in two growth-runs, accounting for two surface termination methods and two substrate orientations. As usual, the growth rate of $\text{Ga}_{0.47}\text{In}_{0.53}\text{As}$ was 0.23 ML/s, the V/III beam equivalent pressure ratio was about 6:1 and the substrate temperature was set to 450 °C during all growth-runs. In the first growth-run, two samples S1277.1 and S1277.2 were grown simultaneously on InP (001) and (113)B substrates. To ensure the flatness of growth front, a thick InP buffer layer was deposited before the deposition of $\text{Ga}_{0.47}\text{In}_{0.53}\text{As}$ layer. Being aware that segregated indium atoms may cumulate on its final surface, the thickness of this $\text{Ga}_{0.47}\text{In}_{0.53}\text{As}$ layer was chosen as small as 10 nm. Following that, the surface of $\text{Ga}_{0.47}\text{In}_{0.53}\text{As}$ is exposed to As_2 flux for as long as 600 s to ensure that InAs deposition has reached its equilibrium shape. And finally, the substrate temperature is ramped down at fastest rate possible under As_2 flux. In the second growth-run, two samples S1283.1 and S1283.2 were grown under the same procedures except that the $\text{Ga}_{0.47}\text{In}_{0.53}\text{As}$ surfaces were annealed under combined (As_2+Sb_2) flux. The beam equivalent pressure ratio between As_2 and Sb_2 flux was about 1:5.

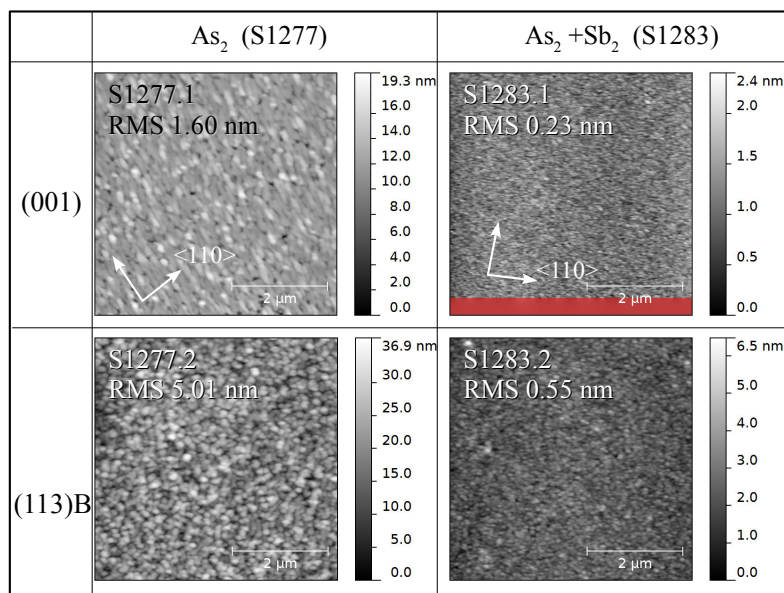


Figure A.5: Surface of $\text{Ga}_{0.47}\text{In}_{0.53}\text{As}$ annealed under As_2 flux or (As_2+Sb_2) combined.

Figure A.5 reports contact-mode AFM observations of annealed $\text{Ga}_{0.47}\text{In}_{0.53}\text{As}$ surfaces, and figure A.6 shows several line profiles taken from these AFM images. The most striking feature among these images is the nanostructures formed on sample S1277.1/2

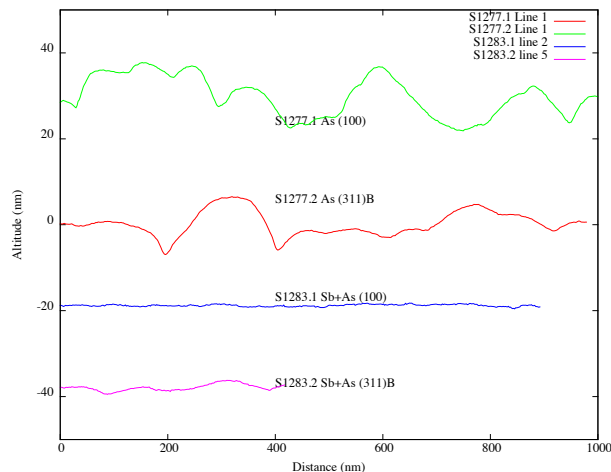


Figure A.6: Line profiles taken in AFM images in figure A.5.

(As₂ annealing). Further AFM profiles analyses also indicate that the inclination of their facets can be as large as 25°, which correspond to well-defined facets rather than vicinal surfaces. This is in clear contrast with the surfaces obtained under (As₂+Sb₂) annealing, which remain relative flat. We consider the surface has reached its equilibrium shape after 600 s annealing, and the discrepancy between surface obtained under two surface termination method has thus becomes a direct evidence that Sb can change the equilibrium shape of lattice-matched Ga_{0.47}In_{0.53}As deposition.

It's worth noting that the GaInAs islands formed on (001) surface are elongated along one of its [1 1 0] directions while those island formed on (113) surface is more isotropic. The shape of elongated islands agrees with the anisotropic surface diffusion on GaInAs (001) surface [4]. Such strongly anisotropic surface morphology cannot be achieved without extensive mass transport, which in turn confirms that the surface is under equilibrium.

For (As₂+Sb₂)-annealed Ga_{0.47}In_{0.53}As surface (S1283.1/2), no 'real' quantum-dot like object is detected on either of the two samples. Although the difference between two substrate orientations is less pronounced, the 'granular texture' is more obvious on (113)B surface than on (001) surface. In one hand, such result indicates that high-level of strain/mismatch is crucial for the formation of InAs island in the case of InAs/GaAs_{0.51}Sb_{0.49} (113)B quantum dots. On the other hand, the low surface energy of GaAs_{0.51}Sb_{0.49} (113)B surface could be another driving force for the formation of InAs/GaAs_{0.51}Sb_{0.49} Volmer-Weber quantum dots.

A.4 Routine experimental methods

Photoluminescence experimental setup

For most of the PL spectra presented in this thesis, a 532 nm YAG:Nd double frequency laser was used as excitation source. With the optics, it can achieve maximum power density of 4 kW/cm². Two additional 405 nm and 1064 nm laser were also used for complementary studies like PL peak identification. In this setup, a Helium closed-cycle cryostat was employed that enables PL studies from about 10 K to room temperature. A compact grating spectrometer was used for light detection. Its detector is a CCD array made of strained-GaInAs, and the working spectra range is from 890 nm to 2100 nm.

X-ray diffraction

All the X-ray diffraction and reflectivity studies presented in this thesis were performed on a Bruker D8-Discover goniometer. This machine is equipped with LynxEyeTM multi-channel 1D detector so that reciprocal space map measurement is as simple as $\omega-2\theta$ scans. We would like to thank to Valerie Demange from Université de Rennes 1 for granting us the use of this equipment.

Contact-mode atomic force microscope

All the AFM studies in this thesis were performed on a Veeco diInnova system. The AFM tip (nanoworld Arrow CONTR) has a typical tip radius of curvature of less than 10 nm. With such a tip, the inter-island space between high-density InAs/GaAsSb quantum dots presented in chapter 4 cannot be easily resolved.

References

- [1] G. B. Stringfellow, *Organometallic vapor-phase epitaxy, second edition: theory and practice*, 2nd ed. (Academic Press, Dec. 23, 1998), 572 pp.
- [2] F. Turco et al., “Thermodynamic analysis of the molecular beam epitaxy of AlInAs alloys”, *Journal of Crystal Growth* **88**, 282–290 (1988).
- [3] Ioffe Institute, *NSM archive physical properties of semiconductors*, (1998) <http://www.ioffe.rssi.ru/SVA/NSM/Semicond/> (visited on 06/10/2012).
- [4] J. Belk et al., “Surface alloying at InAs/GaAs interfaces grown on (001) surfaces by molecular beam epitaxy”, *Surface Science* **387**, 213–226 (1997).

AVIS DU JURY SUR LA REPRODUCTION DE LA THESE SOUTENUE

Titre de la thèse:

Growth and optical characterization of Sb-based materials on InP for optical telecommunication

Nom Prénom de l'auteur : ZHAO YU

Membres du jury :

- Monsieur ANDRE Régis
- Monsieur JULIEN François
- Monsieur BERTRU Nicolas
- Monsieur FOLLIOU Hervé
- Monsieur PERRIN Mathieu
- Monsieur KOENRAAD Paul
- Madame PONCHET Anne
- Monsieur TOURNIE Eric

Président du jury :

Date de la soutenance : 11 Février 2014

Reproduction de la these soutenue

- Thèse pouvant être reproduite en l'état
 Thèse pouvant être reproduite après corrections suggérées

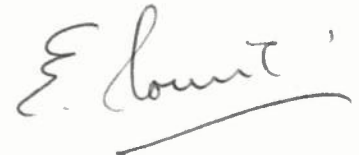
Fait à Rennes, le 11 Février 2014

Signature du président de jury

Le Directeur,



M'hamed DRISSI



Ce travail de thèse porte sur la croissance et sur la caractérisation optique de nanostructures à base d'antimoine sur substrats InP, en vue d'applications dans le domaine des télécommunications optiques.

La transition inter-sous-bande est un processus ultrarapide qui permet la modulation de la lumière dans les réseaux de télécommunication optique. Durant cette thèse, une absorption inter-sous-bande dans le proche-infrarouge provenant de puits quantiques $\text{Ga}_{0.47}\text{In}_{0.53}\text{As}/\text{AlAs}_{0.56}\text{Sb}_{0.44}$ a été observée pour la première fois au laboratoire. Les analyses par microscopie électronique à effet tunnel sur la face clivée montrent cependant de nombreuses déviations à l'idéalité de nos structures : mélange à l'échelle atomique aux interfaces entre GaInAs et AlAsSb, inhomogénéité de l'alliage GaInAs, incorporation non-intentionnel d'antimoine dans le GaInAs.

Les puits quantiques $\text{InAs}/\text{AlAs}_{0.56}\text{Sb}_{0.44}$ sont potentiellement des objets de choix pour la réalisation de composants inter-sous-bande travaillant à 1,55 μm . Des puits quantiques $\text{InAs}/\text{AlAs}_{0.56}\text{Sb}_{0.44}$ contraint, exempt de défauts ont été obtenus par croissance assistée par effet surfactant de Sb. En symétrisant la contrainte induite par le dépôt d'InAs par l'insertion de couches nanométriques de AlAs dans les barrières, des multi-puits $\text{InAs}/\text{AlAs}_{0.56}\text{Sb}_{0.44}$ sans contrainte macroscopique ont été réalisés.

L'effet de l'antimoine en surface sur la croissance de structure $\text{InAs}/\text{GaAs}_{0.51}\text{Sb}_{0.49}$ a également été étudié. En présence d'antimoine sur substrats InP d'orientation (001), le dépôt d'InAs conduit à la formation de puits quantiques. Par contre sur ceux orientés suivant (113)B des boîtes quantiques sont formées suivant le mode de croissance Volmer-Weber. Ces résultats sont discutés en termes d'effets cinétiques ou énergétiques de l'antimoine en surface. La modification de l'anisotropie de l'énergie de surface induite par l'antimoine permet d'interpréter nos résultats sur substrats (100) et (113) B.

Mots-clés : épitaxie par faisceaux moléculaires ; nanostructures ; optoélectronique ; composés semi-conducteurs

This PhD work presents molecular beam epitaxy growth and optical studies on several Sb-nanostructures on InP substrate, for their potential use in optical telecommunication.

Inter-subband transition in $\text{Ga}_{0.47}\text{In}_{0.53}\text{As}/\text{AlAs}_{0.56}\text{Sb}_{0.44}$ quantum well is a useful physical process for implementing ultrafast full-optical modulations. Near-infrared inter-subband transition in this material was achieved and microscopic studies on this structure has revealed that the intermixing at GaInAs/AlAsSb interface, unintentional Sb incorporation in GaInAs layer and the inhomogeneity within GaInAs layer could prevent $\text{Ga}_{0.47}\text{In}_{0.53}\text{As}/\text{AlAs}_{0.56}\text{Sb}_{0.44}$ multiple quantum wells from achieving inter-subband transition in 1.55 μm optical telecommunication band.

The strained $\text{InAs}/\text{AlAs}_{0.56}\text{Sb}_{0.44}$ quantum well is another material that has potential use in 1.55 μm full-optical modulation. 2 nm-thick defect-free $\text{InAs}/\text{AlAs}_{0.56}\text{Sb}_{0.44}$ was obtained under Sb surfactant-mediated growth, and by using strain compensation techniques, $\text{InAs}/\text{AlAs}_{0.56}\text{Sb}_{0.44}$ multiple quantum wells with zero net-strain were realized.

The study of Sb-mediated growth is also carried on to $\text{InAs}/\text{GaAs}_{0.51}\text{Sb}_{0.49}$ nanostructures. The growths of such structures on InP (001) substrate has led to the formation of flat InAs layer, while high-density $\text{InAs}/\text{GaAs}_{0.51}\text{Sb}_{0.49}$ quantum dots were obtained on InP (113)B substrates under Volmer-Weber growth mode. We attribute such phenomena to the surface-orientation dependent surfactant effect of Sb. Emission wavelength close to 2 μm was achieved with only 5 ML of InAs deposition, which makes these quantum dots attractive to InP-based mid-wave applications.

Keywords: molecular beam epitaxy, nanostructure, optoelectronics, compound semiconductors